The University of Sheffield

Growth and Characterisation of $GaAs_{1-x}Bi_x$

by

ABDUL RAHMAN BIN MOHMAD

A thesis submitted for the degree of Doctor of Philosophy

Department of Electronic and Electrical Engineering

July 2013

Table of Contents

1. Introduction

2. MBE Growth and Characterisation Techniques

3. Photoluminescence Investigation of GaAsBi Alloys

4. Effects of Rapid Thermal Annealing on GaAsBi Alloys

5. Effects of Growth Parameters on GaAsBi Alloys

6. Conclusion

In the name of God, the Most Gracious, the Most Merciful

Acknowledgement

I would like to express my gratitude to my supervisors, Dr. Jo Shien Ng and Professor John David for giving me opportunities, support and guidance throughout my PhD years. I would like to thank my current and former colleagues in the Impact Ionisation group, Xin Xin, Xiao, Pin Jern, Rajiv, Syahrin, Siew Li, Ben, Matthew, James, Jennifer, Jing Jing, Shiyu, Akeel, Simon, Danuta, Dr. Ian Sandall, Dr. Fadzlin Hasbullah and Dr. Lionel Tan for their assistance and friendship.

Many thanks to my MBE growth gurus, Dr. Faebian Bastiman, Dr. Shiyong Zhang and Richard Frith for their valuable training and advice. I also would like to acknowledge D. F. Reyes for the TEM images and Dr. D. E. Sykes for the SIMS profiles used in this thesis. Also to the dedicated bismide team (Chris and Rob) and my coffee buddies.

I am very grateful to have many wonderful friends (Yusuf, Fikri, Abg Roesli, Abg Luqman, Najib, Ahmed, Afifi and friends in IKRAM) who always motivate and inspire me to be a good person and to contribute to society.

I am indebted to my parents, Mr. Mohmad and Mrs. Jamilah and to my siblings, Azlan and Azwan for always being there for me. Special thanks to my beloved wife, Nurul Huda for the continuous love and support during our life together. To my little daughter, Nurul Iman, thank you for cheering up my days.

Abstract

This thesis reports the optical and structural properties of $GaAs_{1-x}Bi_x$ alloys grown on GaAs by Molecular Beam Epitaxy (MBE). The photoluminescence (PL) of a $GaAs_{0.97}Bi_{0.03}$ alloy was measured over a wide range of temperatures and excitation powers. The temperature dependence of the PL peak energy indicated significant exciton localization at low temperatures and the band gap varies more weakly with temperature than in GaAs. An analysis of dominant carrier recombination mechanism(s) was also carried out indicating that radiative recombination is dominant at low temperature.

The PL results indicate that dilute fractions of bismuth (Bi) with $x < 0.025$ improve the material quality of these low temperature growth alloys by reducing the density of gallium (Ga) and/or arsenic related defects. The crystal quality starts to degrade at higher Bi concentration probably due to a significant amount of Bi-related defects, i.e Bi_{Ga}. However, the room temperature PL intensity continues to increase with Bi content for x up to 0.06 due to the greater band-gap offset between GaAs and $GaAs_{1-x}Bi_x$.

To improve the quality of $GaAs_{1-x}Bi_x$ alloys, annealing and growth studies were carried out. At room temperature, the annealed $GaAs_{1-x}Bi_x$ showed a modest improvement (~ 3 times) in PL while the PL peak wavelength remained relatively unchanged. Also, the optimum annealing temperature is Bi composition dependent; for samples with $x < 0.048$, the optimum annealing temperature is 700 ^{o}C but it reduces to 600 ^{o}C for higher compositions.

Two growth parameters were investigated which are growth rate and As_4/Bi beam equivalent pressure (BEP) ratio. It was found that growth rate significantly affects Bi incorporation and the accumulation of surface Bi. Decreasing the As_4/Bi BEP ratio has been shown to increase Bi concentration but is limited by the formation of Bi double PL peaks.

List of publications

Journal papers

1. **A. R. Mohmad**, F. Bastiman, J. S. Ng, S. J. Sweeney and J. P. R. David, “Photoluminescence investigation of high quality GaAsBi on GaAs”, Appl. Phys. Lett. **98** 122107 (2011)

2. **A. R. Mohmad**, F. Bastiman, C. J. Hunter, J. S. Ng, S. J. Sweeney and J. P. R. David, “The effect of Bi composition to the optical quality of GaAsBi”, Appl. Phys. Lett. **99** 042107 (2011)

3. **A. R. Mohmad**, F. Bastiman, J. S. Ng, S. J. Sweeney and J. P. R. David, “Room temperature photoluminescence enhancement in GaAsBi alloys”, Phys. Stat. Solidi. C **9** 259 (2012)

4. **A. R. Mohmad**, F. Bastiman, C. J. Hunter, R. D. Richards, S. J. Sweeney, J. S. Ng and J. P. R. David, “Effects of rapid thermal annealing on GaAsBi alloys”, Appl. Phys. Lett **101** 012106 (2012)

5. F. Bastiman, **A. R. Mohmad**, J. S. Ng, S. J. Sweeney and J. P. R. David, “Non - stoichiometric GaAsBi / GaAs (100) molecular beam epitaxy growth”, J. Cryst. Growth **338** 57 (2012)

6. C. J. Hunter, F. Bastiman, **A. R. Mohmad**, R. Richards, J. S. Ng, S. J. Sweeney and J. P. R. David, “Absorption characteristics of GaAsBi/GaAs diodes in the near infra-red”, IEEE Photon. Technol. Lett. **24** 2191 (2012)

7. **A. R. Mohmad**, F. Bastiman, D. F. Reyes, C. J. Hunter, R. D. Richards, J. S. Ng and J. P. R. David, “Effects of growth rate on GaAsBi alloys grown by molecular beam epitaxy”, *in preparation for Optics Express*

Conference and poster presentations

1. **A. R. Mohmad**, F. Bastiman, J. S. Ng, S. Jin, S. J. Sweeney and J. P. R. David, "Photoluminescence investigation of bulk GaAsBi on GaAs", 1st International Workshop on Bismuth Containing Semiconductors, Michigan, USA, 14 - 16 July 2010

2. F. Bastiman, **A. R. Mohmad**, J. S. Ng, S. Sweeney and J. P. R. David, "Growth and characterisation of $GaAs_{1-x}Bi_x$ for Opto-electronic applications", 25th Semiconductor and Integrated Opto-Electronics Conference (SIOE), Cardiff, UK, 18 - 20 April 2011.

3. Z. Batool, **A. R. Mohmad**, T. J. C. Hosea, N. Hossain, K. Hild, T. Tiedje and S. J. Sweeney, "Band gap – spin-orbit splitting cross-over observed in GaBiAs/GaAs layers with high bismuth concentration", 25th Semiconductor and Integrated Opto-Electronics Conference (SIOE), Cardiff, UK, 18 - 20 April 2011.

4. **A. R. Mohmad**, F. Bastiman, J. S. Ng, S. J. Sweeney and J. P. R. David, "Composition dependent photoluminescence of $GaAs_{1-x}Bi_x$ alloys on GaAs", 38th International Symposium on Compound Semiconductors (ISCS), Berlin, Germany, 22 - 26 May 2011.

5. Z. Batool, K. Hild, T. J. C. Hosea**, A. R. Mohmad**, T. Tiedje, R. Butkute, V. Pacebutas, A. Krotkus and S. J. Sweeney, "Optical characterisation of GaBiAs/GaAs samples for 1.5 µm application", UK Semiconductor 2011, Sheffield, UK, 6 - 7 July 2011. (Won best poster)

6. **A. R. Mohmad**, F. Bastiman, C. J. Hunter, J. S. Ng, S. J. Sweeney and J. P. R. David, "The effect of Bi composition to the optical quality of $GaAs_{1-x}Bi_x$ alloys", 2nd International Workshop on Bismuth Containing Semiconductors, Surrey, UK, 18 - 20 July 2011.

7. Z. Batool, K. Hild, T. J. C. Hosea**, A. R. Mohmad**, X. Lu, T. Tiedje, R. Butkute, V. Pacebutas, A. Krotkus and S. J. Sweeney, “Resonance of band gap and spin orbit splitting in GaAsBi/GaAs alloys”, 2nd International Workshop on Bismuth Containing Semiconductors, Surrey, UK, 18 - 20 July 2011

8. **A. R. Mohmad**, F. Bastiman, C. J. Hunter, R. D. Richards, S. J. Sweeney, J. S. Ng and J. P. R. David, “Effects of rapid thermal annealing on the optical and structural properties of $GaAs_{1-x}Bi_x$”, Semiconductor and Integrated Opto-Electronics Conference (SIOE) 2012, Cardiff, UK, 2 - 4 April 2012.

9. C. J. Hunter, F. Bastiman **A. R. Mohmad**, R. D. Richards, J. S. Ng, S. J. Sweeney and J. P. R. David, “Absorption characteristics of GaAsBi/GaAs diodes in the near infra-red”, Semiconductor and Integrated Opto-Electronics Conference (SIOE) 2012, Cardiff, UK, 2 - 4 April 2012.

10. F. Bastiman, C. J. Hunter, **A. R. Mohmad**, R. D. Richards, J. S. Ng, S. J. Sweeney and J. P. R. David, “Growth and characterisation of $GaAs_{1-x}Bi_x$ p-i-n diodes”, E-MRS Spring meeting, Strasbourg, France, 14 - 18 May 2012.

11. R. D. Richards, F. Bastiman**,** C. J. Hunter, **A. R. Mohmad**, J. S. Ng and J. P. R. David, “Effect of arsenic species on growth of $GaAs_{1-x}Bi_x$”, UK Semiconductor 2012, Sheffield, UK, 4 - 5 July 2012

12. C. J. Hunter, F. Bastiman **A. R. Mohmad**, R. D. Richards, J. S. Ng, S. J. Sweeney and J. P. R. David, “Optical and electrical properties of $GaAs_{1-x}Bi_x$/GaAs diodes”, 3rd International Workshop on Bismuth Containing Semiconductors, Victoria, Canada, 15 - 18 July 2012

13. **A. R. Mohmad**, F. Bastiman, C. J. Hunter, R. D. Richards, S. J. Sweeney, J. S. Ng and J. P. R. David, “The effect of growth parameters on the optical and structural quality of $GaAs_{1-x}Bi_x$ alloys”, 17th International Conference on Molecular Beam Epitaxy, Nara, Japan, 23 – 28 September 2012

14. F. Bastiman, **A. R. Mohmad**, C. J. Hunter, R. D. Richards, D. F. Mendes, D. F. Reyes, D. L. Sales, J. S. Ng and J. P. R. David, "Reconstruction orientated Bi incorporation mechanisms in GaAsBi/GaAs (100)", submitted to 17th European Molecular Beam Epitaxy Workshop, Levi, Finland, 10 – 13 March 2013.

Glossary of Terms

α, β	Varshni fitting parameters
σ	localisation constant
Θ_B	Bragg's angle
Δ_{SO}	spin-orbit splitting energy
AFM	atomic force microscopy
BEP	beam equivalent pressure
C_{Bi}	coupling between bismuth level and GaAs VBM
E_a	activation energy
E_{Bi}	energy level for bismuth
E_c	energy of the conduction band minima
E_g	energy of band gap
E_{maxloc}	maximum localisation energy
E_o	band gap at 0 K
E_v	energy of VBM
ΔE_{VBAC}	band gap reduction due to Bi incorporation predicted by VBAC model
FEL	fast entry lock
FWHM	full-width-at-half-maximum
$\hbar$	Planck's constant
HR-XRD	high resolution X-ray diffraction

I_o	integrated PL intensity at 10 K
IPL	integrated PL intensity
J_{th}	threshold current density
k	Boltzmann’s constant
LAN	local area network
m	gradient
$m*$	hole effective mass
MAN	metro area network
MBE	molecular beam epitaxy
MOVPE	metal-organic vapour phase epitaxy
P_e	excitation power density
PL	photoluminescence
QD	quantum dot
QW	quantum well
RHEED	reflection high-energy electron diffraction
RTA	rapid thermal annealing
SIMS	secondary ion mass spectrometry
STM	scanning tunnelling microscopy
TEM	transmission electron microscopy
UHV	ultra high vacuum
VBAC	valence band anti-crossing
VBM	valence band maximum

Chapter 1

Introduction

1.1 Motivation

Over the past decade, internet traffic has increased tremendously as a result of an increasing number of people being connected and the growing amount of information on the internet. The internet also has evolved from text based to picture to video and recently, high definition videos. Therefore, higher bandwidth and an increase in data transmission speed are required in order to meet the increasing demand.

The internet traffic data is sent over long distances through high speed optical fibre telecommunication networks. These networks use laser diodes to transmit data in light pulses which pass through fibre cables. The information is then sent to home users through series of lower bandwidth and shorter distance networks called metro and local area networks (MANs and LANs). Since optical fibre networks are expensive, most of the LANs or the ‘last mile’ connections do not use optical fibres, relying on copper cables instead. This creates a bottleneck as the bandwidth and data transmission speed to the home users are limited. Therefore, the realization of high speed, reliable and low cost optoelectronic devices is important in order to expand the optical fibre coverage to home users.

The optical fibre networks require laser diodes to operate at specific wavelengths. This is because the properties of optical fibres are wavelength dependent. The two important properties of optical fibres that need to be considered are dispersion and attenuation. Dispersion occurs because the speed of light is a function of wavelength. The laser pulse (which has some degree of spectral linewidth) will start to disperse as it travels in a dispersive material (the optical fibre) leading to pulses that are broader in time. Thus, adjacent pulses begin to overlap after some distance, making it difficult to decode the original transmitted data. Dispersion thus limits the bandwidth as significant pulse overlapping must be avoided.

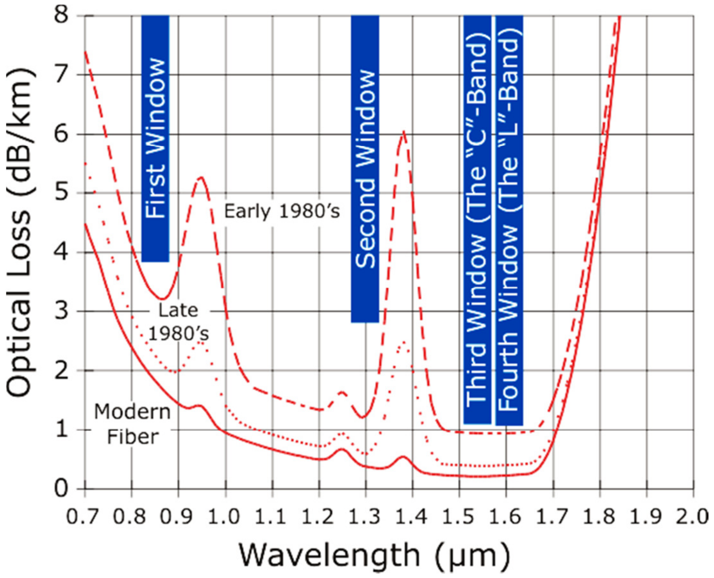

Figure 1.1 The wavelength dependent signal attenuation in optical fibre. The dashed, dotted and solid lines represent the level of attenuation in fibre developed at different times [1].

Figure 1.1 shows the attenuation in optical fibre as a function of wavelength. The advances of fibre technology lead to lower levels of attenuation, thus allowing the signal to travel a longer distance before being attenuated to an unacceptably low magnitude. Optical fibres have three main operating windows which are at wavelengths of 0.85, 1.31 and 1.55 μm. Each of these operating windows has its own advantages. In modern fibres, the first operating window, 0.85 μm, has a relatively high optical loss of 1.8 dB/km. However, cheap GaAs lasers and Si detectors operate at this window. The 1.31 μm window is attractive due to zero dispersion in the fibres and it has a lower optical loss of 0.5 dB/km. The third operating window, 1.55 μm, has the lowest optical loss of 0.2 dB/km, making it the preferred choice for long haul optical fibre networks. Based on these reasons, it is important to have a light emitter and detector which operate at wavelengths of 1.31 and 1.55 μm.

1.2 A rainbow of choices

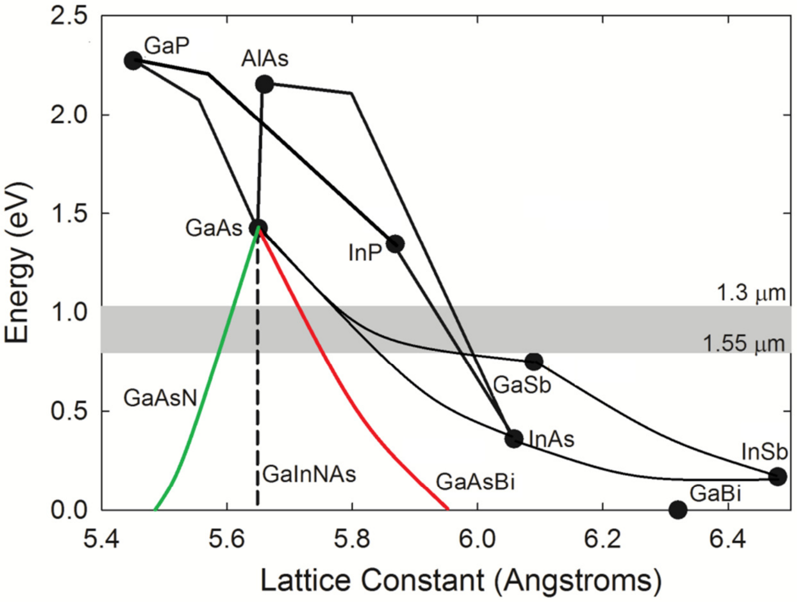

Figure 1.2 Band gap versus lattice constant for various III-V alloys.

A semiconductor material with light emission between 1.31 and 1.55 µm wavelength requires a band gap between 0.95 to 0.8 eV. The choices of materials operating in this region are shown in Figure 1.2. The semiconductor material must also be closely lattice matched to readily available substrates which are GaAs and InP. For decades, InGaAsP laser diodes grown on InP substrates have been used for the long haul optical fibre backbone.

InGaAsP based lasers operating at 1.3 and 1.55 µm wavelengths have a superior threshold current density, J_{th} of ~ 90 to 100 A/cm^2 [2]. However, the threshold current density, J_{th} exhibits an exponential increase with temperature (~exp(T/T_o) where T_o is the characteristic temperature) [3]. This loss has been attributed to; (i) carrier confinement leakage, (ii) Auger recombination loss, (iii) intervalence band absorption and (iv) non-radiative recombination at defects and interface states [3]. The use of strained InGaAs-InGaAsP QW (instead of unstrained QW or bulk devices) has been shown to improve J_{th} by reducing the magnitude of intervalence band absorption loss [4]. However, InGaAsP based lasers operating at 1.55 µm still suffer from carrier confinement leakage and significant Auger recombination loss which account for 80 – 90% of J_{th} at room temperature [5, 6].

However, InP based devices are too expensive to be implemented for the high volume of MANs and LANs. InP substrates are significantly more expensive and normally come in a smaller size compared to GaAs substrates. This is because it is difficult to manufacture large diameter InP wafers reliably. The use of small substrates will increase the production costs. A 6-inch InP substrate (only available from Sumitomo) costs ~ £1800 while the same size GaAs substrate only costs ~ £350. Therefore, an attractive approach to reduce cost is by changing from InP substrates to GaAs substrates.

Various GaAs based semiconductor alloys have been studied with a view to developing emitters for the second and third operating windows. For $In_xGa_{1-x}As/GaAsP$ quantum wells, the emission wavelength is limited to < 1.24 µm with maximum indium content of 0.4 [7]. Extending the emission wavelength by using a higher indium content will result in the formation of dislocations, thus degrading the device performance. This is because the compressive strain introduced by the incorporation of indium in GaAs becomes extremely high even after strain compensation by the quantum well barriers. Therefore, 1.3 and 1.55 µm emission cannot be achieved by $In_xGa_{1-x}As$ on GaAs. Nonetheless, high performance InGaAs lasers have been reported with J_{th} as low as 45 and 90 A/cm^2 for 0.98 and 1.23 µm wavelengths, respectively [7, 8].

1.2.1 Dilute nitride

One of the most widely studied material systems for GaAs-based 1.3 µm emitters for the past 17 years is dilute nitrides. Dilute nitrides extend the emission wavelength of GaAs-based devices to 1.3 µm (and beyond) which cannot be achieved by InGaAs quantum wells. The GaInNAs alloy was first proposed by Kondow *et al* in 1996 [9]. The incorporation of nitrogen (N) in GaAs reduces the band gap as well as introducing tensile strain. Therefore, a lattice matching with GaAs can be achieved by strain compensation between nitrogen and indium. GaInNAs alloy will be lattice matched to GaAs provided that the In:N ratio is ~ 3:1 [10].

The incorporation of N in GaAs introduces a large band gap reduction which is 125 meV/% N [11]. The band gap reduction is mainly attributed to the decrease of the conduction band minima as a result of a band anti-crossing interaction between the conduction band edge of GaAs and the N resonant level [12]. The large conduction band reduction also provides a better electron confinement in GaInNAs/GaAs quantum wells compared to InGaAsP quantum wells, resulting in an improved temperature dependence for dilute nitride lasers. For 1.3 μm emission, the conduction band offset between a $Ga_{0.7}In_{0.3}N_{0.01}As_{0.99}$ well and a GaAs barrier is 350 meV, deep enough to prevent electron overflow at room temperature [13]. However, the conduction band offset between a $In_{0.3}Ga_{0.7}As_{0.6}P_{0.4}$ well and a $In_{0.1}Ga_{0.9}As_{0.2}P_{0.8}$ barrier is only 100 meV for a similar emission wavelength [13].

However, the growth of the GaInNAs alloy is more complicated compared to other conventional alloys (i.e InGaAs, AlGaAs). GaInNAs is a metastable alloy due to the large difference in covalent radius between N and arsenic (As). Therefore, this semiconductor alloy has to be grown at relatively low temperatures (typically ~ 430 ^{o}C) to incorporate even a small amount of nitrogen. If the growth temperature is increased beyond the miscibility gap of the GaInNAs alloy, phase separation will occur which results to the formation of microscopic regions of InGaAs and InGaN [14].

It is generally observed that the incorporation of N leads to a degradation of optical quality. The reasons put forward to explain this include high density of nitrogen interstitials, ion damage (due to high RF power) and low growth temperatures [15-17]. Thermal annealing has been shown to significantly improve the photoluminescence (PL) intensity (by a factor of ~10) but at the expense of a blue-shift in the emission wavelength after annealing [16, 18]. As wafer quality degrades with N content, most of the long wavelength GaInNAs devices are designed to have a maximal indium concentration and a minimal N content, leading to high strain. The compressive strain is typically mitigated by utilising GaNAs barriers (tensile strained) instead of GaAs barriers, which allows more quantum wells to be grown before strain relaxation occurs. For instance, up to three periods of 7 nm-GaInNAs/GaAs quantum wells with In > 0.3 can be grown without strain relaxation

[14]. However, by utilising GaNAs barriers, up to nine periods of 7 nm-GaInNAs quantum wells can be grown without structural deterioration [14].

A review by Harris on the progress of GaInNAs lasers shows that the threshold current density increases exponentially with wavelength and the trend can be fitted empirically with $J_{th} = 500exp\{8(\lambda - 1.2)\}$ A/cm^2 [14]. Thus a 1.55 µm GaInNAs laser will have a threshold current density of 8.2 kA/cm^2 (almost 100 times higher than InGaAsP lasers). This empirical fitting uses actual data from various reports with laser emission wavelengths from 1.2 to 1.45 µm. Later, it was found that the use of an antimony surfactant during GaInNAs growth greatly improves the wafer quality. Antimony (Sb) reduces the segregation of indium during growth and delays the transition of the growth mode from 2D to 3D [14, 19]. Depending on the type of Sb flux and growth conditions, 1 – 10% of Sb may be incorporated to form the quinary alloy, GaInNAsSb. Harris also reported that the mean surface roughness of a $Ga_{0.61}In_{0.39}N_{0.016}As_{0.964}Sb_{0.02}$ sample measured by AFM is half of that of a similar sample grown without an Sb surfactant [14]. The Sb-containing sample shows single atomic layer steps which indicate 2D and layer by layer growth [19]. However, compositional control becomes increasingly complicated as it involves three group V elements which are all interdependent. To date, a high performance 1.54 µm GaInNAsSb laser has been reported with J_{th} = 373 A/cm^2 [20]. Despite various improvements, the threshold current density is still ~ 4 times higher than InP based lasers.

1.2.2 InAs quantum dots

Another approach which was pursed by researchers is quantum dots (QDs). In a QD structure, the free electron motion is restricted in all directions (3D). According to a theoretical work carried out by Arakawa and Sakaki in 1982, QD lasers are expected to have an infinite T_o (i.e J_{th} independent of temperature) as thermal spreading can be suppressed due to a delta function-like density of states (DOS) [21]. Asada *et al* also predicted that lower threshold current densities and higher material gain should be obtained by QD lasers compared to quantum well and bulk devices [22]. InAs QDs have very low J_{th} which is between 26 – 40 A/cm^2 for lasers emitting at ~ 1.2 µm [23]. These values are lower than any quantum well based lasers. For 1.3 µm emission, J_{th} = 70 A/cm^2 has been demonstrated [24]. Despite the superior threshold current density, some of the theoretical predictions are yet to be achieved in practice, mainly due to growth issues.

The main challenge for growing QD lasers is to achieve a homogeneous and sufficiently high dot density while maintaining a low density of defects. The typical QD density, 3.0×10^{10} cm^{-2}, is insufficient to achieve high modal gain. This is because the dots do not occupy the whole area of the active layer. Recently, Fujitsu Laboratories reported a successful attempt to increase the dot density of QD lasers to 5.9×10^{10} cm^{-2} (almost twice the typical dot density) [25]. However, increasing the QD density beyond 10^{11} cm^{-2} could result in the formation of defect clusters and consequently deteriorate the device performance [26].

Another technique that was adopted to increase the overall QD density is introducing multiple stacks of QD layers, separated by spacer layers. Ideally, the spacer layers should be smooth in order to obtain similar QD characteristics in the following layers. However, this is difficult to achieve in practice especially for large numbers of QD stacks. Furthermore, the overall strain will also increase with an increasing number of QD stacks. This limits the number of QD layers as excessive strain will cause the formation of dislocations. To date, the highest net modal gain of QD lasers reported in the literature is 7 cm^{-1} per QD layer (typical values are between 4 – 5 cm^{-1} per QD layer) [25]. For comparison, a typical modal gain for a quantum well devices is above 15 cm^{-1} per QW layer [26].

The J_{th} of QD lasers is also dependent on temperature, contrary to the earlier theoretical work in Ref. [21]. For example, Bimberg *et al* showed that J_{th} is initially constant with temperature but increases exponentially above 100 K [27]. This is because at higher temperatures the injected carriers possess sufficient thermal energy to escape from QD confinement and start to populate the barrier states. Hence, higher injection current is required to maintain the threshold gain of the laser. Despite these problems, commercial InAs QD lasers became available in 2000. However, InAs QD lasers with emission wavelengths up to 1.55 µm remain elusive.

1.3 Dilute bismide materials

Recently, increasing interest has been shown towards another semiconductor alloy called dilute bismide. The introduction of bismuth (Bi) in GaAs introduces many interesting properties which make the alloy a promising material system for light emitters and detectors for optical fibre systems.

1.3.1 Brief history of GaAsBi and related alloys

Band gap engineering based on the introduction of Bi to III-V semiconductors started as early as 1971. The initial works targeted mid and long wavelength infrared photo-detectors. Joukoff *et al* proposed that the semi-metallic character of InBi could reduce the band gap of InSb when Bi sits on antimony sites [28]. Various methods have been used to grow InSbBi and related alloys (InAsBi, InAsSbBi) including Czochralski [28], metal-organic vapour phase epitaxy (MOVPE) [29] and molecular beam epitaxy (MBE) [30]. It was reported that the band gaps of InAsBi and InAsSbBi reduce at the rates of 55 meV/%Bi and 46 meV/%Bi, respectively [31]. However, there has been a lack of progress in this material system due to growth difficulties and the limited solubility of Bi [29, 30].

The incorporation of Bi into GaAs was first reported by Oe *et al* in 1998 [32]. The work was motivated by realisation of semiconductor lasers with improved temperature characteristics (compared to InP based devices) whose emission wavelengths remained nearly constant with ambient temperature variations. Oe *et al* proposed that the $GaAs_{1-x}Bi_x$ alloy, consisting of a semiconductor (GaAs) and a semi-metal (GaBi) will have a temperature insensitive band gap [32]. $GaAs_{1-x}Bi_x$ is also a metastable alloy, similar to the dilute nitrides. In this case, it is due to the large difference in covalent radii between As and Bi which are 0.118 nm and 0.145 nm, respectively. Oe's growth was carried out using MOVPE and a Bi content of 0.024 was achieved [32]. The temperature dependent PL showed that the PL peak energy of $GaAs_{0.976}Bi_{0.024}$ changes by only 0.1 meV/K compared to 0.56 meV/K for GaAs [32, 33]. The only drawback they reported was the presence of small clumps of whiskers on the sample surface whose density increased with growth time.

In 2001, researchers at the National Renewable Energy Laboratory (NREL), USA, reported a piece of theoretical work exploring the idea of isoelectronic co-doping in order to improve the properties of dilute nitrides [34]. The isoelectronic co-doping of GaAs with N and Bi (GaNAsBi) is expected to yield several advantages. Firstly, it allows lattice matching to GaAs substrates as the compressive strain induced by the large Bi atoms can be compensated by the tensile strain introduced by the small N atoms. Secondly, this material system offers a wider scope of band structure design as N mainly influences the conduction band whilst Bi influences the valence band. In addition, the composition of N and Bi could be adjusted to achieve a particular band gap with minimal N.

Finally, the electron mobility of the GaNAsBi alloy is expected to be higher compared to the dilute nitrides [34]. In dilute nitrides, the difference in electronegativity, size and pseudopotential between N and As results in the formation of trap states below the conduction band minima which degrade the electron mobility. For example, the electron mobility of GaN_xAs_{1-x} reduces by 5 times compared to GaAs for x up to 0.005 [35]. However, isoelectronic co-doping with N and Bi (in GaNAsBi) is expected to enhance electron mobility as the oppositely charged long range Coulomb scatterers (N and Bi) combine to form single short range dipole scatterers [34]. This strategy was motivated by the success of charged co-doping between Be and O in GaN in which the electron mobility increases by one to two orders of magnitude [36].

In the meantime, The University of British Columbia (UBC) had been actively involved in the growth of dilute nitrides using a Bi surfactant. They found that the use of a Bi surfactant reduced the surface roughness of GaNAs by an order of magnitude and enhanced the N incorporation [37]. Furthermore, the PL intensity increases by more than two times compared to the surfactant-free samples [37]. In 2003, they started the growth of $GaAs_{1-x}Bi_x$ alloys. During early developments, Bi concentration was often determined by Rutherford Backscattering Spectroscopy (RBS). This is because the lattice constant of cubic GaBi is unknown experimentally even though it has been predicted to be 6.324 Å [38]. Later, Tixier *et al* reported the lattice parameter of free standing GaBi as 6.33 ± 0.06 Å [11], consistent with the predicted value. This was done by linear extrapolation of their experimental values of the $GaAs_{1-x}Bi_x$ lattice constant (measured by high resolution X-ray diffraction (HR-XRD)) versus Bi concentration measured by RBS.

Yoshimoto *et al* were the first to report a systematic study investigating the growth conditions required to incorporate Bi into GaAs [39]. The first conclusion that was made is that the growth temperature must be reduced to less than 400 ^{o}C. Due to the metastable nature of the growth process, decreasing the growth temperature increases the miscibility of Bi into GaAs. Secondly, the As flux has to be reduced until the As:Ga flux ratio is close to the stoichiometric value. For As flux values which are much larger than the Ga flux, Bi atoms cannot be incorporated as they are out-competed by As atoms for lattice sites. However, if the As flux was reduced lower than the stoichiometric value, the surface of the grown epilayer started to become rough.

Finally, Yoshimoto *et al* also found that increasing the Bi flux initially increased Bi incorporation, followed by saturation at high flux [39]. The saturation region was attributed to low miscibility of Bi into GaAs. Ref. [40] also reported similar observations and proposed that growth inside the saturation region should be avoided as it may result in the formation of Bi droplets. The results reported by Yoshimoto *et al* suggest that the $GaAs_{1-x}Bi_x$ alloy has a narrow growth window and efforts to increase Bi concentration without significantly degrading the wafer quality will be challenging [39]. Besides, MBE may be a better choice for $GaAs_{1-x}Bi_x$ growth compared to MOVPE due to the low growth temperature requirement. The growth temperature which is less than 400 ^{o}C is not ideal for MOVPE as it will lead to a high contamination of carbon due to insufficient decomposition of the precursors [39].

To date, the highest Bi concentration in GaAs reported in the literature is 0.22 [41]. This was achieved by lowering the growth temperature as low as 200 ^{o}C [41]. Ref. [41] reports HR-XRD data used to verify the Bi concentration but did not show any optical quality data. The HR-XRD spectra show a broad and diffuse $GaAs_{1-x}Bi_x$ peak with no fringes which indicates rough and incoherent interfaces. Even though no optical data was reported, it is expected that the optical quality will be severely degraded due to a high defect density. For GaAs grown at 200 °C, the density of arsenic anti-sites, As_{Ga} is typically ~ 10^{20} cm^{-3} [42]. If other types of defects are also taken into consideration (e.g. Ga related defects, Bi related defects, dislocations), the quality of $GaAs_{1-x}Bi_x$ layers grown at such low temperatures is expected to be poor and may not be suitable for practical devices. The longest room temperature PL wavelength reported in the literature is 1.44 µm with $x = 0.11$[43]. This indicates that a Bi concentration of ~ 0.11 may be the limit for reasonable optical quality and practical devices. If a further band gap reduction is required, N alloying may be considered to form GaNAsBi.

Recently, electroluminescence (EL) from $GaAs_{1-x}Bi_x$ light emitting diodes has been reported [44-46]. Ref. [44] reported room temperature EL with an injection current of 50 Acm^{-2} for a sample with $x = 0.018$. However, Ref. [46] reported a much lower injection current of 8 Acm^{-2} for $x = 0.06$. This significantly lower injection current was probably due to a higher growth temperature being used for the $GaAs_{1-x}Bi_x$ layer (400 °C compared to 300 °C for the former) and also the positive effect of introducing a growth interrupt. For every 50 nm of bismide layer, the growth was interrupted and a thin GaAs layer was grown without the presence of a Bi flux in order to reduce the accumulation of excess Bi [46]. Furthermore, lasing oscillation from 390 nm thick $GaAs_{0.975}Bi_{0.025}$ by photo-pumping was also reported [47]. In this work, a room temperature lasing wavelength of 983 nm was observed with threshold pumping density of 2.5 mJ/cm^2. The high pumping density was attributed to the lack of carrier confinement in the active layer.

The absorption properties of $GaAs_{1-x}Bi_x$ *p-i-n* diodes also have been reported with a view to developing solar cells and photodetectors [48]. In these applications, a thick (compared to quantum well thickness) absorber layer and low unintentional doping concentration are required to ensure efficient absorption of light (and hence high efficiency and responsivity) and full depletion at zero or low voltage [49]. According to Hunter *et al,* the responsivity of 0.35 µm thick $GaAs_{0.94}Bi_{0.06}$ at 1200 nm is 0.09 A/W, which corresponds to an absorption coefficient of 4×10^3 cm^{-1}[48]. This absorption coefficient is comparable to $Ga_{0.92}In_{0.08}N_{0.03}As_{0.97}$ (5×10^3 cm^{-1}) but is lower than $In_{0.53}Ga_{0.47}As$ (~2 × 10^4 cm^{-1}), measured at a similar wavelength [49, 50]. A lower absorption coefficient was obtained for $GaAs_{0.94}Bi_{0.06}$ (compared to $In_{0.53}Ga_{0.47}As$) because it was measured close to the band gap ($E - E_g = 33$ meV) where absorption begins to roll-off. If the absorption coefficient of $In_{0.53}Ga_{0.47}As$ is also measured at $E - E_g = 33$ meV, a value which is comparable to $GaAs_{0.94}Bi_{0.06}$ (~5 × 10^3 cm^{-1}) will be obtained [50]. The responsivity should be improved by increasing the layer thickness. However, this is only possible with strain compensation by alloying N into $GaAs_{1-x}Bi_x$. The unintentional doping concentration in $GaAs_{1-x}Bi_x$ was reported to be sufficiently low and vary between ~1 × 10^{14} to ~1 × 10^{16} cm^{-3}[51, 52]. This should enable photodetectors and solar cells to operate at zero or low reverse voltage.

State-of-the-art multi-junction solar cells consist of InGaP/GaAs/Ge [53]. It was proposed that the introduction of an additional junction with a band gap of 1 eV on top of the Ge junction will increase the efficiency of the solar cells to > 40 % [53]. GaNAsBi lattice matched to GaAs (or Ge) with a band gap of 1 eV can be achieved with Bi and N concentrations of 0.022 and 0.013, respectively [54]. The concentrations of both Bi and N are relatively low and can be easily achieved in practice. Therefore, the GaNAsBi alloy has the potential to be applied in quadruple-junction solar cells.

1.3.2 Benefits of bismuth for optoelectronic devices

Bismuth containing semiconductors have attracted increasing interest in recent years due to the large band gap reduction possible with small concentrations of Bi, thus promising for long wavelength devices [11, 55, 56]. Introducing Bi into GaAs reduces the semiconductor band gap by 88 meV/%Bi, which is much larger than the 16 and 21 meV/% of In and Sb, respectively, and only lower than the 125 meV/%N alloying [11]. It was suggested that incorporation of Bi increases the valence band maximum due to an anti-crossing interaction between the GaAs valence band and the Bi resonant level (further explanation in Section 1.3.3) [57, 58]. This is analogous to the conduction band anti-crossing interaction in dilute nitrides between the conduction band edge and the nitrogen resonant states.

In order to reduce the cost of optical-fibre networks, laser diodes with temperature insensitive wavelength emission are desirable. Despite the importance of the InGaAsP material system for laser diodes, its emission wavelength and threshold current density are very sensitive to temperature. This is due to the small conduction band offset between the quantum wells and the barriers. As the device temperature increases during operation, carriers become more mobile and tend to escape from the wells. Hence, the device efficiency and output power will be reduced. To compensate for this, a higher injection current is needed, leading to a further increase in temperature. In order to avoid thermal run-away and maintain a stable operation, InGaAsP lasers need to be equipped with external thermoelectric coolers which increase cost and power consumption. It was reported that the temperature coefficient of the $GaAs_{1-x}Bi_x$ band gap (obtained by temperature dependent PL) is as small as 0.1 meV/K compared to ~ 0.4 meV/K for InGaAsP [59-61]. Such temperature insensitivity is useful in the active regions of laser diodes and could potentially eliminate the need for cooling packages for lasers.

Furthermore, Bi containing alloys offer the possibility to suppress Auger recombination loss in near- to mid-infrared laser diodes [54]. Auger recombination is a non-radiative process in which an electron and a hole recombine in a band-to-band transition but the energy released is used to excite another carrier into the conduction or valence band. As a result, three carriers become unavailable for lasing and hence, increase the threshold current density. The threshold current density is then given by $J_{th} \approx Cn_{th}^3$, where C is the Auger recombination coefficient and n_{th} is the threshold carrier density [62]. There are four types of Auger processes called CHCC, CHSH, CHLH and CHHH which correspond to the excitation of a third carrier within the conduction band (CB), spin-split off (S-O) to heavy hole band (HH), light hole (LH) to HH band and within HH, respectively. However, the most dominant processes are CHSH and CHCC as shown in Figure 1.3 (a) and (b). It was reported that the CHLH Auger current is ~ 100 times weaker compared to CHSH and CHCC while CHHH transition is very weak due to heavy mass and often neglected [63]. In addition, phonon-assisted Auger recombination may also occur for each type of processes. Figure 1.3 (c) shows an example of a phonon-assisted CHSH process. In this process, the excited carrier passes through to an intermediate state I before reaching the final state by the emission or absorption of a phonon.

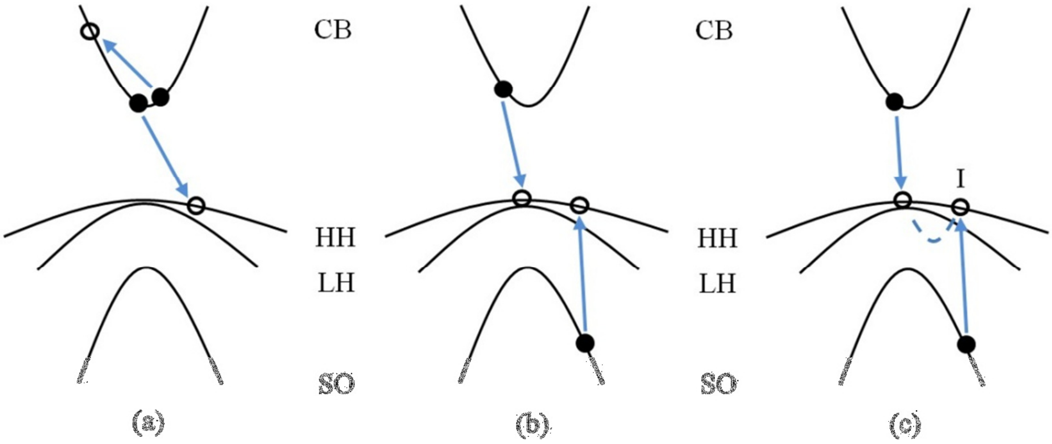

Figure 1.3 Schematic diagram showing (a) CHCC (b) CHSH and (c) phonon-assisted CHSH Auger recombination processes.

At room temperature, Auger loss accounts for 50 % and 80 % of the threshold current density for 1.3 and 1.55 µm InGaAsP lasers, respectively [6]. However, for mid-infrared lasers operating at 2 and 3 µm wavelengths, i.e GaInAsSb/GaSb, the threshold current density is significantly lower. This effect is illustrated in Figure 1.4. It was proposed that this is due to the spin-orbit splitting energy (Δ_{SO}) being larger than the band gap, which inhibits Auger recombination and inter-valence band absorption transitions involving the S-O band since energy and momentum can no longer be conserved [54, 64]. This is expected to improve laser performance and has been reported in InGaAsSbP/InAs mid-infrared LEDs [65]. However, the CHCC and CHLH processes may still occur.

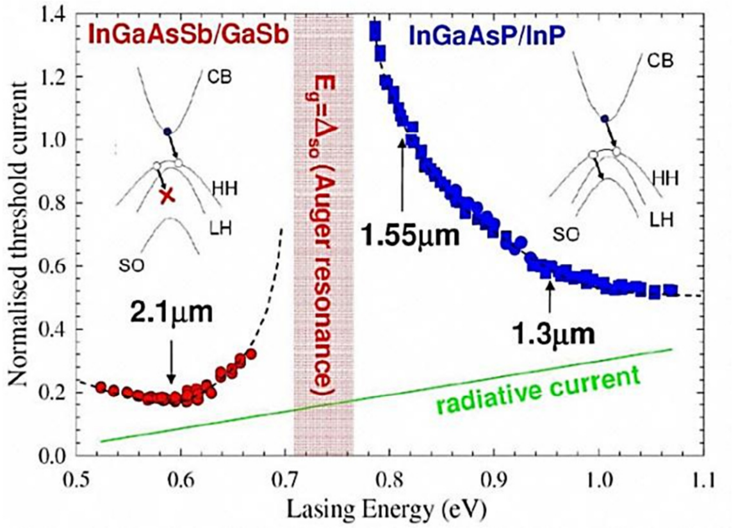

Figure 1.4 Normalised threshold current versus lasing energy for near and mid infrared lasers [64].

Being the largest element in group V, Bi is attractive because Δ_{SO} increases super linearly with the atomic number of the group V element [64]. It was theoretically predicted that GaBi has an extremely large Δ_{SO} which is ~ 2.2 eV compared to 0.8 eV and 0.35 eV for GaSb and GaAs, respectively [58]. It was calculated that Δ_{SO} will be larger than the band gap of $GaAs_{1-x}Bi_x$ when x ~ 0.10 to 0.11 [54, 66]. By incorporating N into $GaAs_{1-x}Bi_x$, strain compensation can be achieved and a further band gap reduction will be obtained. Figure 1.5 shows the predicted variation of band gap and Δ_{SO} for GaAsBiN with varying Bi and N concentrations. The condition for $E_g < \Delta_{SO}$ to supress Auger recombination loss may be achieved in GaAsBiN laser diodes operating in the near- to mid-infrared (>1.55 μm) regions. A good understanding of the growth and properties of the ternary GaAsBi alloy is essential in order to realize high performance GaAsBiN devices.

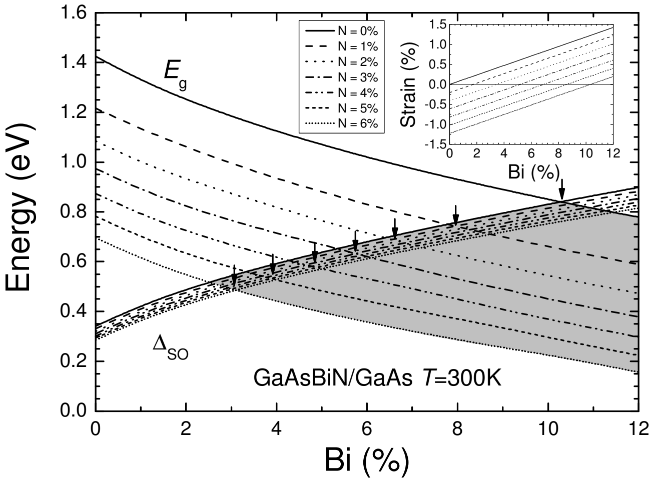

Figure 1.5 The variation of band gap and Δ_{SO} for the GaAsBiN alloy as predicted by Ref. [54]. The grey region represents the area for which $\Delta_{SO} > E_g$. The inset shows the variation of strain with varying Bi and N concentrations.

1.3.3 The Valence Band Anti-Crossing model

The band anti-crossing model was first proposed by Shan *et al* to explain the large band gap reduction in the dilute nitride system [12]. Dilute nitrides contain two anion species that are highly mismatched in atomic radius, which are N and As. Alberi *et al* proposed that the same principles can be adopted to explain the large band gap reduction in $GaAs_{1-x}Bi_x$, as the atomic radii of As and Bi are highly mismatched too [57]. This extended model is called the valence band anti-crossing (VBAC) model.

The incorporation of Bi into GaAs introduces Bi defect states which interact with the extended states of the host (GaAs). Since Bi has a lower electronegativity than As, the defect level is located close to the valence band edge of GaAs. The interaction between these states results in a splitting of the valence band into two sub-bands, called E_+ and E_- bands. The former is located at a higher energy than the Bi level while the latter is located at a lower energy. Based on the VBAC model, the energies of the E_+ and E_- levels are given by

$$E_{\pm}(\mathrm{GaAsBi}) = \frac{E_v(GaAs) + E_{Bi} \pm \sqrt{(E_v(GaAs) - E_{Bi})^2 + 4xC_{Bi}^2}}{2}, \qquad (1.1)$$

where $E_v(GaAs)$ is the energy of the valence band maximum (VBM) of GaAs, E_{Bi} is the energy of the Bi level, x is the Bi composition and C_{Bi} is the coupling between the Bi level and the GaAs VBM. The values of E_+, E_- and E_{Bi} are referenced to the VBM of GaAs, which is in turn referenced to zero. The value of C_{Bi} is 1.6 eV while the value of E_{Bi} is 0.4 eV below the VBM of GaAs [57]. Assuming a parabolic band for GaAs,

$$E_v\,(GaAs) = -\,\frac{\hbar^2 k^2}{2m^*}\,, \tag{1.2}$$

where $\hbar$ is the Planck constant, k is the momentum and m^* is the hole's effective mass. Figure 1.6 shows the calculated dispersion relations of the valence band of $GaAs_{0.98}Bi_{0.02}$. The anti-crossing interaction between the VBM of GaAs and Bi level causes the valence band maximum of $GaAs_{1-x}Bi_x$ to increase, consequently reducing the band gap.

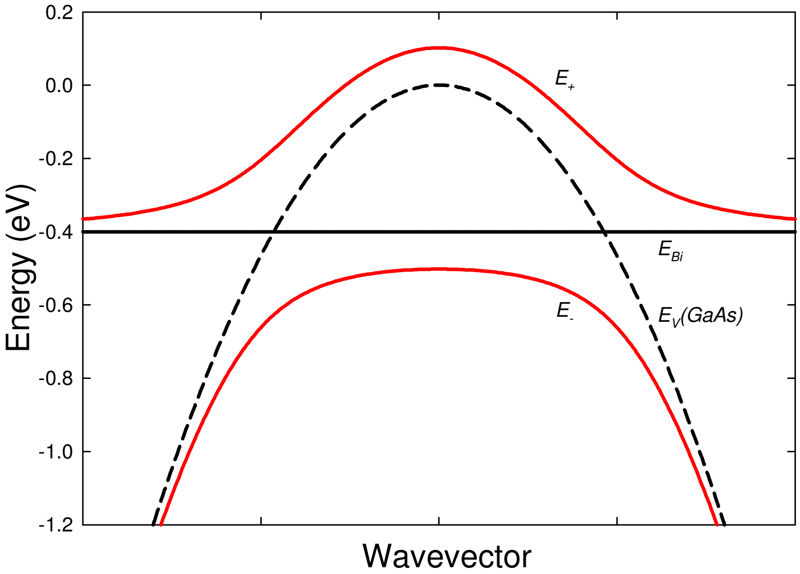

Figure 1.6 The calculated valence band structure of $GaAs_{0.98}Bi_{0.02}$ using the VBAC model. The solid black and dashed lines refer to the Bi level and the valence band edge of GaAs, respectively.

If the conduction band is assumed to be unaffected, since the Bi level is located at much lower energy than the conduction band, the band gap of $GaAs_{1-x}Bi_x$ is given by,

$$E_g(GaAsBi) = E_c(GaAs) - E_+(GaAsBi) \ , \tag{1.3}$$

which can be simplified to

$$E_g(GaAsBi) = E_g(GaAs) - \Delta E_{VBAC} \ , \tag{1.4}$$

where ΔE_{VBAC} refers to the band gap reduction due to Bi incorporation, which is,

$$\Delta E_{VBAC} = \frac{\Delta E_{VBM-Bi}}{2}\left[\sqrt{1+4x\left(\frac{C_{Bi}}{\Delta E_{VBM-Bi}}\right)^2}-1\right] \tag{1.5}$$

The full derivation for Equation 1.4 and 1.5 are shown in Appendix A.

1.4 Thesis overview

The motivation and benefits of the $GaAs_{1-x}Bi_x$ alloy have been outlined earlier in this chapter. Since $GaAs_{1-x}Bi_x$ is a relatively new alloy, this thesis will be dedicated to the growth and characterization of this material system. Three main areas have been identified for investigation, which are:

- The effects of Bi incorporation on the optical properties of $GaAs_{1-x}Bi_x$
- Annealing study and the origin of optical quality improvement
- The effects of growth parameters on $GaAs_{1-x}Bi_x$ grown by MBE

Chapter 2 explains the growth and characterisation techniques used in this work. The basics of MBE growth and its in-situ monitoring system will be discussed. The principles of high resolution X-ray diffraction (HR-XRD) and PL will be explained.

Chapter 3 focuses on the PL investigation of $GaAs_{1-x}Bi_x$ with a wide range of Bi compositions. Particular attention is given to band gap temperature dependence, localization effects, PL full-width-at-half-maximum (FWHM), dominant recombination mechanism(s) at different temperatures and excitation powers and mechanisms of enhanced room temperature PL.

Chapter 4 examines the influence of rapid thermal annealing on the optical and structural properties of $GaAs_{1-x}Bi_x$ alloys. Samples were annealed at various annealing temperatures and annealing times. The origin of the PL improvement induced by thermal annealing also will be discussed.

Results in Chapter 3 and 4 showed that growth optimizations are needed to improve wafer quality. Thus, a study on the effects of growth parameters on the optical and structural quality of $GaAs_{1-x}Bi_x$ was carried out and reported in Chapter 5. Two growth parameters were investigated which are growth rate and As_4/Bi beam equivalent pressure ratio.

Chapter 6 summarizes all the results and provides suggestions for future work.

1.5 References

[1] D.R. Goff. *A Brief History of Optical Fibre*. http://www.olson-technology.com/mr_fiber/fiber-history.htm 2003.

[2] B. Zhao and A. Yariv, *Semiconductor lasers I : Fundamentals*, editted by. E. Kapon. 1999 Academic Press.

[3] G.N. Childs, S. Brand, and R.A. Abram, "Intervalence band absorption in semiconductor laser materials", *Semiconductor Science and Technology,* vol. **1**, pp. 116, 1986.

[4] P.J.A. Thijs, L.F. Tiemeijer, P.I. Kuindersma, J.J.M. Binsma, and T. Van Dongen, "High-performance 1.5 µm wavelength InGaAs-InGaAsP strained quantum well lasers and amplifiers", *Quantum Electronics, IEEE Journal of,* vol. **27**, pp. 1426-1439, 1991.

[5] J.P. Loehr and J. Singh, "Effect of strain on CHSH Auger recombination in strained $In_{0.53}Ga_{0.47}As$ on InP", *Quantum Electronics, IEEE Journal of,* vol. **29**, pp. 2583-2588, 1993.

[6] A.F. Phillips, S.J. Sweeney, A.R. Adams, and P.J.A. Thijs, "The temperature dependence of 1.3- and 1.5 µm compressively strained InGaAs(P) MQW semiconductor lasers", *Selected Topics in Quantum Electronics, IEEE Journal of,* vol. **5**, pp. 401-412, 1999.

[7] N. Tansu, Y. Jeng-Ya, and L.J. Mawst, "High-performance 1200-nm InGaAs and 1300-nm InGaAsN quantum-well lasers by metalorganic chemical vapor deposition", *IEEE Journal of Selected Topics in Quantum Electronics,* vol. **9**, pp. 1220-1227, 2003.

[8] N. Chand, E.E. Becker, J.P. van der Ziel, S.N.G. Chu, and N.K. Dutta, "Excellent uniformity and very low (< 50 A/cm^2) threshold current density strained InGaAs quantum well diode lasers on GaAs substrate", *Applied Physics Letters,* vol. **58**, pp. 1704-1706, 1991.

[9] M. Kondow, K. Uomi, A. Niwa, T. Kitatani, S. Watahiki, and Y. Yazawa, "GaInNAs: A Novel Material for Long-Wavelength-Range Laser Diodes with Excellent High-Temperature Performance", *Japanese Journal of Applied Physics,* vol. **35**, pp. 1273 - 1275, 1996.

[10] L. Bellaiche, "Band gaps of lattice-matched (Ga,In)(As,N) alloys", *Applied Physics Letters,* vol. **75**, pp. 2578-2580, 1999.

[11] S. Tixier, M. Adamcyk, T. Tiedje, S. Francoeur, A. Mascarenhas, P. Wei, and F. Schiettekatte, "Molecular beam epitaxy growth of $GaAs_{1-x}Bi_x$", *Applied Physics Letters,* vol. **82**, pp. 2245-2247, 2003.

[12] W. Shan, W. Walukiewicz, J.W. Ager Iii, E.E. Haller, J.F. Geisz, D.J. Friedman, J.M. Olson, and S.R. Kurtz, "Band Anticrossing in GaInNAs Alloys", *Physical Review Letters,* vol. **82**, pp. 1221-1224, 1999.

[13] M. Kondow, T. Kitatani, S. Nakatsuka, M.C. Larson, K. Nakahara, Y. Yazawa, M. Okai, and K. Uomi, "GaInNAs: A novel material for long-wavelength semiconductor lasers", *IEEE Journal on Selected Topics in Quantum Electronics,* vol. **3**, pp. 719-729, 1997.

[14] J. J. S. Harris, "GaInNAs long-wavelength lasers: progress and challenges", *Semiconductor Science and Technology,* vol. **17**, pp. 880-891, 2002.

[15] J.A. Gupta, G.I. Sproule, X. Wu, and Z.R. Wasilewski, "Molecular beam epitaxy growth of GaInNAs(Sb) double quantum wells with bright and narrow photoluminescence", *Journal of Crystal Growth,* vol. **291**, pp. 86-93, 2006.

[16] S. Spruytte, C. Coldren, J. Harris, W. Wampler, P. Krispin, K. Ploog, and M. Larson, "Incorporation of nitrogen in nitride-arsenides: Origin of improved luminescence efficiency after anneal", *Journal of Applied Physics,* vol. **89**, pp. 4401, 2001.

[17] S.M. Wang, Y.Q. Wei, X.D. Wang, Q.X. Zhao, M. Sadeghi, and A. Larsson, "Very low threshold current density 1.3 μm GaInNAs single-quantum well lasers grown by molecular beam epitaxy", *Journal of Crystal Growth,* vol. **278**, pp. 734-738, 2005.

[18] H.P. Xin, K.L. Kavanagh, M. Kondow, and C.W. Tu, "Effects of rapid thermal annealing on GaInNAs/GaAs multiple quantum wells", *Journal of Crystal Growth,* vol. **201–202**, pp. 419-422, 1999.

[19] J.S. Harris Jr, "The opportunities, successes and challenges for GaInNAsSb", *Journal of Crystal Growth,* vol. **278**, pp. 3-17, 2005.

[20] S.R. Bank, B. Hopil, L.L. Goddard, H.B. Yuen, M.A. Wistey, R. Kudrawiec, and J.S. Harris, "Recent Progress on 1.55 μm Dilute-Nitride Lasers", *IEEE Journal of Quantum Electronics,* vol. **43**, pp. 773-785, 2007.

[21] Y. Arakawa and H. Sakaki, "Multidimensional quantum well laser and temperature dependence of its threshold current", *Applied Physics Letters,* vol. **40**, pp. 939-941, 1982.

[22] M. Asada, Y. Miyamoto, and Y. Suematsu, "Gain and the threshold of three-dimensional quantum-box lasers", *IEEE Journal of Quantum Electronics,* vol. **22**, pp. 1915-1921, 1986.

[23] G.T. Liu, A. Stintz, H. Li, T.C. Newell, A.L. Gray, P.M. Varangis, K.J. Malloy, and L.F. Lester, "The influence of quantum-well composition on the performance of quantum dot lasers using InAs-InGaAs dots-in-a-well (DWELL) structures", *IEEE Journal of Quantum Electronics,* vol. **36**, pp. 1272-1279, 2000.

[24] D. Bimberg and C. Ribbat, "Quantum dots: lasers and amplifiers", *Microelectronics Journal,* vol. **34**, pp. 323-328, 2003.

[25] Y. Tanaka, M. Ishida, K. Takada, Y. Maeda, T. Akiyama, T. Yamamoto, H.Z. Song, M. Yamaguchi, Y. Nakata, K. Nishi, M. Sugawara, and Y. Arakawa. "1.3 μm InAs/GaAs high-density quantum dot lasers". in *IEEE LEOS Annual Meeting Conference Proceedings*, Antalya, 2009

[26] M.V. Maximov, V.M. Ustinov, A.E. Zhukov, N.V. Kryzhanovskaya, A.S. Payusov, I.I. Novikov, N.Y. Gordeev, M.S. Yu, I. Krestnikov, D. Livshits, S. Mikhrin, and A. Kovsh, "A 1.33 μm InAs/GaAs quantum dot laser with a 46 cm^{-1} modal gain", *Semiconductor Science and Technology,* vol. **23**, pp. 105004, 2008.

[27] D. Bimberg, M. Grundmann, F. Heinrichsdorff, N.N. Ledentsov, V.M. Ustinov, A.E. Zhukov, A.R. Kovsh, M.V. Maximov, Y.M. Shernyakov, B.V. Volovik, A.F. Tsatsul'nikov, P.S. Kop'ev, and Z.I. Alferov, "Quantum dot lasers: Breakthrough in optoelectronics", *Thin Solid Films,* vol. **367**, pp. 235-249, 2000.

[28] B. Joukoff and A.M. Jean-Louis, "Growth of $InSb_{1-x}Bi_x$ single crystals by Czochralski method", *Journal of Crystal Growth,* vol. **12**, pp. 169-172, 1972.

[29] J.J. Lee, J.D. Kim, and M. Razeghi, "Growth and characterization of InSbBi for long wavelength infrared photodetectors", *Applied Physics Letters,* vol. **70**, pp. 3266-3268, 1997.

[30] A.J. Noreika, W.J. Takei, M.H. Francombe, and C.E.C. Wood, "Indium antimonide-bismuth compositions grown by molecular beam epitaxy", *Journal of Applied Physics,* vol. **53**, pp. 4932-4937, 1982.

[31] Z.M. Fang, K.Y. Ma, R.M. Cohen, and G.B. Stringfellow, "Photoluminescence of InAsBi and InAsSbBi grown by organometallic vapor phase epitaxy", *Journal of Applied Physics,* vol. **68**, pp. 1187-1191, 1990.

[32] K. Oe and H. Okamoto, "New semiconductor alloy GaAsBi grown by Metal Organic Vapor Phase Epitaxy", *Japanese Journal of Applied Physics,* vol. **37**, pp. L1283, 1998.

[33] I. Vurgaftman, J.R. Meyer, and L.R. Ram-Mohan, "Band parameters for III-V compound semiconductors and their alloys", *Journal of Applied Physics,* vol. **89**, pp. 5815-5875, 2001.

[34] A. Mascarenhas, Y. Zhang, J. Verley, and M.J. Seong, "Overcoming limitations in semiconductor alloy design", *Superlattices and Microstructures,* vol. **29**, pp. 395-404, 2001.

[35] D.L. Young, J.F. Geisz, and T.J. Coutts, "Nitrogen-induced decrease of the electron effective mass in $GaAs_{1-x}N_x$ thin films measured by thermomagnetic transport phenomena", *Applied Physics Letters,* vol. **82**, pp. 1236-1238, 2003.

[36] K.H. Ploog and O. Brandt. "Doping of group III nitrides". San Jose, California (USA), 1998

[37] S. Tixier, M. Adamcyk, E.C. Young, J.H. Schmid, and T. Tiedje, "Surfactant enhanced growth of GaNAs and InGaNAs using bismuth", *Journal of Crystal Growth,* vol. **251**, pp. 449-454, 2003.

[38] A. Janotti, S.H. Wei, and S.B. Zhang, "Theoretical study of the effects of isovalent coalloying of Bi and N in GaAs", *Physical Review B* vol. **65**, pp. 1152031-1152035, 2002.

[39] M. Yoshimoto, S. Murata, A. Chayahara, Y. Horino, J. Saraie, and K. Oe, "Metastable GaAsBi Alloy Grown by Molecular Beam Epitaxy", *Japanese Journal of Applied Physics,* vol. **42**, pp. L1235-37, 2003.

[40] F. Bastiman, A.R.B. Mohmad, J.S. Ng, J.P.R. David, and S.J. Sweeney, "Non-stoichiometric GaAsBi/GaAs (100) molecular beam epitaxy growth", *Journal of Crystal Growth,* vol. **338**, pp. 57-61, 2012.

[41] R.B. Lewis, M. Masnadi-Shirazi, and T. Tiedje, "Growth of high Bi concentration $GaAs_{1-x}Bi_x$ by molecular beam epitaxy", *Applied Physics Letters,* vol. **101**, pp. 082112-4, 2012.

[42] D.C. Look, "Molecular beam epitaxial GaAs grown at low temperatures", *Thin Solid Films,* vol. **231**, pp. 61-73, 1993.

[43] X. Lu, D.A. Beaton, R.B. Lewis, T. Tiedje, and Y. Zhang, "Composition dependence of photoluminescence of $GaAs_{1-x}Bi_x$ alloys", *Applied Physics Letters,* vol. **95**, pp. 041903, 2009.

[44] R.B. Lewis, D.A. Beaton, X. Lu, and T. Tiedje, "$GaAs_{1-x}Bi_x$ light emitting diodes", *Journal of Crystal Growth,* vol. **311**, pp. 1872-1875, 2009.

[45] N. Hossain, I.P. Marko, S.R. Jin, K. Hild, S.J. Sweeney, R.B. Lewis, D.A. Beaton, and T. Tiedje, "Recombination mechanisms and band alignment of $GaAs_{1-x}Bi_x$/GaAs light emitting diodes", *Applied Physics Letters,* vol. **100**, pp. 051105-3, 2012.

[46] C. J. Hunter, F. Bastiman, A. R. Mohmad, R. Richards, R. Beanland, and J.P.R. David, "Structural study of bulk GaAsBi/GaAs heterostructures ", *in preparation for Journal of Crystal Growth,* vol.,2013.

[47] Y. Tominaga, K. Oe, and M. Yoshimoto, "Low Temperature Dependence of Oscillation Wavelength in GaAsBi Laser by Photo-Pumping", *Applied Physics Express,* vol. **3**, pp. 062201, 2010.

[48] C.J. Hunter, F. Bastiman, A.R. Mohmad, R. Richards, J.S. Ng, S.J. Sweeney, and J.P.R. David, "Absorption Characteristics of $GaAs_{1-x}Bi_x$\GaAs Diodes in the Near-Infrared", *Photonics Technology Letters, IEEE,* vol. **24**, pp. 2191-2194, 2012.

[49] J.S. Ng, W.M. Soong, M.J. Steer, M. Hopkinson, J.P.R. David, J. Chamings, S.J. Sweeney, and A.R. Adams, "Long wavelength bulk GaInNAs p-i-n photodiodes lattice matched to GaAs", *Journal of Applied Physics,* vol. **101**, pp. 064506-6, 2007.

[50] J. Singh, *Semiconductor Optoelectronics: Physics and Technology*, editted. 1995, New York McGraw Hill.

[51] C.J. Hunter and F. Bastiman, *Electrical characterisation of GaAsBi pin diodes, Unpublished results*, 2012.

[52] G. Pettinari, A. Patane, A. Polimeni, M. Capizzi, X. Lu, and T. Tiedje, "Bi-induced p-type conductivity in nominally undoped Ga(AsBi)", *Applied Physics Letters,* vol. **100**, pp. 092109-4, 2012.

[53] D.J. Friedman, J.F. Geisz, S.R. Kurtz, and J.M. Olson, "1-eV solar cells with GaInNAs active layer", *Journal of Crystal Growth,* vol. **195**, pp. 409-415, 1998.

[54] S.J. Sweeney and S.R. Jin, "Bismide-nitride alloys: Promising for efficient light emitting devices in the near- and mid-infrared", *Journal of Applied Physics,* vol. **113**, pp. 043110-6, 2013.

[55] S. Francoeur, M.J. Seong, A. Mascarenhas, S. Tixier, M. Adamcyk, and T. Tiedje, "Band gap of $GaAs_{1-x}Bi_x$, $0<x<3.6\%$", *Applied Physics Letters,* vol. **82**, pp. 3874-3876, 2003.

[56] W. Huang, K. Oe, G. Feng, and M. Yoshimoto, "Molecular-beam epitaxy and characteristics of $GaN_yAs_{1-x-y}Bi_x$", *Journal of Applied Physics,* vol. **98**, pp. 053505-6, 2005.

[57] K. Alberi, O.D. Dubon, W. Walukiewicz, K.M. Yu, K. Bertulis, and A. Krotkus, "Valence band anticrossing in $GaBi_xAs_{1-x}$", *Applied Physics Letters,* vol. **91**, pp. 051909-3, 2007.

[58] Y. Zhang, A. Mascarenhas, and L.W. Wang, "Similar and dissimilar aspects of III-V semiconductors containing Bi versus N", *Physical Review B,* vol. **71**, pp. 155201, 2005.

[59] K. Oe, "Characteristics of Semiconductor Alloy $GaAs_{1-x}Bi_x$", *Japanese Journal of Applied Physics,* vol. **41**, pp. 2801, 2002.

[60] K. Satzke, G. Weiser, R. Hoger, and W. Thulke, "Absorption and electroabsorption spectra of an $In_{1-x}Ga_xP_{1-y}As_y$/InP double heterostructure", *Journal of Applied Physics,* vol. **63**, pp. 5485-5490, 1988.

[61] Y. Yamazoe, T. Nishino, and Y. Hamakawa, "Electroreflectance study of InGaAsP quaternary alloys lattice matched to InP", *IEEE Journal of Quantum Electronics,* vol. **17**, pp. 139-144, 1981.

[62] B. Gönül, "The analysis of the variation of the threshold current with pressure in semiconductor quantum well lasers", *Semiconductor Science and Technology,* vol. **14**, pp. 648, 1999.

[63] A. Sugimura, "Comparison of band-to-band Auger processes in InGaAsP", *Quantum Electronics, IEEE Journal of,* vol. **19**, pp. 930-932, 1983.

[64] S.J. Sweeney. "Bismide-alloys for higher efficiency infrared semiconductor lasers". in *22nd IEEE International Semiconductor Laser Conference (ISLC)*, Kyoto, 2010

[65] K.J. Cheetham, A. Krier, I.P. Marko, A. Aldukhayel, and S.J. Sweeney, "Direct evidence for suppression of Auger recombination in GaInAsSbP/InAs mid-infrared light-emitting diodes", *Applied Physics Letters,* vol. **99**, pp. 141110-3, 2011.

[66] M. Usman, C.A. Broderick, A. Lindsay, and E.P. O'Reilly, "Tight-binding analysis of the electronic structure of dilute bismide alloys of GaP and GaAs", *Physical Review B,* vol. **84**, pp. 245202, 2011.

Chapter 2

MBE Growth and Characterisation Techniques

Epitaxial growth can be done by several techniques such as liquid phase epitaxy (LPE), molecular beam epitaxy (MBE) and metal-organic vapour phase epitaxy (MOVPE). In the early development of semiconductor devices, LPE was the preferred choice. More recently, MBE has become commonly used in research environments while MOVPE is widely used in industry. The growth of $GaAs_{1-x}Bi_x$ has been demonstrated by both MBE and MOVPE [1, 2]. This chapter introduces the basics of MBE growth and the characterisation tools used to analyse the $GaAs_{1-x}Bi_x$ alloy.

2.1 Molecular beam epitaxy

2.1.1 Molecular beam epitaxy system

MBE is an epitaxial growth process involving the reaction of atomic or molecular beams with a crystalline surface under ultra-high vacuum (UHV) environment [3]. This technique was developed by A. Y. Cho at Bell Laboratories in the late 1960s and growth of GaAs by MBE was demonstrated in 1971 [4, 5]. The technique was initially used to study the semiconductor surfaces and thin films but later employed for the growth of practical devices such as optoelectronic devices. MBE is the preferred technique for research due to its ability to produce atomically abrupt interfaces, achieve precise control of growth thickness (down to monolayer accuracy) and produce precise compositions and high quality semiconductor layers.

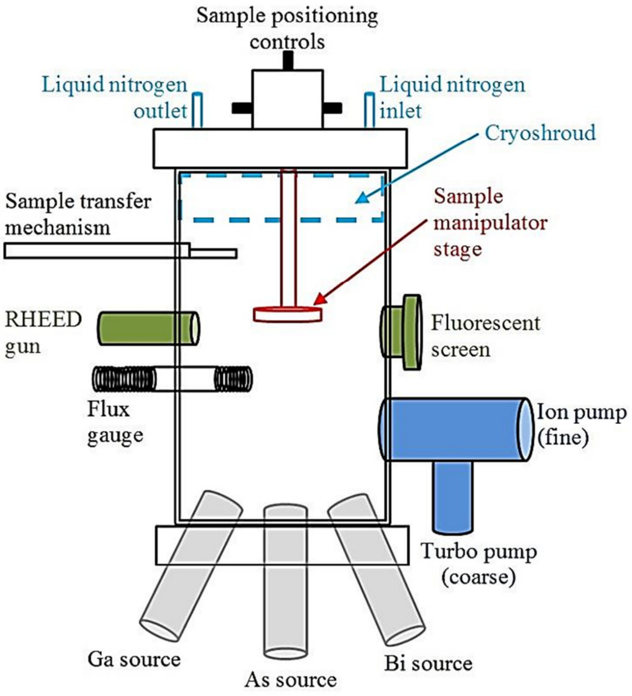

Figure 2.1 Schematic diagram of the growth chamber of the MBE-STM machine.

In this work, an Omicron MBE – scanning tunnelling microscopy (STM) system with gate-valve isolated MBE and the STM chambers was used. The MBE side has two main chambers which are the Fast Entry Lock (FEL) and the growth chamber. The chambers are isolated from each other by a gate-valve. A schematic diagram of the growth chamber of the MBE-STM system is shown in Figure 2.1. Wafers enter and leave the system through the FEL (not shown). The FEL is pumped down from atmospheric pressure to 10^{-9} mBar in approximately 30 minutes by a turbo pump. The substrate is then transferred to the growth chamber.

The growth chamber has an ion pump which reduces the pressure further to 10^{-10} mBar. Maintaining a good UHV environment in the growth chamber is important as it will affect the purity of the grown sample. At a background pressure of $\sim 10^{-10}$ mBar the mean free path of particles is of the order of a few kilometres. When pressure increases up to 10^{-5} mBar during growth (mainly due to arsenic flux) the mean free path reduces, but it remains much longer than the distance between the source and the substrate (~ 30 cm). Therefore, the travelling source fluxes are unlikely to encounter collisions with other particles before reaching the sample.

A cryoshroud (a vessel inside the system which is filled with liquid nitrogen) located on top of the growth chamber also acts as a pump. Most of the impurity gaseous will condense on the cold cryoshroud surface, reducing the background pressure. All source fluxes which did not hit the sample during growth (the source beam is larger than the sample) will also condense on the cryoshroud surface, preventing them from bouncing around and eventually condensing elsewhere.

The sources are at an angle pointing towards the substrates to allow source fluxes to reach the sample. An individual mechanical shutter or valve is used to switch fluxes in and out as needed. This mechanism is sufficient to obtain an epilayer with atomically abrupt interfaces since the time it takes to grow a monolayer is much longer than the shuttering time.

An ion gauge is used to measure and calibrate the group III and V source fluxes. The ion gauge measures the beam equivalent pressure (BEP) which is a relative measure of the beam flux. Measurement is generally carried out before every deposition run. For dopant sources, the flux is too small to be measured by the ion gauge, therefore, an ex-situ calibration is required such as Secondary Ion Mass Spectroscopy (SIMS).

2.1.2 Group III and V sources

Knudsen effusion cells are used to create the molecular beams. The Omicron MBE-STM system has six cells; gallium, indium, aluminium (installed in June 2012), bismuth, arsenic (cracker installed in August 2011) and a dual-dopant source (silicon and beryllium). However, this work uses only gallium, bismuth and arsenic sources. Highly purity 6N5 materials (99.99995 % pure) are used for sources and are placed inside crucibles made from pyrolytic boron nitride (PBN).

The gallium source is a simple Knudsen cell. The cell has a resistive heater coil which provides the thermal energy to melt and evaporate the gallium. The cell is also integrated with a shutter and a water-cooling shroud to maintain a stable cell temperature. For the bismuth source, a dual-filament cell is used. This cell has two heating filaments which are located at the base and the tip of the crucible. The temperature of the top filament is ~ 150 ^{o}C hotter than the bottom filament. For a single filament cell, the lip of the crucible may be colder than the base. Therefore, material re-condensation at the lip of the crucible may occur, leading to the formation of small metal beads. The metal beads can drop back into the source melt and then be sprayed onto the substrate during growth, creating oval defects [6]. The presence of the top heating filament in a dual-filament cell ensures the lip of the crucible remains hot and prevents bismuth re-condensation at the lip, reducing the possibility of oval defects.

The arsenic source consists of two zones which are a sublimator and a cracker. The temperature of the sublimator is typically set between 350 – 450 ^{o}C in order to sublime the arsenic to As_4. The cracker zone will then thermally ‘crack’ the As_4 to As_2 at temperature between 800 to 1000 ^{o}C. The two zones are separated by a needle valve. Since the sublimator zone is quite big, its large thermal mass does not allow rapid variation of the arsenic flux by varying the cell temperature. Therefore, the needle valve opening is adjusted to control the arsenic flux while the temperature of the sublimator is kept constant. If the cracker temperature is set lower than 800 ^{o}C, the arsenic cracking efficiency will drop, causing the arsenic flux to be dominated by As_4. It has been shown that growth utilizing As_2 will have better quality and higher PL intensity compared to growth utilising As_4 [7]. As_2 is also more reactive and requires lower growth temperature compared to As_4 [7].

2.1.3 Substrate cleaning and buffer growth

The samples were grown on pieces cleaved from semi-insulating GaAs (100) substrates. The substrates were cleaved in two different sizes, 11.0 × 3.5 mm^2 or 11.4 × 11.8 mm^2 depending on the substrate holder. The former was used for most of the samples grown before June 2011. A new substrate holder was then designed by F. Bastiman in order to accommodate a bigger substrate size. The cleaved substrate was degreased and cleaned thoroughly to remove dust which was produced during the cleaving process. The substrate piece was cleaned using cotton buds dipped in n-butyl acetate. The substrate surface was wiped gently from the centre to the edges and then dried by blowing with nitrogen gas. Finally, the substrate was placed under a microscope to check the cleanliness. The cleaning procedures may be repeated if necessary.

After the substrate has been loaded into the growth chamber it was outgassed at ~ 400 ^{o}C for 30 minutes to desorb water vapour and other volatile contaminants. The surface of the epi-ready substrate is coated with a layer of protective oxide which must be removed before growth. Therefore, the substrate was heated to 580 – 620 ^{o}C under arsenic flux in order to remove the oxide. The reflection high-energy electron diffraction (RHEED) pattern was used to monitor the oxide removal process. After oxide removal, the substrate surface is relatively smooth with deformation heights of 5 – 20 nm [8].

Then, a GaAs buffer of 0.3 - 0.5 μm thickness was grown at 580 – 620 ^{o}C to bury any defects and provide an atomically flat surface for epilayer growth. The GaAs was grown with an As_2 BEP of ~ 15 times larger than the gallium BEP. The growth rate of GaAs (and other III-V semiconductors) is controlled by the group III element(s) due to their unity sticking coefficient. Higher flux (thus higher growth rate) is achieved by increasing the gallium cell temperature. For the MBE-STM system, changing the gallium cell temperature from 900 to 1030 ^{o}C typically leads to an increase of GaAs growth rate from 0.1 to 1 μm/h.

A smoother surface will be obtained if the oxide is removed via the gallium-assisted oxide desorption technique to allow a thinner buffer layer (~ 80 nm) [9]. However, it requires prior native oxide thinning by HCl and a precise amount of gallium during oxide removal. This technique was used in many of the early samples. Later, the conventional method became the preferred choice due to its simplicity. For more details on the gallium-assisted oxide removal technique the readers are referred to Ref. [9].

Rotating the substrate during growth is important in order to ensure the uniformity of thickness and composition across the grown layer. However, the MBE-STM system used in this work does not have a substrate rotation mechanism. Since this work uses relatively small substrates, composition uniformity across the sample (checked by PL) was achieved without rotation.

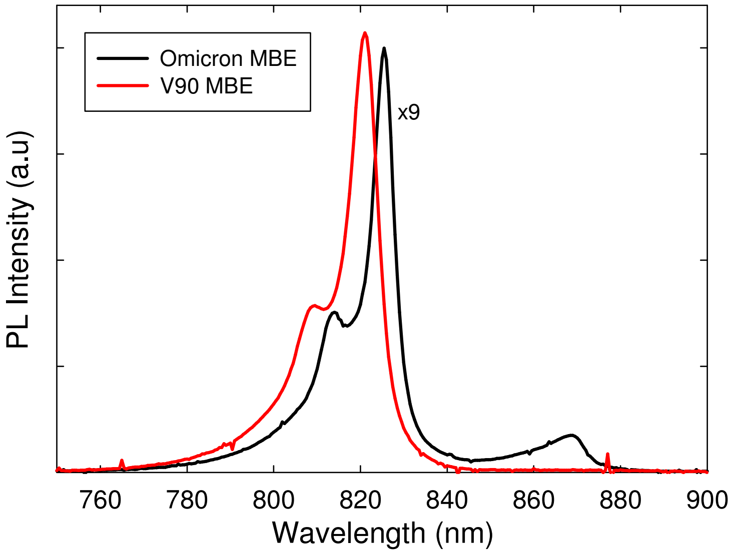

Figure 2.2 Room temperature PL comparisons for samples grown by Omicron MBE and standard V90 MBE.

Since the Omicron MBE is not a standard machine and requires additional steps prior to growth a control sample was grown and the optical quality is compared to a sample grown by a standard V90 MBE. Figure 2.2 shows the room temperature PL spectra of the control samples (GaAs/$Al_{0.4}Ga_{0.6}As$ 10-period quantum wells) grown by both machines. The thickness of the GaAs wells and $Al_{0.4}Ga_{0.6}As$ barriers are ~ 6 and 10 nm, respectively. However, the Omicron's control sample uses an S.I substrate while the V90's control sample uses an n+ substrate. The PL intensity of the sample grown by the Omicron is ~ 9 times lower compared to the sample grown by the V90. This is due to higher background pressure inside the growth chamber as a result of substrate outgassing. The substrate outgassing was also carried out for a short period of time which is 30 minutes. However, for the V90 MBE, substrate outgassing was carried out inside a dedicated area called the 'preparation chamber' which preserves a good background pressure inside the growth chamber. This is typically carried out simultaneously while another sample is being grown inside the growth chamber and for a longer period of time (2 hours). Besides, the cleaving process and extra cleaning steps may also contribute to a higher density of defects in the Omicron control sample.

2.1.4 Growth of GaAsBi

After the GaAs buffer layer was completed and annealed for 20 minutes, growth was interrupted to prepare for GaAsBi growth. The substrate temperature was reduced from ~ 600 ^{o}C to the growth temperature of the bismide layer which is ≤ 400 ^{o}C. The temperature of the gallium cell was also changed to obtain the required growth rate and the arsenic valve opening was varied to achieve the intended Ga:As BEP ratio. In order to grow GaAsBi using As_4 the temperature of the arsenic cracker was reduced from 1000 to 650 ^{o}C. The use of As_4 allows GaAsBi to be grown at higher growth temperature and higher arsenic overpressure compared to As_2 [10]. The incorporation of As_2 is a simple first-order reaction while the incorporation of As_4 is a second-order reaction which requires the interaction with another tetramer [7]. The Bi flux consists of monomers and dimers [10-12]. The Bi monomers are highly mobile while the dimers can be assumed to incorporate in a similar manner to the As_2 [10]. Therefore, an unstable Bi dimer can easily be dislodged by As_2 while competing for gallium sites. However, for As_4 to occupy the lattice sites, simultaneous dislodging of two adjacent Bi dimers is required [10]. This condition favours the incorporation of Bi in GaAs with the use of As_4.

Prior to GaAsBi growth, the sample's surface was pre-deposited with Bi for 10 seconds and then left for 30 seconds. During this process, the RHEED pattern from the $[\bar{\mathbf{1}}\,\mathbf{1}\,\mathbf{0}]$ azimuth changed from c4 to 3× which is from an As terminated surface to Bi terminated surface (further explanation about RHEED in Section 2.2). This step was carried out to supress the segregation of Bi to the surface during GaAsBi growth. This in turn will reduce the formation of a Bi concentration gradient at the GaAs/GaAsBi interface. Next, the gallium and Bi shutters were opened simultaneously to start the GaAsBi growth (the arsenic valve was open all the time). For the growth of a multiple quantum well structure, Bi pre-deposition was carried out once before the growth of the first quantum well. The RHEED pattern stays 3× (from $[\bar{\mathbf{1}}\,\mathbf{1}\,\mathbf{0}]$ azimuth) throughout the growth of GaAs barriers showing that the surface stays Bi terminated.

After the GaAsBi growth finished, a GaAs capping layer was grown using As_4 at similar growth temperature and growth rate as the GaAsBi layer. The same temperature was used to grow the GaAsBi and the capping layer to avoid unintentional annealing which may lead to the diffusion of Bi atoms to the capping layer. The details of all samples studied in this thesis are summarised in Appendix B.

2.2 Reflection high-energy electron diffraction

Reflection high-energy electron diffraction (RHEED) is a useful in-situ monitoring tool in MBE which provides information on surface structure, surface quality, growth rate and temperature. The system consists of an electron gun and a phosphor screen. An electron beam with energy of 15 – 20 keV strikes the sample surface at an angle of 1 - 3^{o}, before being diffracted by the crystal surface and forming visible diffraction patterns on the phosphor screen. Due to the glancing angle the electrons only penetrate the first few monolayers, so the diffraction patterns are highly sensitive to the surface. RHEED must be performed in a UHV environment to minimise electron scattering.

The RHEED pattern is a series of streaks or spots which correspond to the surface reconstruction of the sample. Reconstruction happens when the surface atoms move and/or re-bond with other atoms in order to minimise the surface energy [13]. A reconstruction pattern is classified by the number of secondary streaks that appear in addition to the primary streak. The pattern which shows the primary streak only is called 1× (one-by) while the pattern with *n* additional streaks in between the primary streaks is called (*n*+1)×. The RHEED pattern is normally denoted as $(a \times b)$, where *a* and *b* is the surface reconstruction from the $[1\,1\,0]$ and $[\bar{1}\,1\,0]$ azimuths, respectively. For example, high quality GaAs is grown with a (2 × 4) surface reconstruction.

The RHEED pattern can be streaky, spotty, hazy or rings. If the RHEED pattern appears spotty (instead of streaky), it indicates that the sample surface is rough. An amorphous surface such as native oxide layer will show a haze while a polycrystalline surface will show rings. Even though the RHEED pattern only provides qualitative information, it offers a quick and useful check on the surface condition.

2.2.1 Temperature Calibration

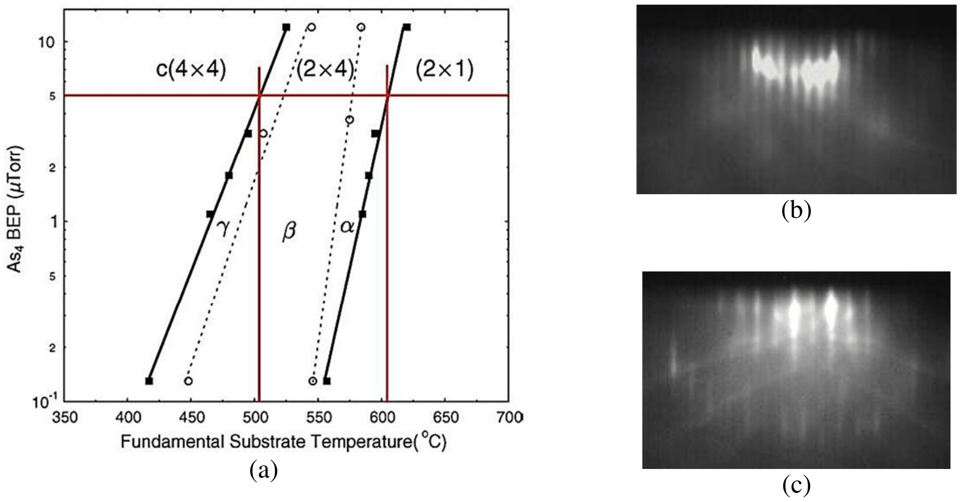

(a)

(b)

(c)

Figure 2.3 (a) Static phase diagram of GaAs versus arsenic BEP and substrate temperature, taken from Ref. [13], (b) and (c) show the RHEED patterns taken from the $[\bar{1}\,1\,0]$ azimuth, showing 4× and c4 patterns, respectively.

RHEED transition	Temperature (^{o}C)	As BEP (μTorr)	Comment
Hazy to c(4 × 4)	~ 290	0	arsenic-cap desorption
c(4 × 4) to (2 × 4)	~ 400	0	Low temperature ref.
c(4 × 4) to (2 × 4)	~ 505	5	Intermediate temperature ref.
Hazy to streaks	580	5	Oxide desorption and clean-up
(2 × 4) to (2 × 1)	~ 605	5	High temperature ref.

Table 2.1 Summary of temperature reference points for temperature calibrations.

In this work, the RHEED patterns of GaAs surface reconstructions were used to calibrate the growth temperatures. The GaAs surface reconstruction is dependent on the substrate temperature and the arsenic overpressure. Therefore, by fixing the arsenic BEP and then varying the substrate heater current, temperature of the substrate can be estimated based on surface reconstruction changes. Figure 2.3 (a) shows the static surface reconstruction map of GaAs against arsenic BEP and substrate temperature taken from Ref. [13]. For an arsenic BEP of 5 μTorr, substrate temperatures of ~ 505 and ~ 605 ^{o}C can be estimated based on surface reconstruction changes from c(4 × 4) to (2 × 4) and (2 × 4) to (2 × 1), respectively. Three other temperature calibration points are 290, 400 [14] and 580 ^{o}C. Table 2.1 summarises the temperature calibration points used in this work. Other temperatures were extrapolated based on these temperature calibration points.

2.2.2 Growth rate calibration

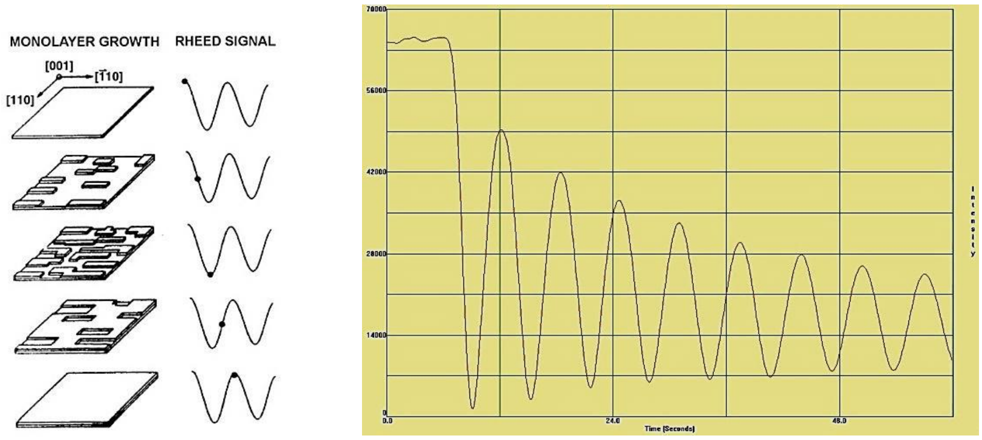

(a) (b)

Figure 2.4 (a) Illustration of the RHEED intensity oscillation during a monolayer growth, taken from Ref. [13], (b) is an example of RHEED oscillations observed during GaAs growth in this work.

The RHEED intensity oscillation provides a quick and accurate measurement of the growth rate. The intensity varies as the surface roughness changes during growth and a complete oscillation corresponds to the growth of a monolayer [13]. When growth initially starts the surface is smooth and the RHEED intensity is high. As islands start to form during growth the RHEED intensity starts to decrease due to the increase of surface roughness. The oscillation intensity is lowest when half of a monolayer is grown. The RHEED intensity starts to recover again when the islands coalesce into a flat layer. This process is illustrated in Figure 2.4.

2.3 High resolution X-ray diffraction

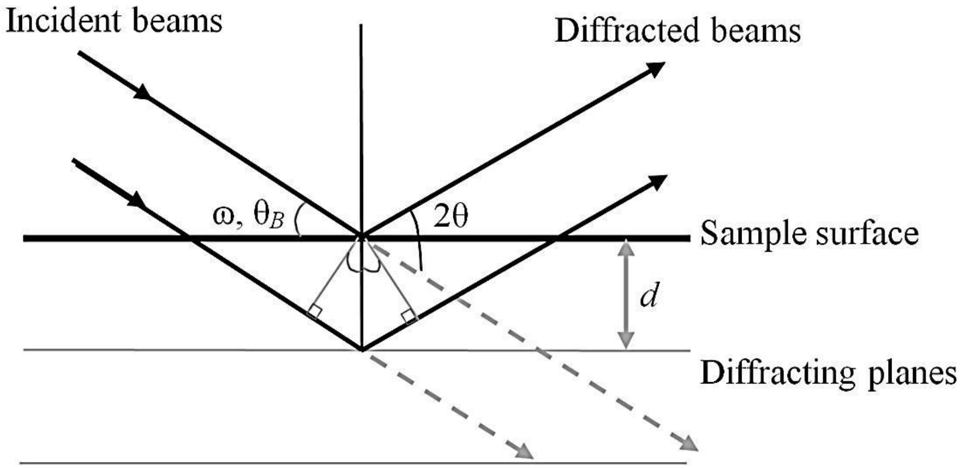

Figure 2.5 Diagram illustrating the diffraction of an X-ray beam on crystal planes.

High resolution X-ray diffraction (HR-XRD) is a powerful non-destructive method to characterise the structural properties of epitaxially grown semiconductor materials. X-rays are suitable for this purpose as their wavelength (1.54 Å for X-rays radiated from copper target) is comparable to the inter-atomic distance in a crystal. X-rays can penetrate deep into the sample and provide information on crystalline quality, layer thickness, alloy composition, mismatch and interface roughness. The most common HR-XRD scan on semiconductor samples is the rocking curve ω-2θ scan diffracted off the (004) plane.

A beam of X-rays incident on a crystal lattice will be diffracted and interfere with each other to form constructive and destructive interference. This phenomenon is shown in Figure 2.5 and can be described by Bragg's law,

$$n\lambda = 2d\sin\theta_B \,, \tag{2.1}$$

where n is an integer, λ is the wavelength of the X-ray, d is the distance between adjacent parallel atomic planes and θ_B is Bragg's angle. Bragg's law states that in order for constructive interference to take place the difference in distance travelled by the incident waves must be an integer multiple of the wavelength of the wave so that the diffracted waves are in phase. Diffractions occurring away from the Bragg's angle will have a much reduced intensity, resulting in the formation of a diffraction peak with a finite linewidth. The higher the number of diffraction planes the higher the diffraction intensity and the narrower the peak. The peak linewidth will eventually approach the bulk crystal limit. The presence of structural defects such as dislocations will broaden the linewidth.

For a strained epilayer grown on a substrate, the rocking curve will show two peaks which correspond to the lattice parameter of the substrate and the epilayer. This is because the lattice cell of the strained epilayer will deform in the vertical direction, resulting in changes to the lattice parameter with respect to the substrate. Different lattice parameters will diffract X-rays at different angles leading to two separate peaks. A large lattice parameter will diffract at a smaller angle leading to negative peak splitting (with respect to the substrate) and vice versa for a smaller lattice parameter. Therefore, a HR-XRD scan in combination with Vegard's law (for the relationship between lattice parameter and alloy composition) is useful to estimate the alloy composition of an epilayer grown on a substrate. The estimation of alloy composition for a ternary compound is straightforward, but becomes increasingly complicated for quarternary and quinary alloys.

In this work, a Bede D1 HR-XRD system was used and is illustrated in Figure 2.6. The X-ray beam was generated in a sealed tube where electrons were accelerated by 50 kV of potential difference before hitting a copper target. The collision results in the radiation of X-ray spectrum consisting of several lines called $K_{\alpha 1}$, $K_{\alpha 2}$ and K_{β}, which each correspond to different electronic transitions. The X-ray beam is non-monochromatic and has large angular divergence (typically 0.1^{o} after passing through a mechanical collimator) which limits the resolution and makes diffraction analysis more complicated [15]. Hence, beam conditioning is required to obtain a monochromatic and highly collimated X-ray beam.

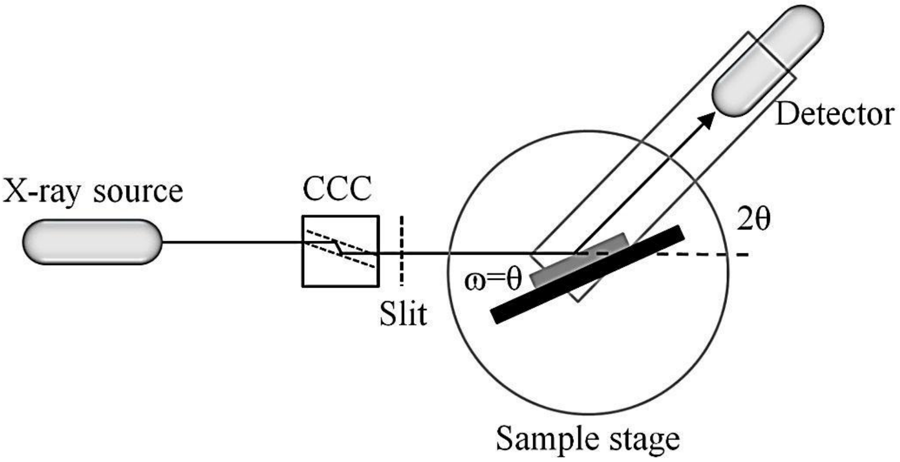

Figure 2.6 Schematic of an HR-XRD experimental setup.

X-ray beam conditioning was achieved by using silicon Channel Crystal Cut (CCC) where the beam undergoes multiple diffractions (2 to 4). This technique produces a high intensity and highly collimated X-ray beam with an angular divergence of 12 arc sec [15]. The Bede D1 system also has a second CCC to further reduce the angular divergence to 5 arc sec but results in the reduction of the X-ray intensity [15]. In this work the single CCC, high intensity configuration is sufficient to obtain the required information. A slit was positioned after the CCC to remove the $K_{\alpha2}$ component. The $K_{\alpha1}$ component is normally used for XRD measurements due to its higher intensity compared to the $K_{\alpha2}$ component.

The sample stage and the detector are mounted on the same rotating arm. During HR-XRD measurements, the position of the X-ray source is fixed while the sample stage and the detector are rotated. The rotational movement of the detector is always double that of the sample in order to satisfy the Bragg condition.

2.4 Photoluminescence

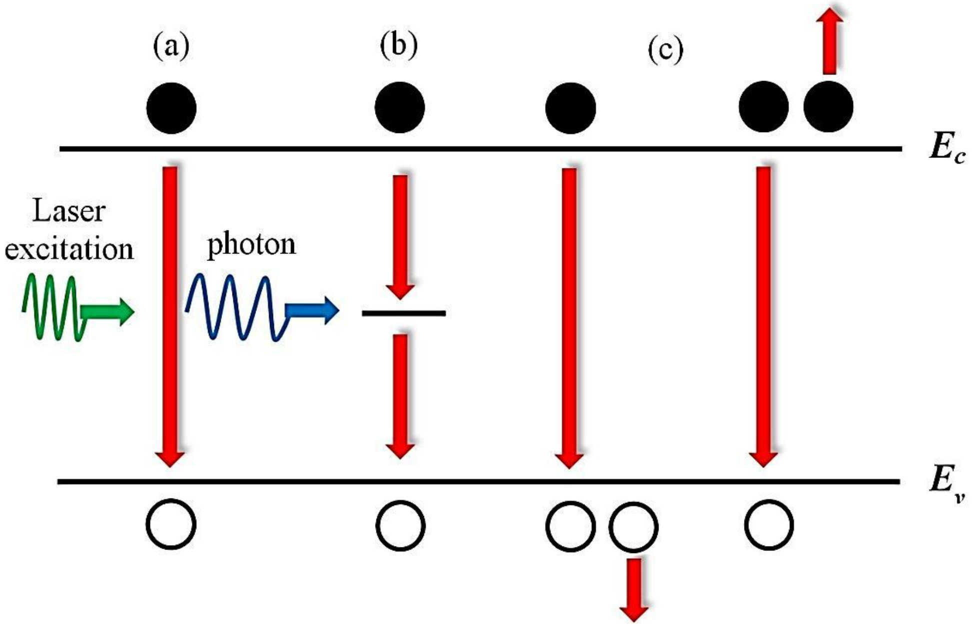

Figure 2.7 Possible carrier recombination processes showing (a) band to band radiative recombination and non-radiative recombination via (b) defect states and (c) Auger processes. E_c and E_v refer to the conduction band and the valence band, respectively.

Photoluminescence spectroscopy is a very sensitive technique for investigating intrinsic electronic transitions and electronic transitions at defects [16]. This technique is also simple, non-destructive and does not require sample preparation. Photoluminescence refers to luminescence excited by incident photons. A typical photon source is a laser. If the energy of a photon is similar to or larger than the band gap of the semiconductor material under test, the photon will be absorbed. An electron will then be promoted from the valence band to the conduction band, creating an electron-hole pair. The electron-hole pair will then undergo scattering events and eventually recombine and emit a photon (or photoluminescence) with an energy which corresponds to the band gap of the material. This process is called band-to-band radiative recombination and is illustrated in Figure 2.7 (a).

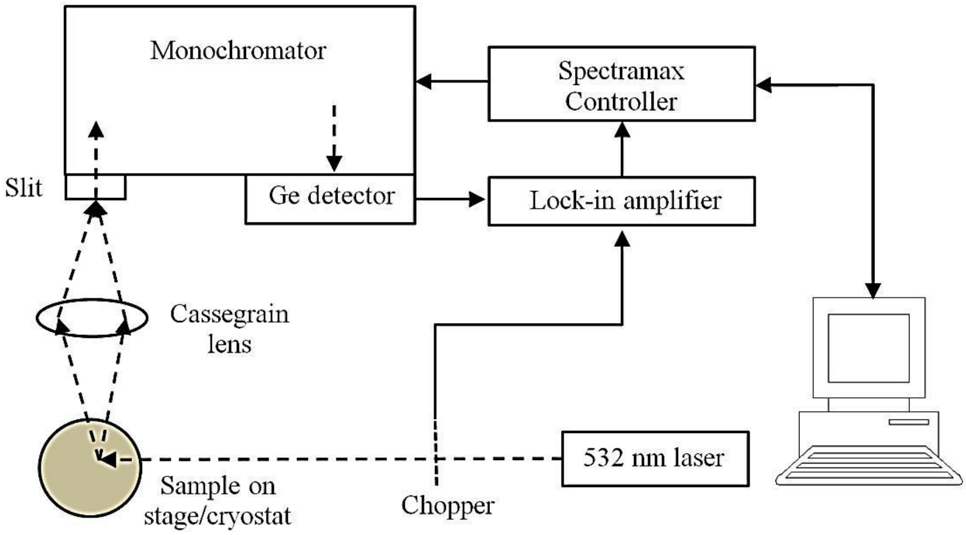

Figure 2.8 Schematic diagram of photoluminescence setup.

The electron-hole pair can also recombine non-radiatively via defect states in the band gap, as shown in Figure 2.7 (b). The presence of defect states could be due to impurities (i.e carbon, oxygen etc) or growth defects (dislocations, point defects etc). For carriers recombined via defect states the energy released will be converted to lattice vibrations and heat which is known as phonons. Therefore, a sample with a high density of defects will have weaker PL intensity.

In the case of Auger recombination, the electron and hole recombine in a band-to-band transition but the energy released is given away to another electron or hole. The high energy (or hot) electron or hole will be promoted higher in the conduction band or deeper in the valence band. The hot carrier will consequently relax to the edge of the conduction band or the valence band when the energy is lost to phonons. Auger recombination becomes more likely at high excitation when more carriers are generated.

Figure 2.8 shows the experimental setup of PL measurements. For measurements at room temperature, the sample was mounted on an XYZ stage for precise positioning and focusing. The excitation source is a 532 nm diode pumped solid state (DPSS) laser with maximum excitation power of 1 Watt. The laser's incident power was measured by a power meter. It was found that the incident power is approximately one-third of the initial laser power. Two-thirds of the laser power is lost due to mirror reflections before reaching the sample. Besides, the output laser power is not accurately set by the control software for the laser power < 100 mW. Therefore, excitation powers of < 100 mW were obtained by setting the laser at high power and then attenuating it by a neutral density (ND) filter whose attenuation factor is known. For example, 30 mW of excitation was obtained by setting the laser at 300 mW and attenuating it by an ND filter with attenuation factor of 10.

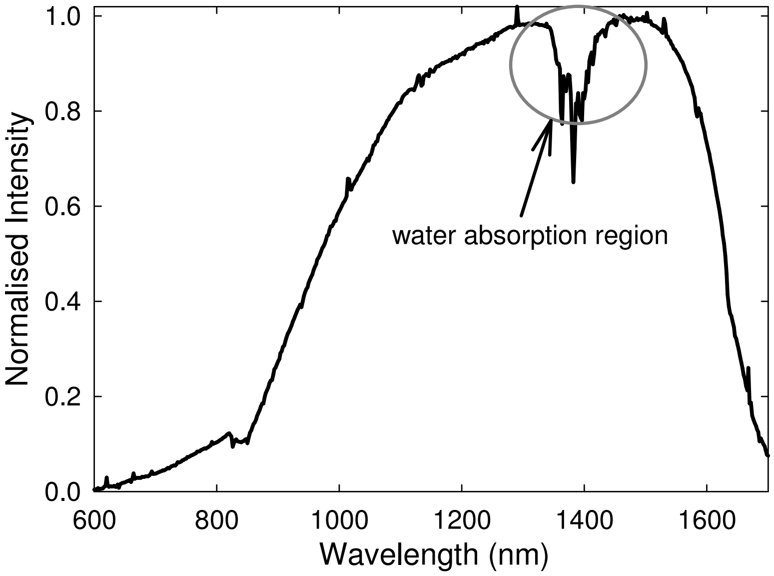

Figure 2.9 The PL system's spectral response.

The laser beam was chopped at 180 Hz which was chosen to avoid the signal being affected by the voltage mains supply (multiples of 50 Hz). The laser's 2nd order excitation (1064 nm) was attenuated by a KG3 filter. The emitted PL was collected by a cassegrain lens and then focused onto the entrance slit of the monochromator. Various slit widths (0.5 to 2 mm) and ND filters were used to enhance weak signals and attenuate strong PL signals. The PL was then detected by a liquid nitrogen cooled germanium detector. The detector was operated at 77 K to reduce its dark current and to increase its detection characteristics. In order to eliminate the contribution from the background light to the measured PL, a phase-sensitive lock-in detection technique was used.

The monochromator has three grating selections: 1200 grooves/mm, 900 grooves/mm and 600 grooves/mm which correspond to blazed wavelength (optimal wavelength) of 330, 850 and 1500 nm, respectively. All PL measurements were carried out using the 900 grooves/mm grating because it gives good efficiency for wavelengths from 850 to 1400 nm. For accurate analysis, the measured PL data were corrected based on the system's spectral response measured using a white light source, as shown in Figure 2.9. The PL system's spectral response depends on the responses of the germanium detector, monochromator grating and the associated optics.

For low temperature measurements, the sample was mounted inside a closed-cycle helium cryostat system which consists of a gas compressor, a temperature controller, a vacuum pump and the cryostat itself. The compressor provides a high pressure gas whose expansion creates a refrigeration effect down to 10 K. The temperature inside the cryostat is controlled by the temperature controller as well as a heater and a temperature sensor in the cryostat.

2.5 Error Analysis

This section will explain the calibration processes and steps taken to estimate and minimise errors during experimental works. For PL setup, the system was calibrated using the laser line (532 nm) with typical error of ± 0.5 nm. This value is small and can be neglected. A reference sample was also used to calibrate the PL intensity which typically varies within ± 5%. For critical measurements, the extra precaution was taken by measuring the samples next to each other. The temperature dependent PL was carried out with temperature variations of ± 0.5 ^{o}C.

For HR-XRD, the positions of ω, 2θ and tilt were optimised before every measurement in order to get the maximum intensity. The measurement step was set between 5 and 8 arc seconds. The measurement step and difficulty in determining the position of the peak (due to the broadness of the spectra) may result in uncertainty in the value of Bi concentration. This uncertainty is estimated to be around ± 0.002 (i.e

0.06 ± 0.002 for a sample with 6% Bi). For very thin GaAsBi layers in which the bismide peak was not obvious, RADS simulation was carried out to verify the Bi composition.

The rapid thermal annealing (RTA) runs were carried out using a standard recipe. This means that all annealing processes use an identical purging procedure, similar durations for temperature ramping up and ramping down and cooling procedure. The wafer should also experience uniform heating as the furnace is a series of heating lamps located on the top and bottom of the quartz chamber. The heating lamps are also monitored and any lamp failures will be flagged by the RTA software. During annealing, the N flow was reduced to 2 litre/min to ensure laminar flow across the wafer to avoid the formation of hot spots. For precaution purposes, the samples were placed more or less in a similar position which is at the centre of the carrier wafer for every annealing run. The temperature variation for the RTA system is estimated to be < 7 ^{o}C. This value is much smaller than the annealing temperature used in this work which is > 600 ^{o}C.

Important parameters for MBE growth include the determination of material fluxes and growth rate. For every flux measurement, the flux gauge was fully inserted and set at similar sensitivity. The flux of each element was measured in the order of Ga, Bi and As. Arsenic was measured last because it will increase the background pressure of the growth chamber. The fluxes reported in this work were determined with an uncertainty of ± 0.1 mBar. The growth rate was determined by averaging the values measured from at least three sets of RHEED oscillations with typical error of ± 0.005 µm/h.

2.6 References

[1] K. Oe, "Metalorganicvapor phase epitaxial growth of metastable $GaAs_{1-x}Bi_x$ alloy", *Journal of Crystal Growth,* vol. **237-239**, pp. 1481, 2002.

[2] S. Tixier, M. Adamcyk, T. Tiedje, S. Francoeur, A. Mascarenhas, P. Wei, and F. Schiettekatte, "Molecular beam epitaxy growth of $GaAs_{1-x}Bi_x$", *Applied Physics Letters,* vol. **82**, pp. 2245-2247, 2003.

[3] A.Y. Cho, "Growth of III–V semiconductors by molecular beam epitaxy and their properties", *Thin Solid Films,* vol. **100**, pp. 291-317, 1983.

[4] A.Y. Cho, "Film Deposition by Molecular-Beam Techniques", *Journal of Vacuum Science and Technology,* vol. **8**, pp. S31-S38, 1971.

[5] A.Y. Cho, "GaAs Epitaxy by a Molecular Beam Method: Observations of Surface Structure on the (001) Face", *Journal of Applied Physics,* vol. **42**, pp. 2074-2081, 1971.

[6] C.T. Lee and Y.C. Chou, "Types of oval defects on GaAs grown by MBE", *Journal of Crystal Growth,* vol. **91**, pp. 169-172, 1988.

[7] C.T. Foxon and B.A. Joyce, *Growth and characterisation of semiconductors*, R.A. Stradling and P.C. Klipstein, Editors. 1990, IOP Publishing Ltd: Bristol.

[8] F. Bastiman, *PhD Thesis, In Situ Surface Studies of III-V Semiconductor Compounds*, in *Department of Electronic and Electrical Engineering* 2010, University of Sheffield.

[9] F. Bastiman, J.C. Lin, A.G. Cullis, R. Hogg, and M. Skolnick, "Ga assisted oxide desorption on GaAs (001) studied by scanning tunnelling microscopy", *Journal of Crystal Growth,* vol. **312**, pp. 1687-1692, 2010.

[10] F. Bastiman, A.R.B. Mohmad, J.S. Ng, J.P.R. David, and S.J. Sweeney, "Non-stoichiometric GaAsBi/GaAs (100) molecular beam epitaxy growth", *Journal of Crystal Growth,* vol. **338**, pp. 57-61, 2012.

[11] R.F.C. Farrow, "The stabilization of metastable phases by epitaxy", *Journal of Vacuum Science & Technology B: Microelectronics and Nanometer Structures,* vol. **1**, pp. 222-228, 1983.

[12] X. Lu, D.A. Beaton, R.B. Lewis, T. Tiedje, and M.B. Whitwick, "Effect of molecular beam epitaxy growth conditions on the Bi content of $GaAs_{1-x}Bi_x$", *Applied Physics Letters,* vol. **92**, pp. 192110, 2008.

[13] V.P. LaBella, M.R. Krause, Z. Ding, and P.M. Thibado, "Arsenic-rich GaAs(0 0 1) surface structure", *Surface Science Reports,* vol. **60**, pp. 1-53, 2005.

[14] K. Regiński, J. Muszalski, V.V. Preobrazhenskii, and D.I. Lubyshev, "Static phase diagrams of reconstructions for MBE-grown GaAs(001) and AlAs(001) surfaces", *Thin Solid Films,* vol. **267**, pp. 54-57, 1995.

[15] D. Ellison, *D1 System : Installation, Operation and Maintenance Manual*, editted. 2004 Bede Scientific Instrument Ltd.

[16] E.C. Lightowlers, *Growth and characterisation of semiconductors*, editted by. R.A. Stradling and P.C. Klipstein. 1990, Bristol IOP Publishing Ltd.

Chapter 3

Photoluminescence Investigation of GaAsBi Alloys

3.1 Motivation

The advantages of Bi for optoelectronic devices have been explained in Chapter 1. Despite these advantages, the optical properties of $GaAs_{1-x}Bi_x$ alloys have not been extensively studied compared to GaNAs. The PL data reported to date have significantly larger full-width-half-maxima (FWHM) than the more established InGaAs, suggesting significant alloy composition fluctuations in the $GaAs_{1-x}Bi_x$ samples [1-3]. It was also suggested that radiative recombination at room temperature is dominated by localised excitons. By comparing the PL emission and linear absorption for sample with $x = 0.04 - 0.05$ at low temperatures, a large Stokes shift was obtained and this value remained at 45 meV from 120 K to room temperature [4]. This is also in agreement with Lu *et al* who observed the shift of the PL peak to higher energies with increasing excitation powers at room temperature [3]. However, these observations are in contradiction with Ref. [5-7] which reported a band-to-band or free exciton recombination at room temperature.

Another peculiar trend is the PL intensity improvement with increasing Bi content up to $x = 0.045$ [3]. Enhanced PL in $GaAs_{1-x}Bi_x$ is highly desirable as it may lead to reduced threshold current densities for laser diodes. It was also suggested that the composition dependent PL enhancement is due to localization effects induced by Bi incorporation, similar to the role of indium in wide-gap InGaN and InAlGaN alloys [3, 8]. This is in contrast to N alloying in GaAs which degrades the optical quality. However, this result is in contrast with Ref. [9] which observed a decreasing

PL intensity with Bi content for *x* up to 0.026, in MOVPE grown samples. To date, the composition dependent PL of $GaAs_{1-x}Bi_x$ has not been verified and the origin of PL intensity enhancement is still not well understood.

In this chapter, a detailed study of PL measured from $GaAs_{1-x}Bi_x$ samples will be reported. The study focuses on localization effects, PL FWHM, band gap temperature dependence and dominant carrier recombination mechanism(s) at different temperatures and excitation powers. The reason for PL intensity enhancement also will be addressed.

3.2 Localization effects in GaAsBi

3.2.1 Description of samples

The semi-insulating GaAs (100) substrate used was cleaved into $11.0 \times 3.5\ mm^2$ pieces (to fit into the substrate holder). After degassing at 400 °C, oxide on the substrate was removed via Ga-assisted oxide desorption, providing a flat growth surface and eliminating the requirement for thick buffer layers [10]. An 80 nm GaAs buffer layer was grown at 585 °C. The active region, a 160 nm $GaAs_{1-x}Bi_x$ layer was grown at 400 °C at a rate of 160 nm per hour. This was followed by an 80 nm GaAs capping layer also grown at 400 °C. The same temperature was used to grow the $GaAs_{1-x}Bi_x$ layer and the GaAs cap to avoid unintentional annealing which may lead to the diffusion of Bi atoms to the GaAs cap. Figure 3.1 shows the structure of the $GaAs_{1-x}Bi_x$ samples. The $GaAs_{1-x}Bi_x$ growth temperature used in this work is higher than those reported in the literature (270 – 380 °C) [1, 2, 11, 12].

Material	Thickness (nm)
GaAs cap	80
$GaAs_{1-x}Bi_x$ layer	160
GaAs buffer	80
S.I (100) GaAs substrate	

Figure 3.1 Sample structure.

This section uses three $GaAs_{1-x}Bi_x$ samples with Bi compositions of 0.014, 0.021 and 0.03. However, particular attention is given to the $GaAs_{0.97}Bi_{0.03}$ sample. Two samples were also used for reference which are 3 μm thick GaAs (grown at the optimal temperature of 580 °C) and 160 nm thick GaAs (grown at 400 °C).

Figure 3.2 shows the HR-XRD spectra of the $GaAs_{0.97}Bi_{0.03}$ sample. The sharp peak located at 0 arcsec corresponds to diffraction from the GaAs buffer layer and the substrate while the peak located at -915 arcsec originated from the bismide layer. The $GaAs_{1-x}Bi_x$ layer is under compressive strain due to its larger lattice constant compared to GaAs. According to Bragg's law, a large lattice constant diffracts at a smaller angle leading to negative peak splitting. The spectra also shows well-defined fringes which indicates a smooth and coherent interface [1]. The Bi content was determined by fitting the HR-XRD scan using RADS mercury software, as shown in Figure 3.2. The GaBi lattice constant was assumed to be 6.324 Å [13].

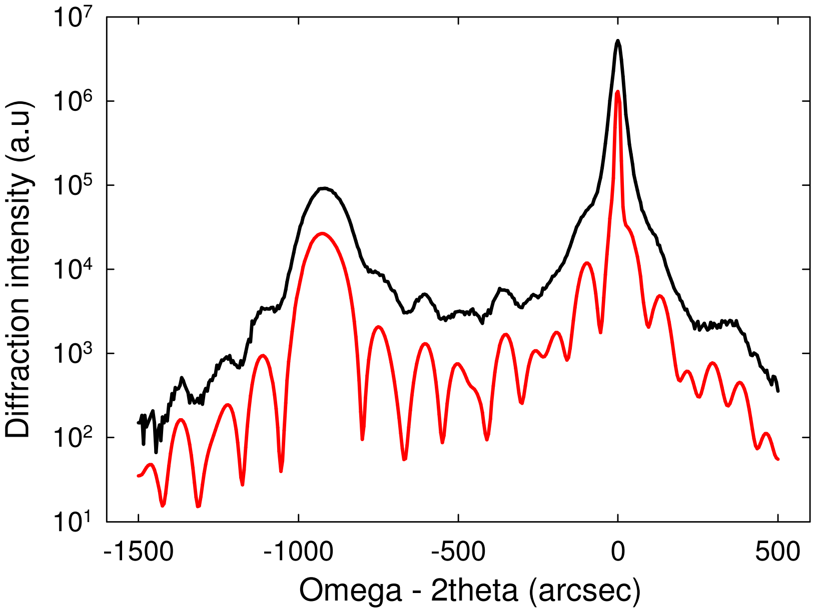

Figure 3.2 HR-XRD data (black) and RADS simulation (red) for the GaAsBi sample with a Bi content of 0.03.

3.2.2 Room temperature results

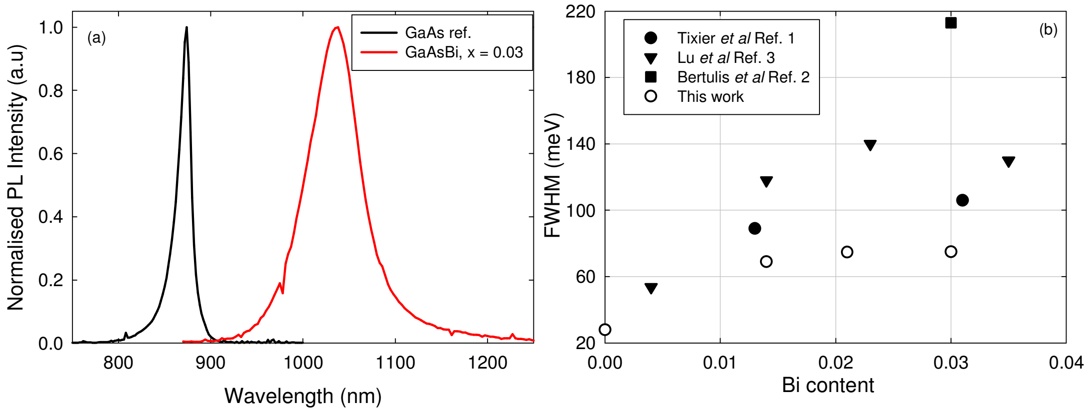

Figure 3.3 (a) Normalised RT PL spectra for the 3 μm thick GaAs reference and a GaAsBi sample with $x = 0.03$ (b) comparison of PL FWHM of this work and reports in the literature.

Figure 3.3(a) shows the normalized PL data of the GaAs reference and $GaAs_{0.97}Bi_{0.03}$ sample measured at room temperature (RT). The PL peak wavelength of the $GaAs_{0.97}Bi_{0.03}$ sample is red-shifted to 1035 nm compared to 874 nm for GaAs. However, the FWHM increases significantly with Bi incorporation. Figure 3.3 (b) shows that the introduction of a small amount of Bi in GaAs causes a sudden linewidth broadening from 28 meV for GaAs to 69 meV for $GaAs_{0.986}Bi_{0.014}$. However, the FWHM only increases slightly with further increases in Bi content for compositions up to 0.03. This suggests that the crystal quality was mainly affected by the incorporation of Bi (which induced significant alloy fluctuations) rather than the amount of Bi in the sample. Despite the large FWHM, the values reported in this work are still small compared to reports in the literature.

3.2.3 Temperature dependent results

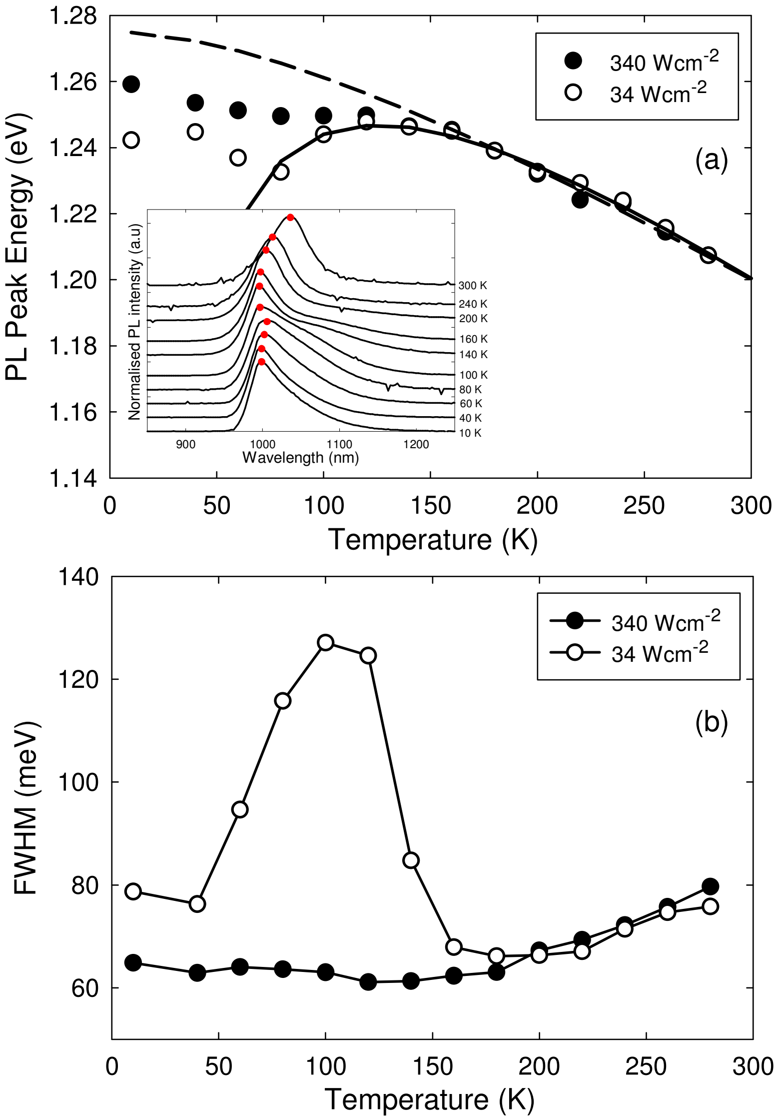

Figure 3.4 (a) Temperature dependence data (symbols) of PL peak energy with different P_e. The data are fitted using the standard and modified Varshni expression (dashed and solid lines). The inset shows the PL spectra at various temperatures for $P_e = 34$ Wcm^{-2}. These PL spectra are vertically shifted for clarity (b) FWHM versus temperature for different P_e.

PL was measured at temperatures ranging from 10 K to RT as a function of excitation power density, P_e for the GaAs$_{0.97}$Bi$_{0.03}$ sample. Temperature dependent data of the PL peak energy obtained using $P_e = 34$ and 340 Wcm^{-2} are compared in Figure 3.4 (a). Both sets of data displayed S-shape behavior, particularly at the lower pump intensity, indicating exciton localization at low temperatures. Similar observations were also reported in Ref. [4].

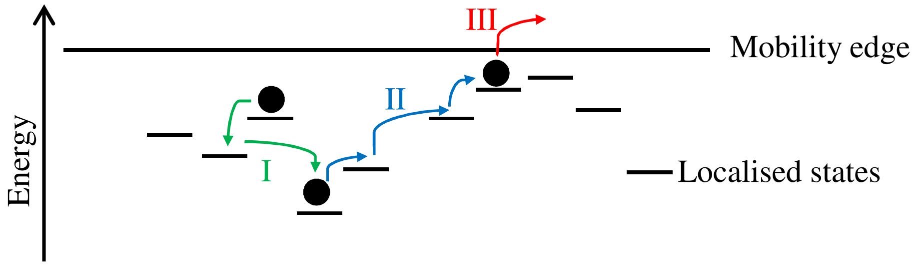

Figure 3.5 The hopping of excitons between localized states due to temperature.

The S-shape behavior consists of three main processes; (I) first red-shift from 10 to ~80 K, (II) blue-shift between 80 to ~150 K and (III) second red-shift for temperatures above 160 K. These processes are illustrated in Figure 3.5. For process (I), as temperature increases from 10 K to ~80 K, the PL peak energy decreases as excitons transfer to lower energy states nearby. For process (II), the PL peak energy increases as the increasing thermal energy increasingly mobilizes previously localized excitons. Above 160 K (process III), the excitons become delocalized and the more usual red-shift of the PL peak is observed. The second PL peak energy red-shift mainly depends on the temperature dependence of the band gap, since PL at these temperatures originates from the band edges.

The temperature dependence of the band gap in unperturbed semiconductors is often described by the Varshni equation [14],

$$E_g(T) = E_o - \frac{\alpha T^2}{T+\beta} \ , \qquad (3.1)$$

where E_o is the band gap at 0 K and α and β are fitting parameters. For perturbed semiconductors with band-tail states contributing to radiative recombination, as in the case of $GaAs_{1-x}Bi_x$, equation (3.1) is modified into [15],

$$E_{PL}(T) = E_d - \frac{\sigma^2}{kT},$$
$$= E_d(0) - \frac{\alpha T^2}{T+\beta} - \frac{\sigma^2}{kT} \qquad (3.2)$$

where E_d is the energy difference between the centre of the electron and hole density of states (assuming a Gaussian distribution). The value of E_d varies with temperature in a similar manner to E_g and hence, follows the Varshni equation, i.e $E_d = E_d(0) - \alpha T^2/(T + \beta)$ [15]. The σ^2/kT term is the Stokes-type red-shift where σ is the localization parameter which indicates the degree of localization (a large value of σ indicates strong localization effects) and k is Boltzmann's constant. The value of red-shift becomes significant at low temperatures and large values of σ. However, Equation (3.2) is only valid for T > 70 K where the assumption of non-degenerate occupation is satisfied (carrier occupation degenerates easily at low temperatures) [15].

Fitting the data in Figure 3.4 (a) using Equation (3.1) yielded $\alpha = 0.42$ meV/K and $E_o = 1.275$ eV (using $\beta = 204$ K from GaAs [16]). The localization energy for a particular temperature is defined as [17],

$$E_{loc}(T) = E_g(T) - E_{PL}(T) \qquad (3.3)$$

The maximum localization energy, E_{maxloc}, for the $GaAs_{0.97}Bi_{0.03}$ sample is 33 meV (obtained at T = 80 K). For Equation (3.2), the values obtained are, $\alpha = 0.49$ meV/K, $E_d = 1.325$ eV, $\beta = 120$ K and $\sigma = 22.5$ meV. The α values are similar, which is expected because exciton localization due to band-tail states is not pronounced at high temperatures. While these values are larger than the reported values of 0.4 and 0.27 meV/K in Ref. [18] ($x = 0.012$) and Ref. [4] ($x = 0.04 - 0.05$), respectively, they are still smaller than the temperature coefficient from a control GaAs sample which is 0.56 meV/K (not shown in Figure 3.4 (a)). Hence $GaAs_{0.97}Bi_{0.03}$ does have a weaker temperature dependence of band gap than GaAs.

FWHMs of the PL data are plotted against temperature in Figure 3.4 (b). The P_e = 34 Wcm^{-2} data exhibited a strong maximum at ~100 K, while the peak for the P_e = 340 Wcm^{-2} data was much less pronounced. This difference is expected from the more pronounced S-shape for the P_e = 34Wcm^{-2} data in Figure 3.4 (a). This is because at higher pump intensities, the higher photo-generated carrier density blurs out carrier localization effects. The abrupt increase of the FWHM with temperature is explained by the increase in exciton mobility with temperature [19]. As the temperature increases, the excitons become more mobile, thus recombining from (and producing PL with) a broader (non-equilibrium) energy distribution. The FWHM then drops when excitons come into thermal equilibrium. The subsequent FWHM increase for T > 160 K is due to increasing thermal distribution.

3.2.4 Arrhenius analysis

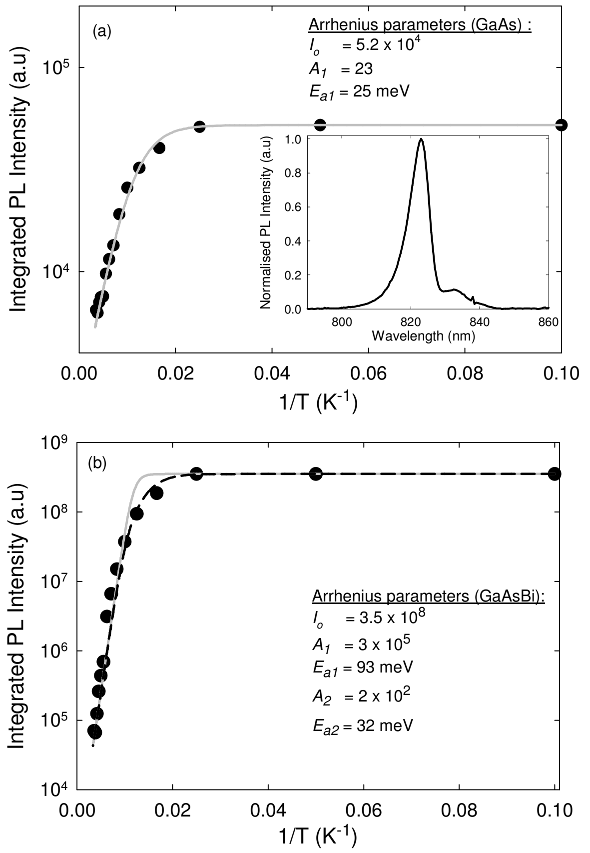

Figure 3.6 Arrhenius plot of (a) the 160 nm thick GaAs reference and (b) the GaAs$_{0.97}$Bi$_{0.03}$ sample. The inset in (a) shows the PL spectra of the GaAs reference sample measured at 10 K. The grey and black lines refer to the fittings using equations 3.4 and 3.5, respectively.

Figure 3.6 (a) shows the integrated PL (IPL) intensity for the 160 nm GaAs reference sample (grown at 400 °C) against the inverse of temperature, known as an Arrhenius plot. The PL FWHM measured at 10 K is 12 meV as shown in the inset of Figure 3.6 (a). At low temperatures (10 – 40 K) the IPL intensity is approximately unchanged. However, the IPL intensity started to decrease slowly at intermediate temperatures. At high temperatures, the IPL intensity decreases exponentially with temperature. The IPL intensity of the GaAs reference reduced by almost an order of magnitude when the temperature was changed from 10 K to room temperature. The thermal quenching of the IPL intensity can be described by,

$$I(T) = \frac{I_o}{1 + A_1 \exp\left(\frac{-E_{a1}}{kT}\right)} \quad , \tag{3.4}$$

where $I(T)$ is the IPL intensity at temperature T, I_o is the IPL intensity at 10 K, A_1 is a fitting parameter and E_{a1} is the activation energy. The best fit using Equation (3.4) yielded A_1 = 23 and E_{a1} = 25 meV as shown in Figure 3.6 (a). The E_{a1} may be attributed to the activation energy of As and Ga related defects due to the low growth temperature.

For the $GaAs_{0.97}Bi_{0.03}$ sample, the IPL intensity is significantly larger compared to the GaAs sample as shown in Figure 3.6 (b). However, the IPL intensity reduced by almost four orders of magnitude when the temperature was changed from 10 K to room temperature. Fitting using Equation (3.4) yielded $A_1 = 3 \times 10^5$ and E_{a1} = 93 meV. However, the experimental data for intermediate temperatures are not well fitted. This suggests that a second activation energy could exist for the bismide sample. Thus, Equation (3.4) can be extended to [20],

$$I(T) = \frac{I_o}{1 + A_1 \exp\left(\frac{-E_{a1}}{kT}\right) + A_2 \exp\left(\frac{-E_{a2}}{kT}\right)} \tag{3.5}$$

Fitting the data using Equation (3.5) yielded A_2 = 200 and E_{a2} = 32 meV while A_1 and E_{a1} remains the same. Equation (3.5) gives a better fit to experimental data at all temperatures.

The values of A_1 and A_2 for the GaAs$_{0.97}$Bi$_{0.03}$ sample are significantly larger than the value of A_1 for GaAs as the IPL intensity of the bismide sample reduces more rapidly with temperature. Both of the activation energies of the GaAs$_{0.97}$Bi$_{0.03}$ sample are also larger than the activation energy of the GaAs reference. The activation energy of 32 meV is bismuth-related and consistent with the 33 meV of maximum localization energy, E_{maxloc}, obtained in Figure 3.4 (a). However, the origin of the 93 meV activation energy is not clear. One possible reason is the delocalization of carriers from deep localised states. Based on the VBAC model, the valence band offset between GaAs and GaAs$_{0.97}$Bi$_{0.03}$ is 230 meV. Therefore, the escape of carriers from the valence band confinement is unlikely as it is much larger than the activation energy. Usman *et al* proposed that the incorporation of Bi in GaAs also reduces the conduction band minima linearly by 28 meV/%Bi [21]. For a sample with $x = 0.03$, the conduction band and valence band offsets with respect to GaAs band edges are 84 and 135 meV, respectively. Therefore, a more likely origin for the 93 meV activation energy is carrier escape from the conduction band confinement. The comparison between VBAC and Usman *et al* models with experimental data in this work will be discussed further in Section 3.4.

3.2.5 Power dependent results

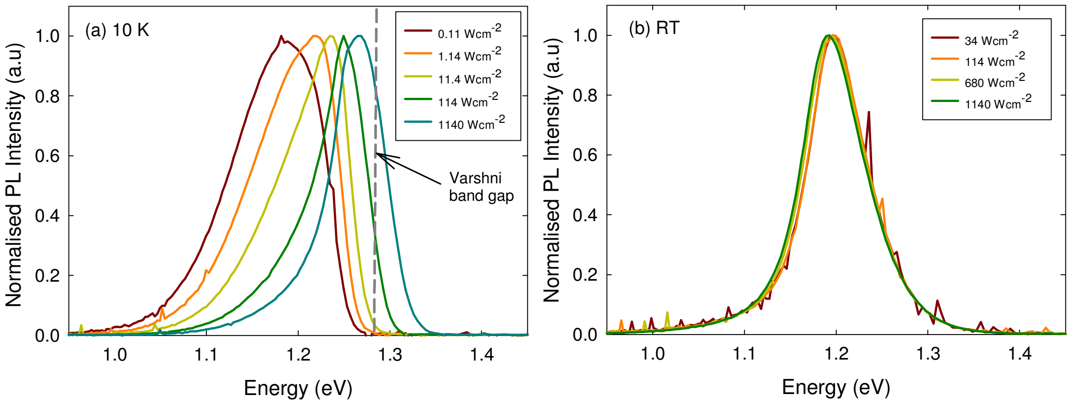

Figure 3.7 Power dependent PL of GaAs$_{0.97}$Bi$_{0.03}$ measured at (a) 10 K and (b) room temperature. The dashed line refers to the band gap estimated by the Varshni equation.

Figure 3.7 shows power dependent PL of the $GaAs_{0.97}Bi_{0.03}$ sample measured at 10 K and RT. At 10 K, the PL peak energy was blue-shifted by 77 meV when P_e was increased from 0.11 to 1140 Wcm^{-2}. The PL FWHM also reduced from 119 to 67 meV when P_e was increased by the same amount. At the highest P_e, the PL peak energy is close to 1.28 eV, the theoretical band gap estimated by the Varshni expression (Equation 3.1). This is because high excitation saturates the localized states and the PL emission will be increasingly dominated by band-to-band recombination. The saturation of localized states is also evidenced by the large blue-shift at the low energy tail compared to the high energy tail. These observations are consistent with the temperature dependent results in Section 3.2.3. However, the PL spectra becomes independent of the excitation power when measured at RT, as shown in Figure 3.7 (b). The result suggests that the carriers are delocalized at room temperature and that the PL emission can be attributed to the band gap.

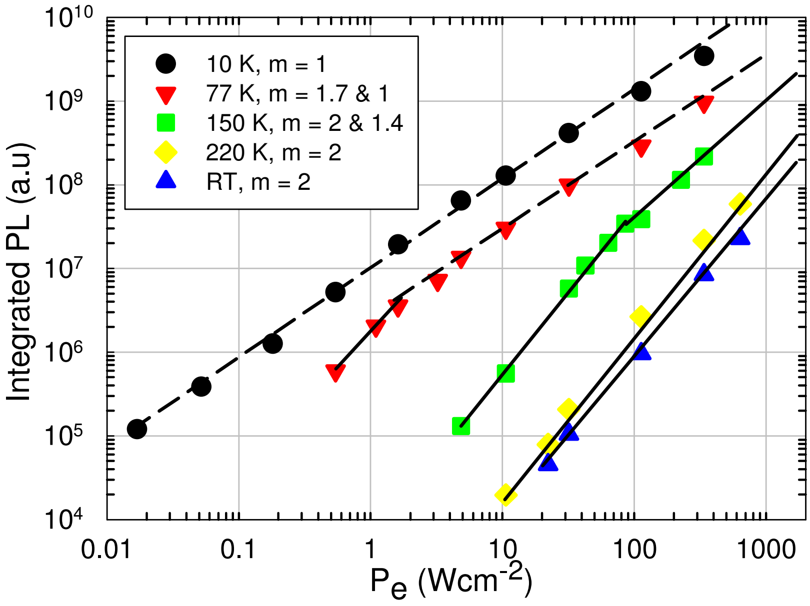

Figure 3.8 Integrated PL intensity versus excitation power density at different temperatures for $x = 0.03$. The dashed and solid lines refer to fittings with gradients of 1 and greater than 1, respectively.

The relationship between IPL intensity and excitation power density, P_e can be described by the rate equation,

$$\frac{dn}{dt} = G - \frac{n}{\tau_{nr}} - Bnp \ , \tag{3.6}$$

where G is the carrier generation rate, τ_{nr} is the non-radiative recombination lifetime, B is the radiative recombination coefficient and n and p are electron and hole concentrations, respectively. The generation of carriers is proportional to the level of excitation, $G \alpha P_e$ and at steady state, $dn/dt = 0$.

When radiative recombination is dominant, the radiative recombination term, $Bnp \gg n/\tau_{nr}$. Therefore, Equation (3.6) can be simplified to $G = Bnp$ and hence, $P_e \alpha Bnp$. In this case, Bnp changes linearly with P_e. When the non-radiative recombination is dominant, the non-radiative recombination term, $n/\tau_{nr} \gg Bnp$. Hence, Equation (3.6) can be simplified to $G = n/\tau_{nr}$ or $n = G\tau_{nr}$. However, P_e needs to be expressed in terms of Bnp as PL only measures radiative recombination. Therefore, $Bnp = B(G\tau_{nr})(G\tau_{nr})=BG^2\tau_{nr}^2$ assuming $n = p$. In this case, $Bnp \alpha P_e^2$ or IPL intensity is a square function of P_e.

Analyzing the dependence of IPL versus excitation power density can provide information about the dominant carrier recombination mechanism(s) [22]. Since dominance of non-radiative recombination is closely related to defect density in the bismide layer, such analysis will also be valuable in comparative PL studies of future bismide samples. Using data for the $GaAs_{0.97}Bi_{0.03}$ sample, IPL versus P_e data are shown as a log-log plot in Figure 3.8. The P_e was varied for almost five orders of magnitude ranging from 0.01 to 1000 Wcm^{-2}. Most of the photons were absorbed by the substrates (~ 73%) as the epilayers are relatively thin compared to the substrates. However, most of the carriers are expected to diffuse and recombine in the $GaAs_{1-x}Bi_x$ layer as the electron diffusion length is estimated to be ~ 10 μm (assuming a diffusion coefficient of 200 cm^{2}s^{-1} and carrier lifetime of 5 ns for high quality GaAs) [23]. The density of photo-generated carriers is estimated to be 4.3×10^{16} to 4.3×10^{21} cm^{-3} for $P_e = 0.01$ to 1000 Wcm^{-2}, respectively. This estimation has taken into account the 30 % of power loss due to reflections at the semiconductor/air interface. For the whole range of P_e, the concentration of the photo-generated carriers is larger than the background doping. An intrinsic $GaAs_{0.97}Bi_{0.03}$ layer is typically p-type and has background doping which varies between ~1 × 10^{14} to ~1 × 10^{16} cm^{-3} [24, 25].

Based on their gradients, *m*, the data in Figure 3.8 can be grouped into three categories, namely $m \sim 1$, $1 < m < 2$, and $m \sim 2$. They correspond to the conditions where the dominant carrier recombination mechanism is, radiative ($m \sim 1$), a mixture of radiative and monomolecular non-radiative (associated with defects) ($1 < m < 2$), or monomolecular non-radiative ($m \sim 2$) [22]. At 10 K, $m = 1$ was observed at all P_e, indicating that radiative recombination is dominant over the entire excitation range investigated. At 77 K, all P_e above $2Wcm^{-2}$ had $m = 1$, but low P_e data showed $m = 1.7$. As the temperature increases, more of the IPL dependence on P_e tended towards $m \sim 2$ for all data points. By 220 K, all the data have a gradient of 2 suggesting that with increasing temperature the more mobile carriers increasingly recombine via defect states.

3.3 Mechanism of enhanced room temperature PL

3.3.1 Description of samples

This section uses three sets of $GaAs_{1-x}Bi_x$ samples, called A, B and C which consist of 10 samples in total. The maximum Bi concentration was 0.06. The samples consist of an 80 nm GaAs buffer, a $GaAs_{1-x}Bi_x$ layer grown at a rate of 160 nm per hour and a 50 nm GaAs cap. Table 3.1 summarizes the $GaAs_{1-x}Bi_x$ samples studied in this section.

Sample set	Number of samples	GaAsBi thickness (nm)	GaAsBi growth temperature (^oC)
A	3	100	420
B	3	50	400
C	4	25	400

Table 3.1 Summary of samples studied in this section.

3.3.2 Room temperature results

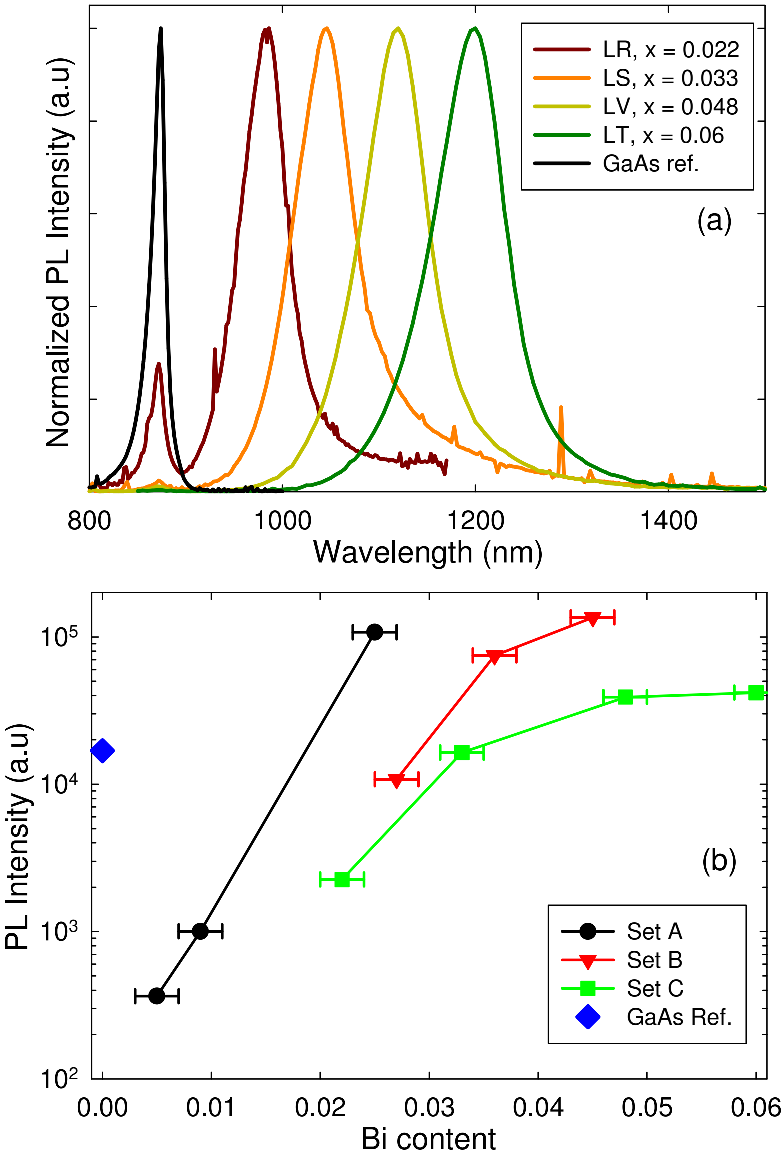

Figure 3.9 (a) Normalised room temperature PL spectra for Set C samples (b) PL intensity versus Bi content at room temperature with $P_e = 320$ Wcm^{-2}.

The normalized PL data of the Set C samples measured at RT is shown in Figure 3.9 (a). This set consists of four samples; *LR*, *LS*, *LV* and *LT* which have Bi contents of 0.022, 0.033, 0.048 and 0.06, respectively. The highest Bi content sample, *LT*, has a peak wavelength of 1.2 µm. Figure 3.9 (b) shows a PL intensity comparison as a function of Bi content with excitation power, $P_e = 320$ Wcm^{-2}. The

PL intensity of *LT* is approximately 100 times greater than the thicker $GaAs_{0.995}Bi_{0.005}$ sample in Set A. Interestingly, the PL intensity of *LT* is also twice compared to the PL intensity of a high quality 3 µm thick GaAs reference sample grown at 580 °C. Even though the GaAs sample has a different structure, the comparison still gives useful information about the crystal quality of the $GaAs_{1-x}Bi_x$ samples. The PL intensity increases rapidly at low Bi content but starts to saturate at high Bi composition. The composition dependent PL intensity enhancement may be due to (i) higher Bi content reduces the defect density, (ii) greater carrier confinement due to the larger GaAs/GaAsBi band offset for high Bi content samples or (iii) higher Bi content increases the localisation effects near the valence band maximum, efficiently trapping holes and making excitons less sensitive to non-radiative recombination centres.

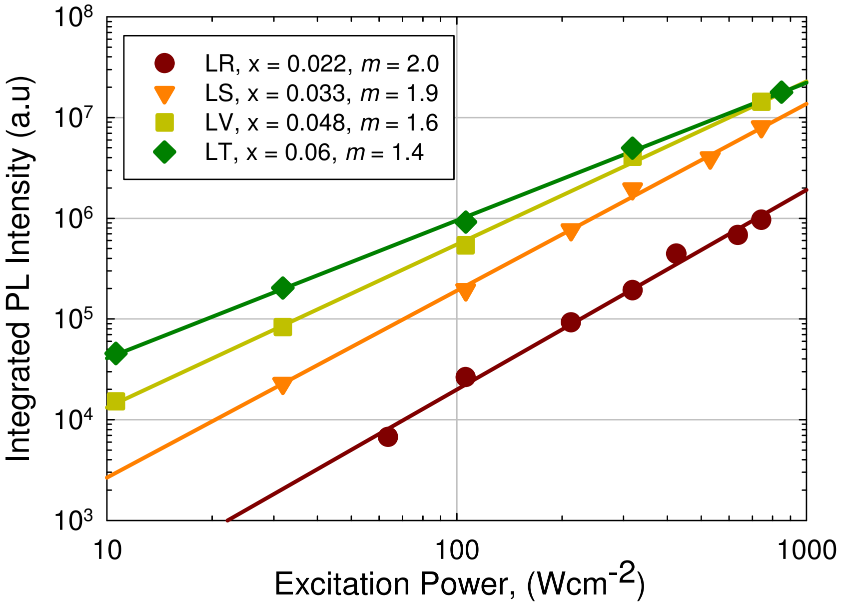

Figure 3.10 Integrated PL intensity against excitation power density measured at room temperature. The solid lines are linear fittings with slope, *m*.

In order to test hypothesis (i), excitation power dependent PL measurements were carried out for the Set C samples. Figure 3.10 shows the IPL intensity versus excitation power density data in a log-log plot. The analysis shows that the PL emissions for low Bi content samples (*LR* and *LS*) are dominated by non-radiative recombination (m = 2) but at higher Bi contents, radiative recombination becomes more significant (m = 1.6 and 1.4 for *LV* and *LT,* respectively). The PL intensity also started to saturate for high Bi fraction samples, even though m continues to decrease to 1.4.

3.3.3 Temperature dependent results

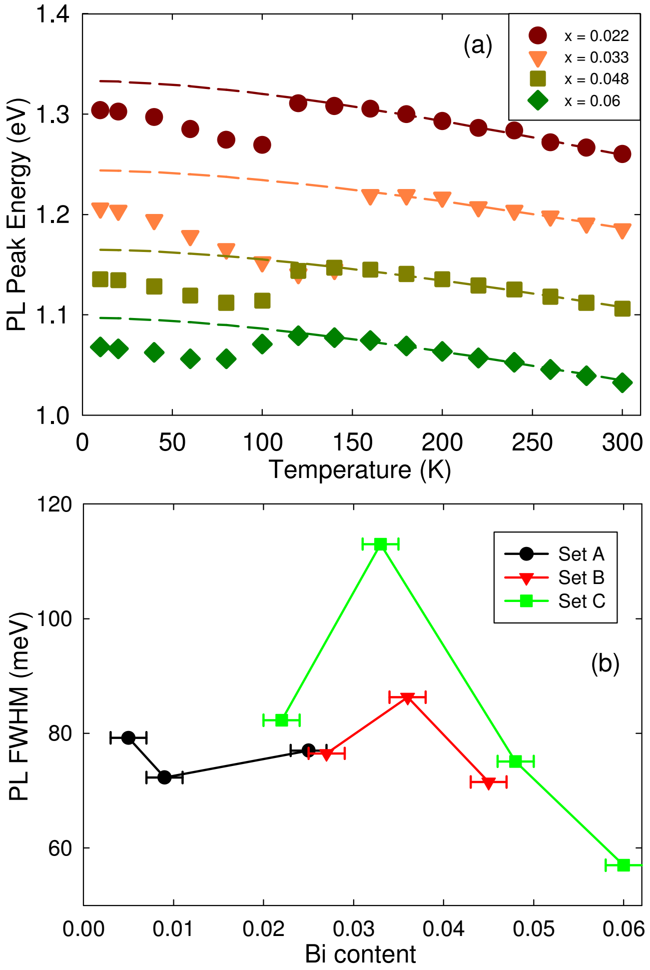

Figure 3.11 (a) Temperature dependence of PL peak energy for Set C samples and (b) FWHM measured at 10 K when excited with P_e = 53 Wcm^{-2}. The dashed lines are fittings using the Varshni equation.

Temperature dependent PL measurements were carried out to investigate the variation of localization effects in the GaAs$_{1-x}$Bi$_x$ samples. The measurements used P_e = 53 Wcm^{-2}, a power density that avoids saturating the localized states whilst ensuring measurable PL signals from all samples at room temperature. The data of PL peak energy against temperature for the Set C samples are shown in Figure 3.11

(a). All samples showed the S-shape behavior as observed earlier. However, the localization energy varies from sample to sample.

Sample	Bi content	E_{maxloc} (meV)	E_o (eV)	α (meV/K)	β (K)
LR	0.022	51	1.333	0.45	250
LS	0.033	90	1.244	0.37	280
LV	0.048	46	1.165	0.37	280
LT	0.060	36	1.097	0.39	260

Table 3.2 Varshni fitting parameters and E_{maxloc} for the Set C samples.

The data were fitted using the Varshni expression (Equation 3.1) and the fitting parameters are summarized in Table 3.2. The value of E_{maxloc} is also included in Table 3.2. As x increases from 0.022 to 0.033, E_{maxloc} initially increases from 51 to 90 meV and then decreases to 46 and 36 meV for $x = 0.048$ and 0.06, respectively. From Figure 3.11 (b), the 10 K FWHMs of the Set C samples also shows a maximum at $x = 0.033$, consistent with the trend observed for E_{maxloc}. This observation is expected as the 10 K linewidth is mainly affected by alloy fluctuations, thus indicative of the relative localization strength. However, for Set A and B samples, the linewidth is approximately constant with an average value of 77 meV. This means that the localization energy is unchanged for both sets of samples. Data in Figure 3.11 do not show an increase in localization energy and FWHM with increasing x for the range studied. Hence, localization effects are unlikely to be the main mechanism for the increased PL shown in Figure 3.9 (b).

Figure 3.12 (a) shows 10 K PL intensity plotted as a function of Bi concentration. For Set A samples, the PL intensity increases with increasing Bi content but decreases for Set B and C. The results are in contrast with the room temperature PL intensity trend observed in Figure 3.9 (b). The results suggest that the incorporation of Bi in GaAs of up to ~ 0.025 improves the material quality. It is well known that growing GaAs at significantly lower than the optimal growth temperature

(580 °C) induces many defects such as As-related defects (As-interstitial [26] and As-antisite, As_{Ga} [27]) and Ga vacancies [28]. Incorporating Bi during low temperature growth enhances surface migration, thus reducing the density of Ga and/or As-related defects [29]. Based on a deep level transient spectroscopy (DLTS) study reported recently, the trap concentration in $GaAs_{0.988}Bi_{0.012}$ is ~ 10 times lower than GaAs, when both are grown at 370 °C [29]. However, Bi incorporation also introduces Bi-related defects such as the Bi-antisite, Bi_{Ga} [30]. For $x > 0.025$, the Bi-related defects started to become significant, thus degrading the optical quality of the $GaAs_{1-x}Bi_x$. This explains the PL intensity reduction for set B and C measured at 10 K.

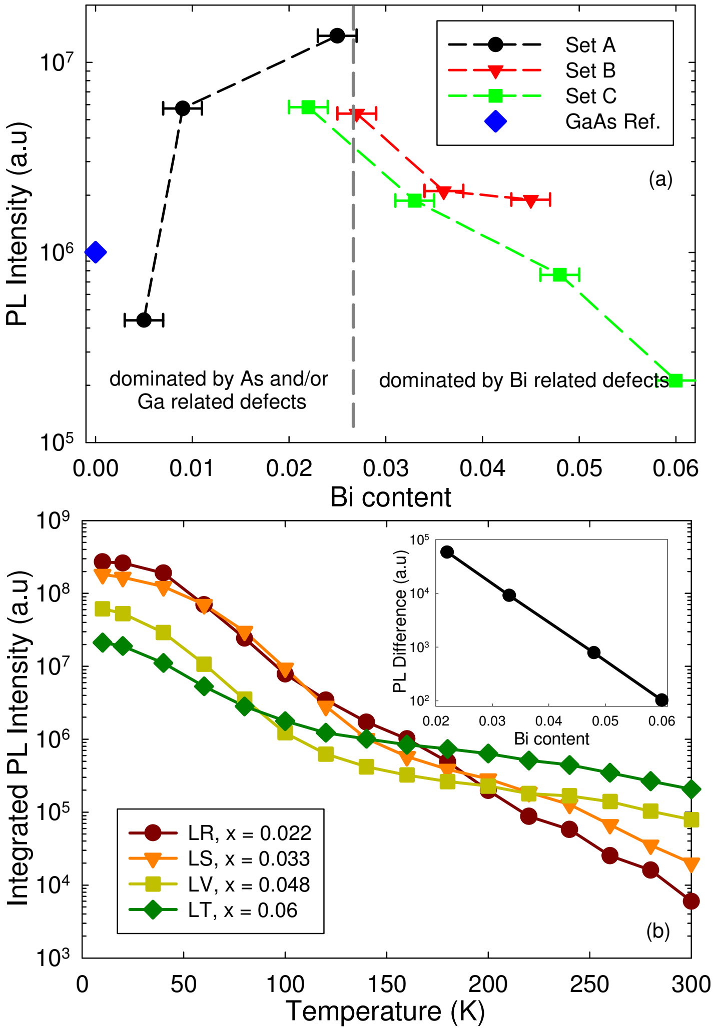

Figure 3.12 (a) PL intensity measured at 10 K and (b) temperature dependence IPL with P_e = 53 Wcm^{-2}. The inset shows the IPL difference between 10 K and RT as a function of Bi content.

Figure 3.12 (b) shows IPL intensity plotted as a function of temperature for the Set C samples. At 10 K, samples with higher Bi compositions have lower IPL intensity. However, the IPL intensity of *LR* and *LS* quenches rapidly over the whole temperature range. For *LV* and *LT*, the IPL intensity also quenches but at a smaller rate above 120 K and eventually overtakes the IPL intensity of *LR* and *LS*. The PL intensity decreases with temperature due to carrier confinement loss and the capture of carriers through defects. Between 10 and 300 K, the differences in IPL are 45000, 9000, 800 and 100 times (all arbitrary units) for *LR*, *LS*, *LV* and *LT* respectively, as shown in the inset of Figure 3.12 (b). The IPL difference reduces by approximately an order of magnitude for every 0.01 increase of Bi content.

Since the defect density increases with Bi content (for $x > 0.025$), the main reason which contributes to the lower PL quenching for high Bi content samples is lower carrier confinement loss. This means that the enhanced room temperature PL observed in Figure 3.9 (b) is the result of more efficient carrier confinement due to larger a band gap offset between $GaAs_{1-x}Bi_x$ and GaAs. The PL enhancement slowly saturates when the valence band offset becomes large enough to avoid carrier escape. This also implies that the power dependent PL measurements with m tending to 1 for increasing Bi content shown in Figure 3.10 were affected by different carrier confinement between samples.

It is expected that the room temperature PL intensity will start to decrease for $x > 0.06$ due to material quality degradation. In Ref. [3], the room temperature PL intensity increases only up to 0.045 (in this work up to 0.06), probably due to a higher density of Bi-related defects as a result of lower growth temperatures (270 – 300 ^{o}C). It is important to note that even though the crystal quality gradually degrades for $x > 0.025$, the PL intensity of $GaAs_{0.94}Bi_{0.06}$ (at RT and 10 K) is still comparable to the PL intensity of the high quality GaAs reference sample.

3.4 Band gap of GaAsBi

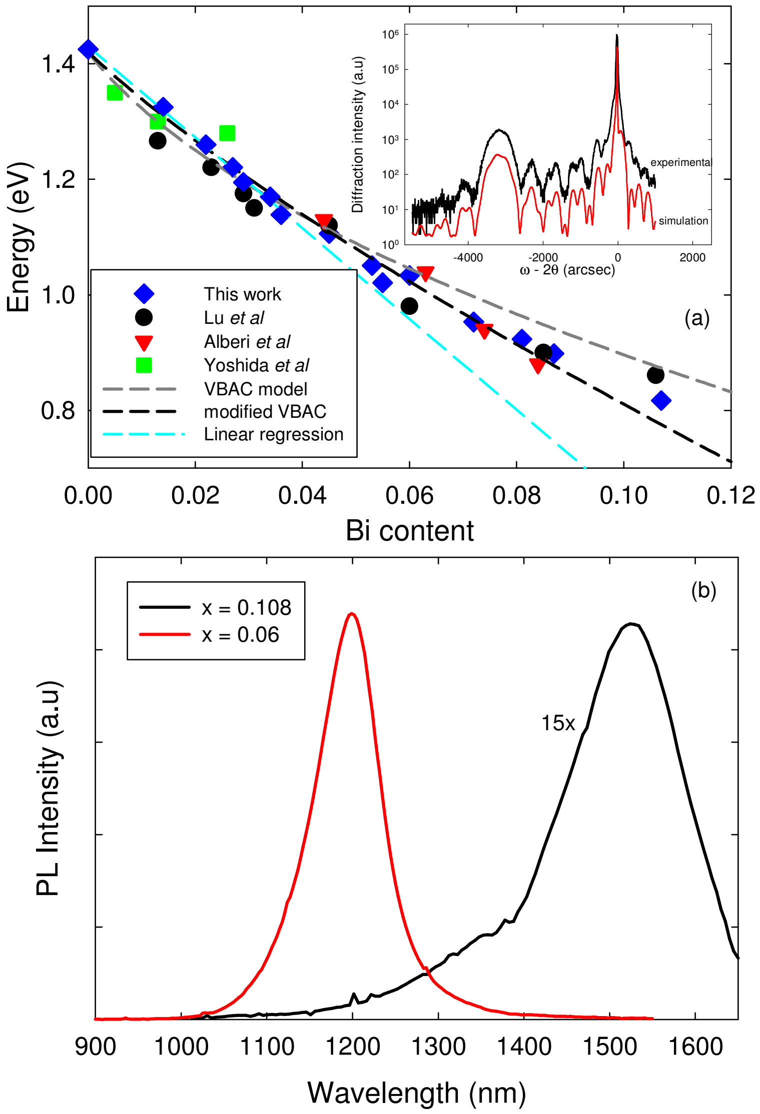

Figure 3.13 (a) Band gap of GaAsBi versus Bi concentration for samples grown by Sheffield and reports in the literature. The grey and black dashed lines refer to the band gap estimated by the VBAC and modified VBAC models, respectively. The inset shows the HR-XRD spectra of the GaAsBi sample with x = 0.108 (b) PL spectra for sample *LT* and x = 0.108 measured at room temperature.

Earlier results show that carriers are delocalised at room temperature. Therefore, the room temperature PL peak wavelength can be used to estimate the band gap of $GaAs_{1-x}Bi_x$. Figure 3.13 (a) shows band gap against Bi concentration for

x up to 0.108. The experimental data obtained from this work are consistent with data in the literature. Data from Lu *et al* [3] was obtained by photoluminescence measurements while Yoshida *et al* [31] and Alberi *et al* [32] used photo-reflectance spectroscopy. Initially, the band gap of $GaAs_{1-x}Bi_x$ reduces linearly for $x < 0.04$ at a rate of 78 meV/%Bi. For higher Bi concentration, the band gap reduction becomes less pronounced. The experimental data were then fitted using the VBAC model as described in Chapter 1. The fitting was obtained with coupling parameter, $C_{Bi} = 2.2$. However, only data for x up to 0.05 are consistent with the model. The measured band gap for $x > 0.05$ is lower than the band gap predicted by the VBAC model.

Recently, Usman *et al* reported a tight-binding analysis to investigate the electronic structure of $GaAs_{1-x}Bi_x$ [21]. This method is an atomistic approach which allows for quantitative investigation of the effect of isolated impurity atoms (in this case replacing an As atom with a Bi atom) on the electronic structure of the host material [21, 33]. Usman *et al* reported the evolution of Bi resonant states in ordered $GaAs_{1-x}Bi_x$ supercells (4096 atoms) which contained a single Bi atom, a single Bi pair and a small Bi clusters [21]. Similar calculations were then extended to calculate the electronic properties of randomly disordered $GaAs_{1-x}Bi_x$ supercells (4096 atoms) in which the number of Bi pairs and n-atom clusters increased by x^2 and x^n [21]. The results confirm that the evolution of the valence band edge of $GaAs_{1-x}Bi_x$ can be described by the VBAC model. However, the VBAC model only partially explains the band gap reduction of $GaAs_{1-x}Bi_x$.

Usman *et al* found that the conduction band minima also reduces linearly with Bi incorporation at a rate of 28 meV/%Bi [21]. The conduction band of $GaAs_{1-x}Bi_x$ ($x \leq 0.05$) retains the Γ character of the GaAs conduction band for ≥ 97 % [21]. The dominant GaAs character and linear energy reduction suggest that the evolution of the conduction band with Bi concentration can be best described by the conventional alloy model [21]. As the evolution of the valence band maxima becomes less pronounced at high Bi concentrations, the contribution from the conduction band becomes increasingly significant. For example, the conduction band offset and the valence band offset of the 0.8 eV band gap $GaAs_{1-x}Bi_x$ are 280 and 340 meV, respectively. This could explain the divergence between the experimental data and theoretical values predicted by the VBAC model at high Bi concentrations.

The VBAC model was then modified to include the reduction of the conduction band minima. The values calculated using the modified VBAC model are in agreement with the experimental data for the whole Bi concentration range, as shown in Figure 3.13 (a). The data fitting was obtained with $C_{Bi} = 1.55$. The fitting also shows that the Bi concentration needed to achieve 1.3 and 1.55 µm emission in bulk material is 0.072 and 0.102, respectively. For quantum well structures, higher Bi concentration is required to achieve similar wavelength emission due to quantum effects.

The inset in Figure 13.3 (a) shows the HR-XRD spectra of the $GaAs_{1-x}Bi_x$ sample with $x = 0.108$ (the highest Bi concentration). The HR-XRD data show well-defined fringes suggesting smooth $GaAs_{1-x}Bi_x$/GaAs interfaces and are in agreement with the simulation without relaxation. The peak splitting between $GaAs_{1-x}Bi_x$ and GaAs is -3160 arcsecs which corresponds to 1.27 % of strain. The result shows that the thickness of the $GaAs_{1-x}Bi_x$ layer (30 nm) is still below the critical thickness. For comparison, the critical thickness of an InGaAs layer with similar strain is 9 nm [34]. Even though the samples were grown under non-optimized growth conditions, reasonably good PL spectra were obtained at room temperature, as shown in Figure 3.13 (b). The $GaAs_{0.892}Bi_{0.108}$ sample has a PL FWHM of 90 meV while the PL intensity is ~15 times lower than *LT*. This result shows that both 1.3 and 1.55 µm emission can be achieved by $GaAs_{1-x}Bi_x$ on GaAs without strain compensation.

3.5 Summary

Temperature dependent and power dependent PL measurements were carried out on a series of $GaAs_{1-x}Bi_x$ samples. The temperature dependence data indicated exciton localization at low temperatures and that the band gap of the $GaAs_{0.97}Bi_{0.03}$ alloy varies more weakly with temperature than that of GaAs. At 75meV, the room temperature FWHM for this sample was significantly smaller than others reported in the literature.

Furthermore, the optical quality of $GaAs_{1-x}Bi_x$ is highly dependent on the Bi concentration. The incorporation of Bi in GaAs reduces the density of Ga and/or As-related defects as well as introducing Bi-related defects. For dilute amounts of Bi ($x < 0.025$), the crystal quality improves but a further increase of Bi causes degradation to the material quality due to a significant amount of Bi-related defects. However, the room temperature PL continues to increase up to $x = 0.06$ due to greater band-gap offset between the GaAs and $GaAs_{1-x}Bi_x$ layers. No clear correlation was found that relates the localization effect to the room temperature PL intensity enhancement.

The band gap of $GaAs_{1-x}Bi_x$ reduces rapidly with Bi composition. This can be described by modified VBAC model which considers both; the reduction of the conduction band minima and the increase of the valence band maxima with Bi incorporation. A highly-strained 30 nm thick $GaAs_{0.892}Bi_{0.108}$ sample with a room temperature PL wavelength of 1.52 μm was reported. This initial work shows the potential of $GaAs_{1-x}Bi_x$ for long wavelength optoelectronic devices on GaAs.

3.6 References

[1] S. Tixier, M. Adamcyk, T. Tiedje, S. Francoeur, A. Mascarenhas, P. Wei, and F. Schiettekatte, "Molecular beam epitaxy growth of $GaAs_{1-x}Bi_x$", *Applied Physics Letters,* vol. **82**, pp. 2245-2247, 2003.

[2] K. Bertulis, A. Krotkus, G. Aleksejenko, V. Pacebutas, R. Adomavicius, G. Molis, and S. Marcinkevicius, "GaBiAs: A material for optoelectronic terahertz devices", *Applied Physics Letters,* vol. **88**, pp. 201112-3, 2006.

[3] X. Lu, D.A. Beaton, R.B. Lewis, T. Tiedje, and Y. Zhang, "Composition dependence of photoluminescence of $GaAs_{1-x}Bi_x$ alloys", *Applied Physics Letters,* vol. **95**, pp. 041903, 2009.

[4] S. Imhof, A. Thranhardt, A. Chernikov, M. Koch, N.S. Koster, K. Kolata, S. Chatterjee, S.W. Koch, X. Lu, S.R. Johnson, D.A. Beaton, T. Tiedje, and O. Rubel, "Clustering effects in Ga(AsBi)", *Applied Physics Letters,* vol. **96**, pp. 131115-3, 2010.

[5] S. Francoeur, S. Tixier, E. Young, T. Tiedje, and A. Mascarenhas, "Bi isoelectronic impurities in GaAs", *Physical Review B,* vol. **77**,2008.

[6] G. Pettinari, A. Polimeni, M. Capizzi, J.H. Blokland, P.C.M. Christianen, J.C. Maan, E.C. Young, and T. Tiedje, "Influence of bismuth incorporation on the valence and conduction band edges of $GaAs_{1-x}Bi_x$", *Applied Physics Letters,* vol. **92**, pp. 262105, 2008.

[7] G. Pettinari, A. Polimeni, J.H. Blokland, R. Trotta, P.C.M. Christianen, M. Capizzi, J.C. Maan, X. Lu, E.C. Young, and T. Tiedje, "Compositional dependence of the exciton reduced mass in $GaAa_{1-x}Bi_x$, x= 0-10%", *Physical Review B,* vol. **81**, pp. 235211, 2010.

[8] S.F. Chichibu, A. Uedono, T. Onuma, B.A. Haskell, A. Chakraborty, T. Koyama, P.T. Fini, S. Keller, S.P. DenBaars, J.S. Speck, U.K. Mishra, S. Nakamura, S. Yamaguchi, S. Kamiyama, H. Amano, I. Akasaki, J. Han, and T. Sota, "Origin of defect-insensitive emission probability in In-containing (Al,In,Ga)N alloy semiconductors", *Nat Mater,* vol. **5**, pp. 810-816, 2006.

[9] K. Oe, "Characteristics of Semiconductor Alloy $GaAs_{1-x}Bi_x$", *Japanese Journal of Applied Physics,* vol. **41**, pp. 2801, 2002.

[10] F. Bastiman, J.C. Lin, A.G. Cullis, R. Hogg, and M. Skolnick, "Ga assisted oxide desorption on GaAs (001) studied by scanning tunnelling microscopy", *Journal of Crystal Growth,* vol. **312**, pp. 1687-1692, 2010.

[11] X. Lu, D.A. Beaton, R.B. Lewis, T. Tiedje, and M.B. Whitwick, "Effect of molecular beam epitaxy growth conditions on the Bi content of $GaAs_{1-x}Bi_x$", *Applied Physics Letters,* vol. **92**, pp. 192110, 2008.

[12] M. Henini, J. Ibanez, M. Schmidbauer, M. Shafi, S.V. Novikov, L. Turyanska, S.I. Molina, D.L. Sales, M.F. Chisholm, and J. Misiewicz, "Molecular beam epitaxy of GaBiAs on (311)B GaAs substrates", *Applied Physics Letters,* vol. **91**, pp. 251909-3, 2007.

[13] A. Janotti, S.H. Wei, and S.B. Zhang, "Theoretical study of the effects of isovalent coalloying of Bi and N in GaAs", *Physical Review B* vol. **65**, pp. 1152031-1152035, 2002.

[14] Y.P. Varshni, "Temperature dependence of the energy gap in semiconductors", *Physica (Amsterdam),* vol. **34**, pp. 149, 1967.

[15] P.G. Eliseev, P. Perlin, J. Lee, and M. Osinski, "Blue temperature-induced shift and band-tail emission in InGaN-based light sources", *Applied Physics Letters,* vol. **71**, pp. 569-571, 1997.

[16] I. Vurgaftman, J.R. Meyer, and L.R. Ram-Mohan, "Band parameters for III-V compound semiconductors and their alloys", *Journal of Applied Physics,* vol. **89**, pp. 5815-5875, 2001.

[17] M.A. Pinault and E. Tournie, "On the origin of carrier localization in $Ga_{1-x}In_xN_yAs_{1-y}$/GaAs quantum wells", *Applied Physics Letters,* vol. **78**, pp. 1562-1564, 2001.

[18] S. Francoeur, M.J. Seong, A. Mascarenhas, S. Tixier, M. Adamcyk, and T. Tiedje, "Band gap of $GaAs_{1-x}Bi_x$, 0<x<3.6%", *Applied Physics Letters,* vol. **82**, pp. 3874-3876, 2003.

[19] H. Gruning, K. Kohary, S.D. Baranovskii, O. Rubel, P.J. Klar, A. Ramakrishnan, G. Ebbinghaus, P. Thomas, W. Heimbrodt, W. Stolz, and W.W. Ruhle. "Hopping relaxation of excitons in GaInNAs/GaNAs quantum wells". in *Physica Status Solidi C*, 2004

[20] N. Grandjean, J. Massies, I. Grzegory, and S. Porowski, "GaN/AlGaN quantum wells for UV emission: heteroepitaxy versus homoepitaxy", *Semiconductor Science and Technology,* vol. **16**, pp. 358, 2001.

[21] M. Usman, C.A. Broderick, A. Lindsay, and E.P. O'Reilly, "Tight-binding analysis of the electronic structure of dilute bismide alloys of GaP and GaAs", *Physical Review B,* vol. **84**, pp. 245202, 2011.

[22] N.F. Hasbullah, J.S. Ng, H.Y. Liu, M. Hopkinson, J.P.R. David, T.J. Badcock, and D.J. Mowbray, "Dependence of the electroluminescence on the spacer layer growth temperature of multilayer quantum-dot laser structures", *IEEE Journal of Quantum Electronics,* vol. **45**, pp. 79-85, 2009.

[23] *Electronic Achive: New Semiconductor Materials, Characteristics and Properties* 1998, Ioffe Physico-Technical Institute: http://www.ioffe.ru/SVA/NSM/Semicond/GaAs/electric.html.

[24] G. Pettinari, A. Patane, A. Polimeni, M. Capizzi, X. Lu, and T. Tiedje, "Bi-induced p-type conductivity in nominally undoped Ga(AsBi)", *Applied Physics Letters,* vol. **100**, pp. 092109-4, 2012.

[25] C.J. Hunter and F. Bastiman, *Electrical characterisation of GaAsBi pin diodes, Unpublished results*, 2012.

[26] N. Hozhabri, S.H. Lee, and K. Alavi, "Infrared measurements in annealed molecular beam epitaxy GaAs grown at low temperature", *Applied Physics Letters,* vol. **66**, pp. 2546-2548, 1995.

[27] M. Kaminska, Z. Liliental-Weber, E.R. Weber, T. George, J.B. Kortright, F.W. Smith, B.Y. Tsaur, and A.R. Calawa, "Structural properties of As-rich GaAs grown by molecular beam epitaxy at low temperatures", *Applied Physics Letters,* vol. **54**, pp. 1881-1883, 1989.

[28] J. Gebauer, R. Krause-Rehberg, S. Eichler, M. Luysberg, H. Sohn, and E.R. Weber, "Ga vacancies in low-temperature-grown GaAs identified by slow positrons", *Applied Physics Letters,* vol. **71**, pp. 638-640, 1997.

[29] T. Fuyuki, S. Kashiyama, Y. Tominaga, K. Oe, and M. Yoshimoto, *Deep level transient spectroscopy sutdy on p-type GaAsBi mixed crystals*, in *38th International Symposium on Compound Semiconductors, Berlin,* 2011.

[30] M. Kunzer, W. Jost, U. Kaufmann, H.M. Hobgood, and R.N. Thomas, "Identification of the BiGa heteroantisite defect in GaAs:Bi", *Physical Review B,* vol. **48**, pp. 4437, 1993.

[31] K.T.W.O. Yoshida J and K. Oe, "Temperature Dependence of GaAsBi Band Gap Studied by Photoreflectance Spectroscopy", *Japanese Journal of Applied Physics,* vol. **42**, pp. 371, 2003.

[32] K. Alberi, O.D. Dubon, W. Walukiewicz, K.M. Yu, K. Bertulis, and A. Krotkus, "Valence band anticrossing in $GaBi_xAs_{1-x}$", *Applied Physics Letters,* vol. **91**, pp. 051909-3, 2007.

[33] E.P.O. Reilly, A. Lindsay, S. Tomić, and M. Kamal-Saadi, "Tight-binding and k·p models for the electronic structure of Ga(In)NAs and related alloys", *Semiconductor Science and Technology,* vol. **17**, pp. 870, 2002.

[34] E.A. Fitzgerald, *Properties of lattice-matched and strained InGaAs*, editted by. P. Bhattacharya. Vol. 8. 1992 IEE EMIS Datareviews series.

Chapter 4

Effects of Rapid Thermal Annealing on GaAsBi Alloys

4.1. Motivation

Since $GaAs_{1-x}Bi_x$ samples are grown at relatively low temperatures, wafer quality might be expected to improve with thermal annealing as in the case for GaNAs samples [1]. However, Feng *et al* reported that annealing $GaAs_{1-x}Bi_x$ (x = 0.032) grown by MBE at up to 800 ^{o}C did not improve its room temperature PL [2]. The PL peak wavelength also blue-shifted by 8 meV which was attributed to micro-scale changes inside the epilayer rather than Bi out diffusion [2]. However, for MOVPE grown $GaAs_{1-x}Bi_x$, PL intensity improvements of more than 10 times and FWHM reductions of 23 meV were observed at 10 K [3]. Despite the significant improvements in Ref. [3], no PL emission could be detected above 100 K. Recently, a photo-reflectance measurement performed by Chine *et al* shows that the band gap of $GaAs_{1-x}Bi_x$ was red-shifted by 60 meV after annealing at 600 ^{o}C [4].

The mixed results in the literature show that the effects of annealing on $GaAs_{1-x}Bi_x$ alloys are not well understood. In this chapter, a systematic study on the effects of annealing on the optical and structural properties of MBE grown $GaAs_{1-x}Bi_x$ alloys will be discussed. The origin of the optical quality improvement also will be addressed.

4.2. Description of samples

The $GaAs_{1-x}Bi_x$ samples were grown on pieces cleaved from semi-insulating GaAs (100) substrates. Each sample consists of a GaAs buffer, 10 - 50 nm $GaAs_{1-x}Bi_x$ epilayer and a GaAs cap. This study uses samples with Bi contents between 0.022 and 0.065. The summary of samples used in this chapter is shown in Table 4.1. All samples were grown at 400 ^{o}C (including the GaAs reference) except for the samples with x = 0.04, 0.042 and 0.065 which were grown at 420, 370 and 380 ^{o}C, respectively. The sample size is either 11.0 × 3.5 mm^2 or 11.4 × 11.8 mm^2 depending on the substrate holder used during growth. Each sample was then cleaved into pieces with an average size of 5.6 × 4.7 mm^2, large enough to avoid edge effects in subsequent PL measurements. Post-growth annealing was carried out in a rapid thermal annealing (RTA) system in nitrogen ambient. For Section 4.3 and 4.5, samples were annealed at 600, 700 and 800 ^{o}C for 30 seconds. For Section 4.4, the annealing temperature was fixed while the annealing time was varied for 3, 30 and 60 seconds.

Section	Sample name	Bi content
4.3	GaAs ref.	-
	LR	0.022
	LS	0.033
	STB0DT	0.040
	LV	0.048
	LT	0.060
	STB02G	0.065
4.4	*STB0GW*	0.042
	STC01B	0.058
4.5	*STB02C*	0.037
	STB02H	0.050

Table 4.1 Summary of samples used in this chapter

4.3. Varying annealing temperatures

4.3.1. AFM results

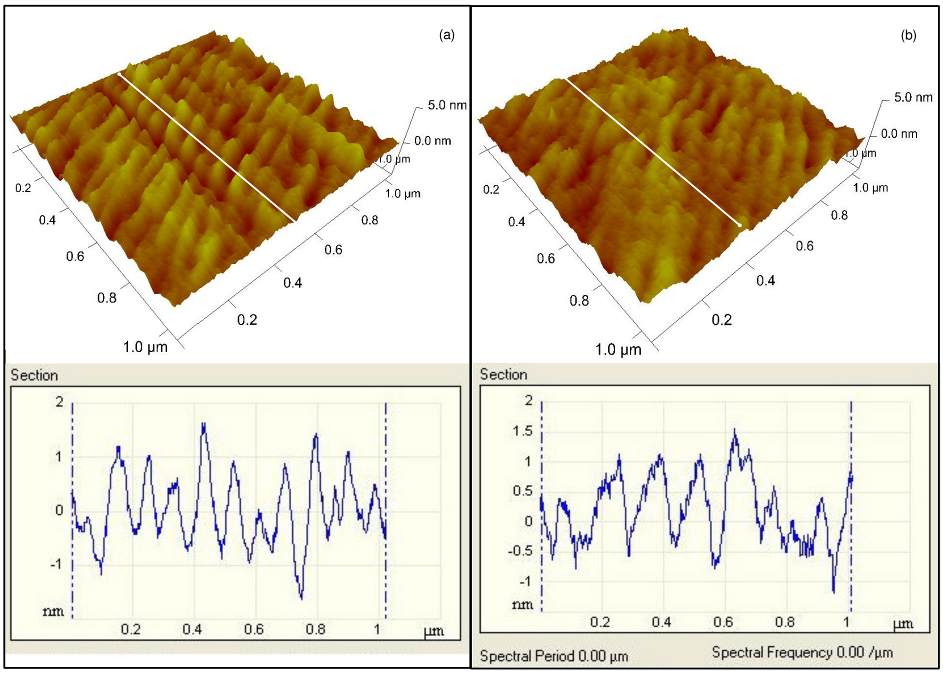

Figure 4.1 AFM 3D plots and cross-sectional scans of sample *LR* before (a) and after (b) annealing. The sample was annealed at 700 °C for 30 seconds in a nitrogen ambient.

Figure 4.1 shows the Atomic Force Microscopy (AFM) 3D plots and cross-sectional scans of as-grown and annealed $GaAs_{1-x}Bi_x$ pieces with $x = 0.022$ (sample *LR*). The as-grown sample has rms roughness of 0.64 nm which is approximately twice the rms roughness of typical high quality GaAs [5]. This is mainly due to the presence of undulations on the surface which are elongated along the $[\bar{1}\ 1\ 0]$. Similar AFM surface topography was also reported by Lu *et al* [6]. Based on high-resolution Scanning Tunnelling Microscopy (STM) images taken by F. Bastiman on uncapped $GaAs_{0.967}Bi_{0.033}$, it was found that the undulations are not a 3D feature but rather densely ordered monolayer islands which were formed during the $GaAs_{1-x}Bi_x$ layer growth [7]. The average period and peak-to-peak amplitude of the undulations are 93 nm and 1.6 nm, respectively. After annealing at 700 °C for 30 seconds, the rms roughness reduces to 0.55 nm. The surface undulations also become broader with an average period of 136 nm.

4.3.2. Photoluminescence and HR-XRD results

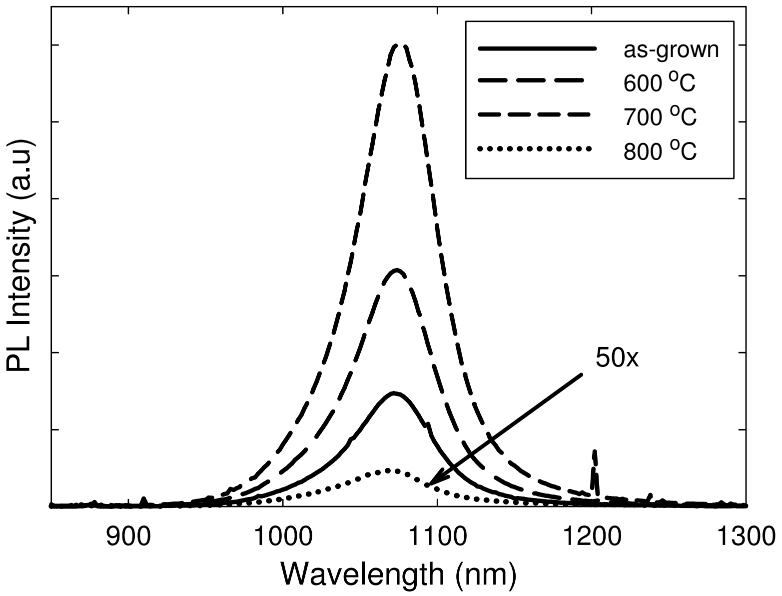

Figure 4.2 PL data of as-grown and annealed GaAsBi with Bi content of 0.04 measured at room temperature.

Figure 4.2 shows the room temperature PL data of as-grown and annealed $GaAs_{1-x}Bi_x$ with $x = 0.04$ (*STB0DT*). For annealing temperatures of 600 and 700 °C, the PL intensity increases (compared to the as-grown) while the PL peak wavelength remained relatively unchanged. This result is encouraging as optical quality improvement could be obtained without compromising the PL peak wavelength. However, the optical quality degraded significantly and the PL peak wavelength blue-shifted by 4 meV when annealed at 800 °C. Hence, 700 °C is the optimum annealing temperature with ~ 3 times of PL intensity improvement.

The PL improvement factor is relatively small compared to the effect of annealing on other semiconductor alloys (i.e GaAs and GaNAs). The integrated PL intensity of the GaAs reference sample (grown at 400 °C) increases by ~ 6 times when annealed at 700 °C. This shows that the arsenic and gallium related defects generated by low growth temperature are easily removed by thermal annealing. In the case of GaNAs, annealing typically leads to significant PL improvement (~ 10 times) but at the expense of PL peak wavelength blue-shift. The significant PL improvement is mainly attributed to the removal of the high density of nitrogen interstitials [1].

The optimum annealing temperature (700 ^{o}C) shown in Figure 4.2 was then used to anneal other $GaAs_{1-x}Bi_x$ samples. Room temperature PL measurements of the as-grown and annealed samples were then carried out. For a given Bi content, the integrated PL improvement ratio between the annealed and as-grown samples was obtained. The PL improvement ratio versus Bi content is shown in Figure 4.3 (a). For samples with $x < 0.048$, PL improvement of ~ 3 times was observed. However, the level of PL improvement reduced for higher Bi content samples and in fact, degraded the luminescence of the sample with $x = 0.065$.

In order to investigate the diminishing improvement in PL intensity for high Bi content samples in Figure 4.3 (a), pieces from the $GaAs_{1-x}Bi_x$ sample with $x = 0.065$ were annealed at different temperatures and the integrated PL improvement ratios are shown in Figure 4.3 (b). It is found that the optimum annealing temperature for $GaAs_{0.935}Bi_{0.065}$ sample is 600 ^{o}C, (100 ^{o}C lower than that of the $GaAs_{0.96}Bi_{0.04}$ sample), suggesting that the optimum annealing temperature is dependent on Bi composition. Hence, using a fixed annealing temperature of 700 ^{o}C for all samples ($x = 0.022$ to 0.065) will give rise to different PL improvement ratios, resulting in the trend in Figure 4.3 (a). Composition dependence of optimum annealing temperatures has been observed in other material systems. It was reported that the optimum annealing temperature of GaNAs reduces from 1000 to 700 ^{o}C when the N content increases from 0.06 to 6 % [8, 9].

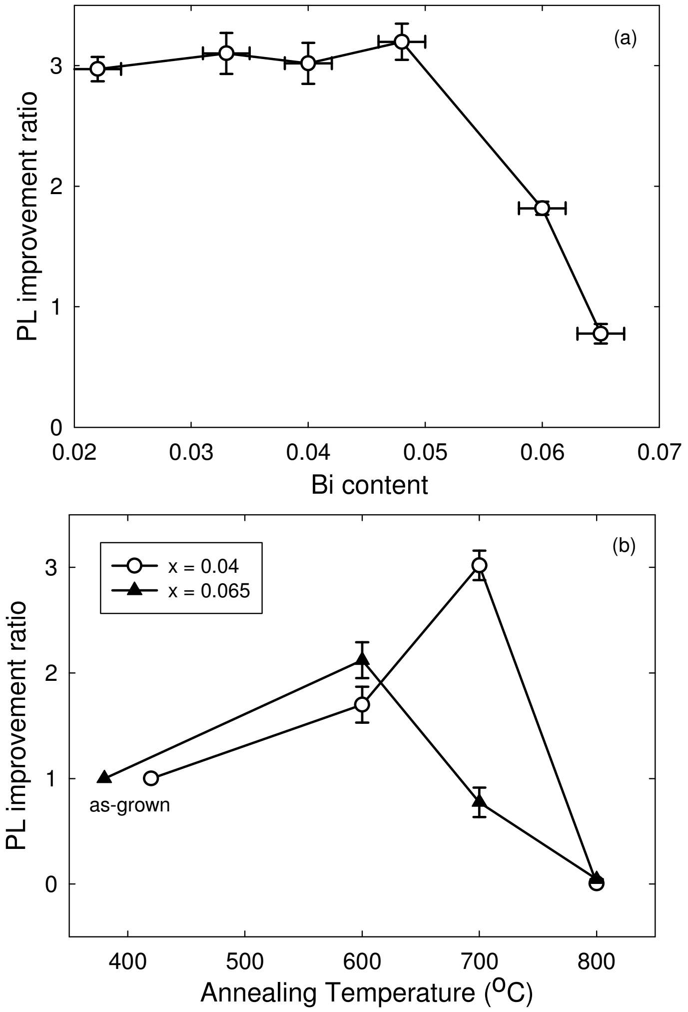

Figure 4.3 (a) The PL improvement ratios of annealed samples with different Bi contents. The samples were annealed at 700 °C for 30 seconds, (b) PL improvement ratios against annealing temperatures for GaAsBi pieces with $x = 0.04$ and 0.065.

The HR-XRD data for the $GaAs_{0.935}Bi_{0.065}$ sample are compared in Figure 4.4 (a). Annealing at 600 °C causes no noticeable structural change compared to the as-grown piece and the average Bi content remained the same. However, the peak-to-valley contrast of the Pendellösung fringes degrades for the 700 °C piece, suggesting a poorer $GaAs_{1-x}Bi_x$/GaAs interface. This may explain the lower PL intensity in Figure 4.3 (b). For the 800 °C piece, only a weak shoulder is observed with no well-defined $GaAs_{1-x}Bi_x$/GaAs interface. As expected, the PL peak energy measured at 10 K shows a blue-shift of 120 meV (Figure 4.4 (b)), consistent with significant Bi out-diffusion as observed in the HR-XRD spectra.

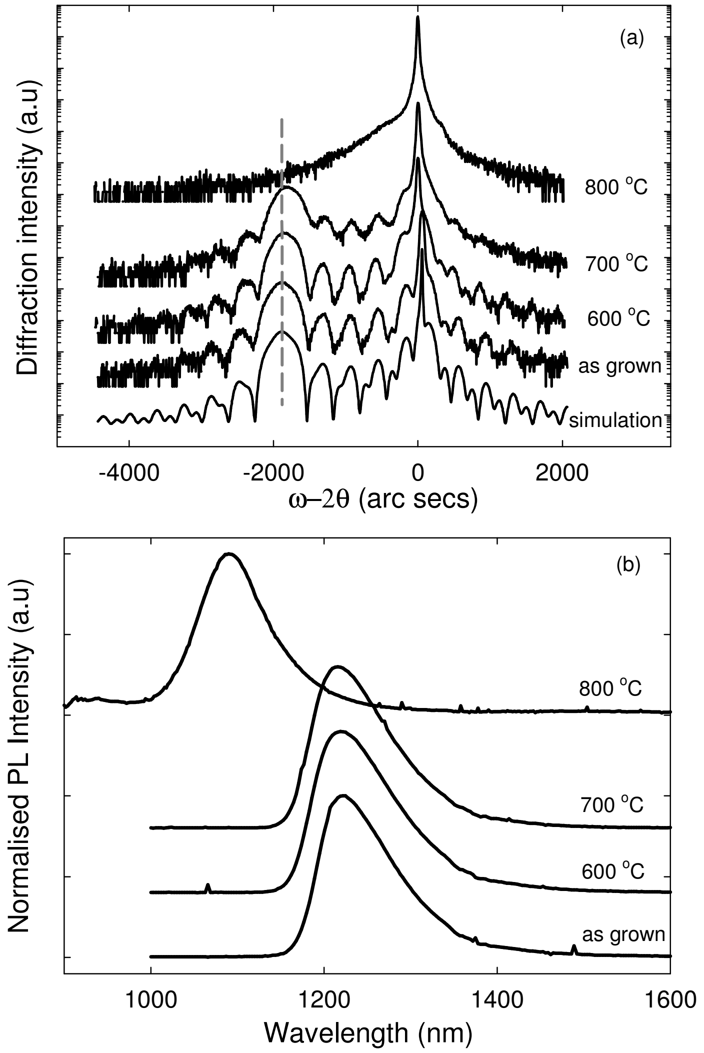

Figure 4.4 (a) The HR-XRD curves of the GaAsBi sample (x = 0.065) at different annealing temperatures. (b) The normalized PL spectra for pieces in (a) measured at 10 K. The spectra were vertically shifted for clarity.

Localization effects in $GaAs_{1-x}Bi_x$ alloys have been shown earlier using temperature dependent PL studies. The temperature dependent PL of as-grown and annealed $GaAs_{1-x}Bi_x$ pieces was measured to assess the effects of annealing on localization and the results are shown in Figure 4.5 (a). For the sample with x = 0.048, the annealed piece shows a less pronounced S-shape behavior compared to the as-grown piece. The 10 K PL peak energy blue-shifts by 6 meV and the PL FWHM reduces from 75 to 68 meV. For the $GaAs_{0.96}Bi_{0.04}$ pieces, the temperature dependent PL data are similar for the as-grown and the annealed pieces, with only a 4 meV reduction in FWHM of the 10 K PL. For temperatures above 150 K, the PL peak energies of the as-grown and annealed pieces for both compositions (x = 0.04 and 0.048) are similar, showing that the band gap is not affected by annealing.

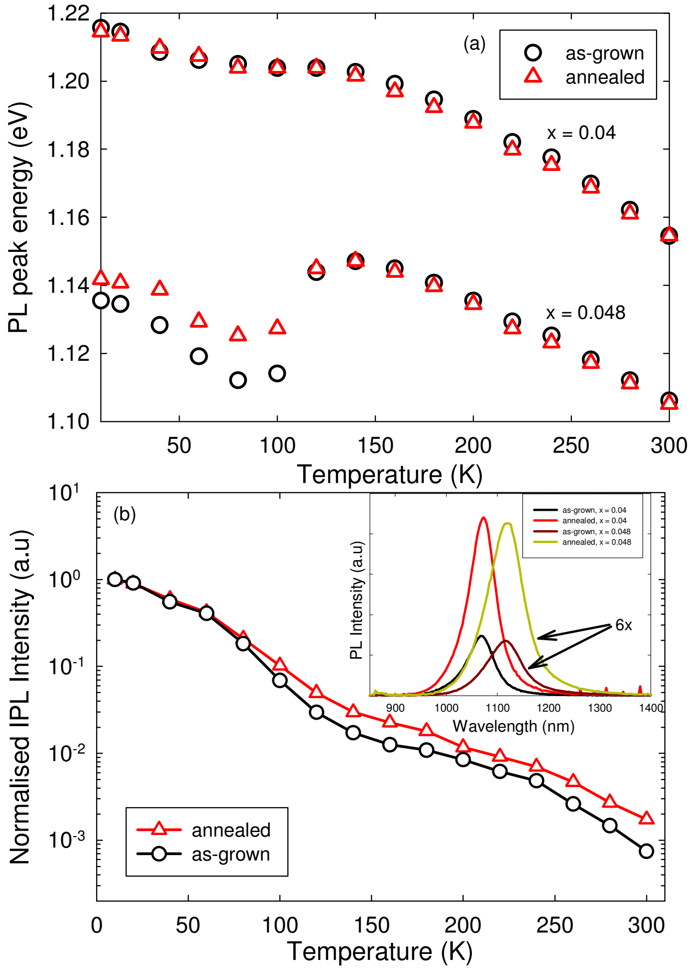

Figure 4.5 (a) Temperature dependence of PL peak energy of as-grown and annealed (700 °C for 30 seconds) GaAsBi samples with Bi contents 0.04 and 0.048. (b) Normalized IPL intensity versus temperature for x = 0.04. The inset shows the room temperature PL spectra before and after annealing for both compositions.

The growth conditions of the $GaAs_{0.96}Bi_{0.04}$ sample were altered compared to $GaAs_{0.952}Bi_{0.048}$ sample in order to reduce the localization effects and significantly weaker localization was obtained, as shown in Figure 4.5 (a). The $GaAs_{0.96}Bi_{0.04}$ sample was grown at 420 °C at a rate of 1 µm per hour while the $GaAs_{0.952}Bi_{0.048}$ sample was grown at 400 °C at a rate of 0.16 µm per hour. The room temperature PL intensity of the $GaAs_{0.96}Bi_{0.04}$ sample is ~ 6 times higher than the $GaAs_{0.952}Bi_{0.048}$ sample, as shown in the inset of Figure 4.5 (b). Figure 4.5 (b) shows that the IPL intensity of the annealed piece reduces at a slower rate with temperature compared to the as-grown piece for temperatures above 100 K. This indicates that the density of defects in the sample reduces with thermal annealing.

Since similar room temperature PL improvement ratio was achieved (~3 times) in samples with x = 0.04 and 0.048 through thermal annealing, whilst reductions in localization effects in both differs, we may conclude that the PL improvement obtained does not necessarily originate from the reduction of Bi inhomogeneity. The small reduction of the 10 K PL FWHM for both samples indicates that alloy fluctuations in $GaAs_{1-x}Bi_x$ are not easily removed by thermal annealing. Hence, the PL intensity improvement could be dominated by the reduction of other types of defects including arsenic and gallium related defects.

4.4. Varying annealing duration

Further optimization was carried out by varying the annealing time at a fixed annealing temperature. This section uses two additional $GaAs_{1-x}Bi_x$ samples with x = 0.042 and 0.058. The optimum annealing temperatures shown in Figure 4.3 were used; 700 ^{o}C for $GaAs_{0.958}Bi_{0.042}$ and 600 ^{o}C for $GaAs_{0.942}Bi_{0.058}$. PL measurements which were carried out before the annealing process show that the wavelength varies with position for this set of samples. The wavelength varies between 1102 – 1108 nm and 1206 – 1214 nm for $GaAs_{0.958}Bi_{0.042}$ and $GaAs_{0.942}Bi_{0.058}$, respectively.

Figure 4.6 (a) shows that for the $GaAs_{0.958}Bi_{0.042}$ sample, the PL intensity of the annealed pieces increases by 2.6 to 3 times compared to the as-grown piece. The PL improvement ratio is almost independent of the annealing time. For the $GaAs_{0.942}Bi_{0.058}$ sample, the PL intensity of the annealed pieces increases with annealing time by factors of 1.1, 2 and 2.4 for annealing times of 3, 30 and 60 seconds, respectively. It is expected that the PL improvement ratio will increase to ~ 3 with longer annealing time.

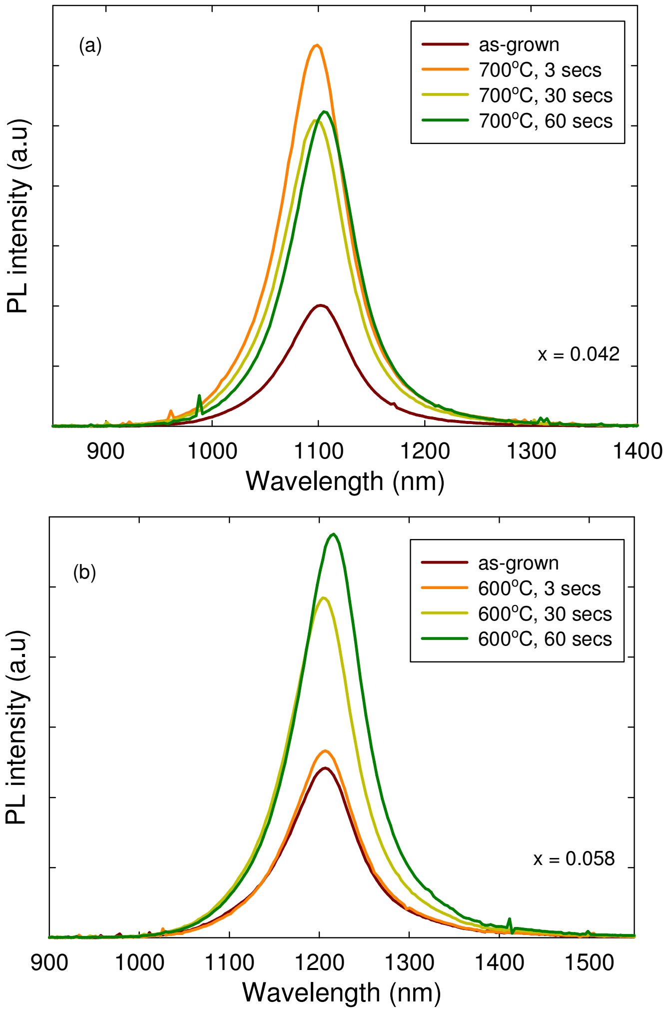

Figure 4.6 The room temperature PL spectra of as-grown and annealed GaAsBi with Bi contents of (a) 0.042 and (b) 0.058.

4.5. Effects of thermal annealing on rough samples

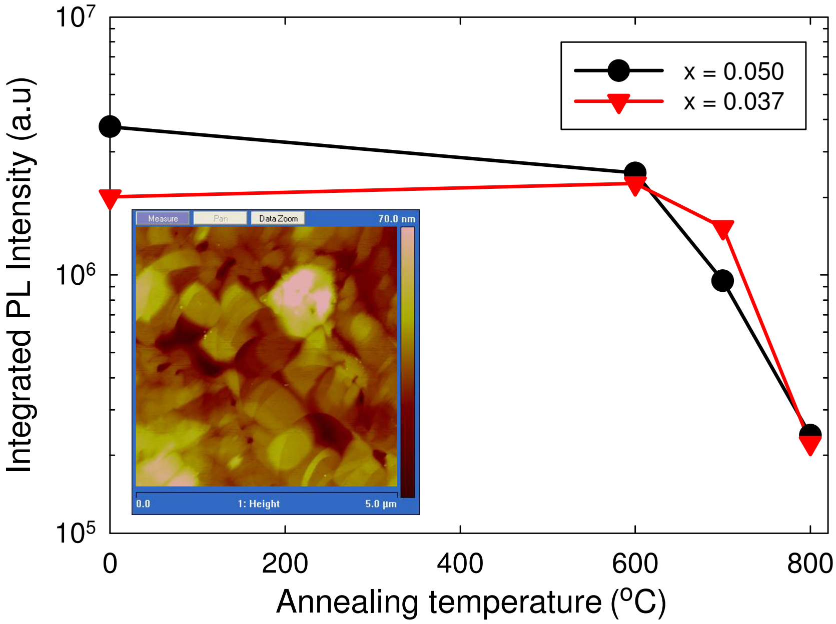

Figure 4.7 Integrated PL intensity versus annealing temperatures for GaAsBi samples with rough surfaces. The inset shows the 5 × 5 μm AFM image of the sample with $x = 0.037$.

In this section, the effect of annealing on $GaAs_{1-x}Bi_x$ samples with rough surfaces is presented. The rms roughness of these samples is ~10 nm as generated by 5 x 5 μm AFM scans. The typical rms roughness for a mirror-like sample is between 0.5 and 0.75 nm. Figure 4.7 shows the IPL intensity against annealing temperature for two $GaAs_{1-x}Bi_x$ samples, whose Bi contents are 0.037 and 0.05. Even though the samples' surfaces are not mirror-like, their room temperature PL intensities are still within an order of magnitude of those of the mirror-like samples. However, the PL FWHMs are much larger, at ~ 115 meV. Interestingly, annealing these samples causes no PL improvement or PL degradation, suggesting that the effects of annealing for $GaAs_{1-x}Bi_x$ are also dependent on the sample surface roughness.

4.6. Summary

The effects of rapid thermal annealing on the optical and structural properties of $GaAs_{1-x}Bi_x$ alloys for x ranging from 0.022 to 0.065 were investigated. At room temperature, the annealed $GaAs_{1-x}Bi_x$ showed a modest improvement (~ 3 times) in photoluminescence while the PL peak wavelength remained relatively unchanged. It was found that bismuth related defects are not easily removed by annealing and the PL improvement may be dominated by the reduction of other types of defects including arsenic and gallium related defects. Also, the optimum annealing temperature is Bi composition dependent. For samples with $x < 0.048$, the optimum annealing temperature is 700 ^{o}C but reduces to 600 ^{o}C for higher compositions.

4.7. References

[1] S. Spruytte, C. Coldren, J. Harris, W. Wampler, P. Krispin, K. Ploog, and M. Larson, "Incorporation of nitrogen in nitride-arsenides: Origin of improved luminescence efficiency after anneal", *Journal of Applied Physics,* vol. **89**, pp. 4401, 2001.

[2] G. Feng, K. Oe, and M. Yoshimoto, "Influence of Thermal Annealing Treatment on the Luminescence Properties of Dilute GaNAs-Bismide Alloy", *Japanese Journal of Applied Physics,* vol. **46**, pp. L764-66, 2007.

[3] I. Moussa, H. Fitouri, Z. Chine, A. Rebey, and B.E. Jani, "Effect of thermal annealing on structural and optical properties of the $GaAs_{0.963}Bi_{0.037}$ alloy", *Semiconductor Science and Technology,* vol. **23**, pp. 125034, 2008.

[4] Z. Chine, H. Fitouri, I. Zaied, A. Rebey, and B.E. Jani, "Photoreflectance and photoluminescence study of annealing effects on GaAsBi layers grown by metalorganic vapor phase epitaxy", *Semiconductor Science and Technology,* vol. **25**, pp. 065009, 2010.

[5] S. Ikuo, U. Katsuhiro, and S. Tae-Yeon, "Growth and structural characterization of III–N–V semiconductor alloys", *Semiconductor Science and Technology,* vol. **17**, pp. 755, 2002.

[6] X. Lu, D.A. Beaton, R.B. Lewis, T. Tiedje, and M.B. Whitwick, "Effect of molecular beam epitaxy growth conditions on the Bi content of $GaAs_{1-x}Bi_x$", *Applied Physics Letters,* vol. **92**, pp. 192110, 2008.

[7] F. Bastiman, A.R.B. Mohmad, J.S. Ng, J.P.R. David, and S.J. Sweeney, "Non-stoichiometric GaAsBi/GaAs (100) molecular beam epitaxy growth", *Journal of Crystal Growth,* vol. **338**, pp. 57-61, 2012.

[8] G. Mussler, J.M. Chauveau, A. Trampert, M. Ramsteiner, L. Däweritz, and K.H. Ploog, "Nitrogen-dependent optimum annealing temperature of Ga(As,N)", *Journal of Crystal Growth,* vol. **267**, pp. 60-66, 2004.

[9] D. Sentosa, X. Tang, Z. Yin, and S.J. Chua, "Thermal annealing effect on GaNAs epilayers with different nitrogen compositions grown by MOCVD", *Journal of Crystal Growth,* vol. **307**, pp. 229-234, 2007.

Chapter 5

Effects of Growth Parameters on GaAsBi Alloys

5.1. Motivation

The results in Chapter 4 show that ex-situ thermal annealing does not provide a significant PL improvement compared to the as-grown samples (~ 3 times improvement). Therefore, understanding the effect of each of the growth parameters is important in improving wafer quality. MBE growth optimization normally involves three main parameters, which are growth temperature, V/III flux ratio and growth rate. The effects of growth temperature and V/III ratio on the incorporation of Bi into GaAs have been discussed earlier in Chapter 1.

However, the effect of growth rate is not widely reported. Recently, Ptak *et al* reported the presence of two growth regimes for the growth of $GaAs_{1-x}Bi_x$ which depend on the growth rate [1]. However, the cause of the different growth regimes is not known. In this chapter, two growth parameters are investigated which are growth rate and As_4/Bi BEP ratio. The $GaAs_{1-x}Bi_x$/GaAs interface abruptness also will be discussed.

5.2. Description of samples

Material	Thickness (nm)	Growth temperature (°C)
GaAs cap	100	370
$GaAs_{1-x}Bi_x$ layer	25	370
GaAs buffer	500	580
S.I (100) GaAs substrate		

Figure 5.1 Sample structure.

Figure 5.1 shows the structure of the $GaAs_{1-x}Bi_x$ samples discussed in Sections 5.3 to 5.5. For Section 5.4, the growth rate was varied between 0.09 to 1 µm/h while the As_4/Ga BEP ratio was fixed at 22. For Section 5.5, the growth rate was fixed at 0.6 µm/h while the As_4/Bi BEP ratio was varied between 130 to 75. The ratio was varied by changing the Bi flux while other growth parameters were fixed.

5.3. RHEED observations

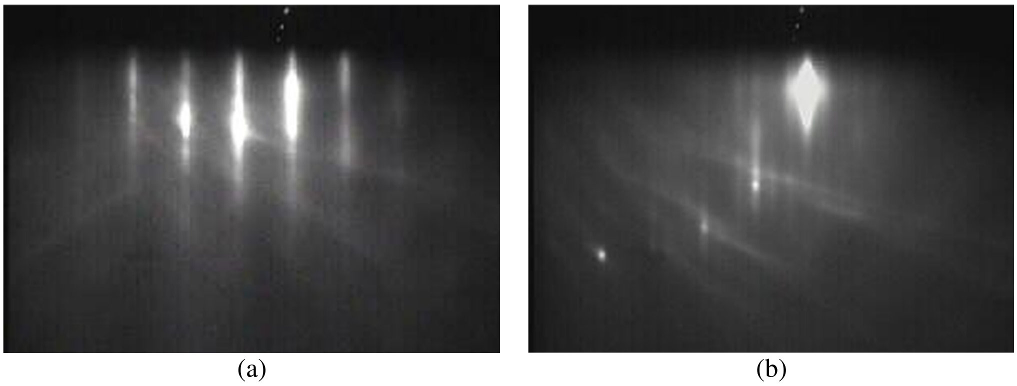

(a) (b)

Figure 5.2 The RHEED diffraction patterns observed from the $[\bar{1}\ 1\ 0]$ azimuth during the growth of (a) the GaAsBi layer and (b) the GaAs capping layer.

Figure 5.2 (a) shows a 1× RHEED diffraction pattern observed from the $[\bar{1}\ 1\ 0]$ azimuth during the growth of a $GaAs_{1-x}Bi_x$ layer. For the [1 1 0] azimuth, a 2× pattern was observed (RHEED not shown), forming a (2 × 1) Bi stabilized surface reconstruction during the $GaAs_{1-x}Bi_x$ growth [2-4]. Ref. [4] observed two major surface reconstructions during $GaAs_{1-x}Bi_x$ growth which are (2 × 1) and (1 × 3). The former is obtained when the As/Ga flux ratio is near stoichiometric while the latter is achieved at high As/Ga flux ratios. It was reported that samples grown on the (2 × 1) reconstructed surface have higher PL intensity and higher Bi content (more than double at a growth temperature of 300 °C) compared to samples grown on (1 × 3) reconstructed surfaces [4].

When growing the GaAs capping layer, the surface reconstruction changes from (2 × 1) to (1 × 3). The typical surface reconstruction for GaAs is (2 × 4). This observation suggests that the GaAs capping layer is grown with a Bi stabilized surface. The unincorporated Bi which accumulates on the surface during $GaAs_{1-x}Bi_x$ growth continues to surface segregate during the GaAs capping layer growth. It is also possible that a dilute amount of Bi impurities is incorporated into the GaAs capping layer.

5.4. Growth rate

5.4.1. Photoluminescence and HR-XRD results

Figure 5.3 (a) shows the room temperature PL peak wavelength as a function of $GaAs_{1-x}Bi_x$ growth rate. For Bi BEP of 5.2×10^{-8} mBar, the PL peak wavelength increases from 980 to 1155 nm as the growth rate is increased from 0.09 to 0.23 µm/h. However, the PL peak wavelength decreases to 1067 nm when the growth rate is further increased to 0.5 µm/h. Therefore, a maximum PL peak wavelength of 1155 nm is achieved at the growth rate of 0.23 µm/h. For Bi BEP of 1.1×10^{-7} mBar, a similar trend was observed. However, the maximum PL wavelength is red-shifted to 1287 nm at the growth rate of 0.5 µm/h. The HR-XRD spectra in the inset of Figure 5.3 (a) show that, for a given Bi BEP, higher Bi concentrations are achieved at higher growth rates. Hence, the change in PL peak wavelength with growth rate can be attributed to the increase of Bi concentration.

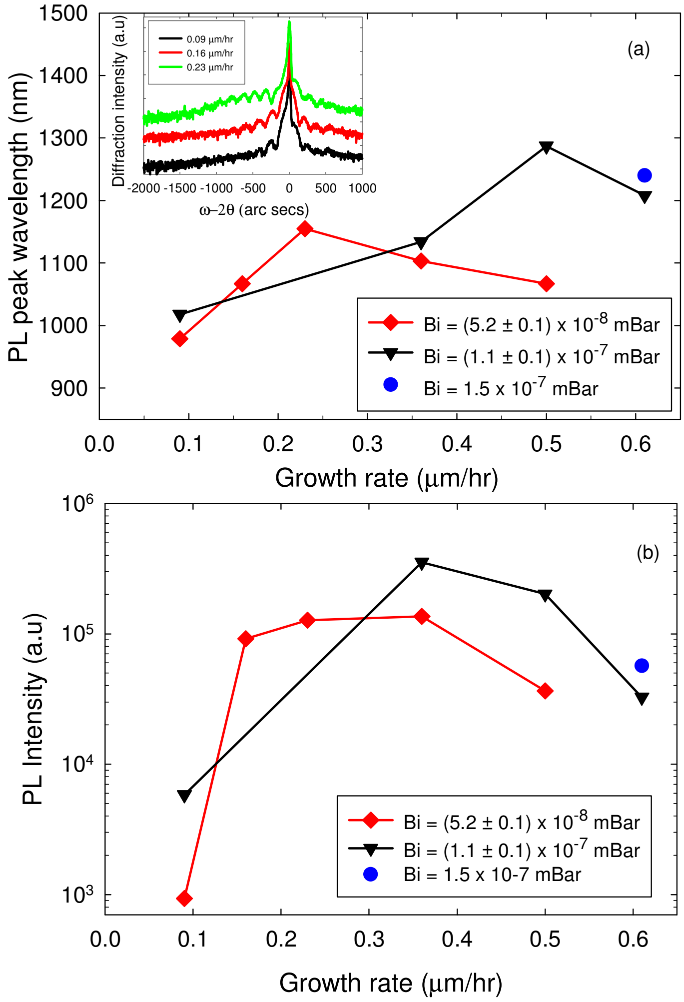

Figure 5.3 The effect of GaAsBi growth rate on (a) PL peak wavelength and (b) room temperature PL intensity. The inset shows the HR-XRD spectra for samples grown with Bi BEP of 5.2×10^{-8} mBar.

It is well-known that Bi has a strong tendency to surface segregate and form a Bi floating layer. Therefore, Bi atoms which reach the growing surface will be either i) incorporated into the lattice ii) segregated to the surface and form the Bi floating layer or iii) get desorbed. The accumulation of Bi on the surface is highly dependent on the growth rate [1]. At high growth rates, higher fractions of Bi adatoms are being incorporated and less are being segregated to the surface. This is because high growth rates effectively bury Bi adatoms into the lattice by reducing the amount of time for the Bi to surface segregate [1]. Hence, Bi concentration increases with growth rate. Conversely, low growth rates provide a sufficient time for Bi adatoms to surface segregate and, consequently, avoidbeing incorporated.

Since high growth rates reduce the segregation of Bi atoms, the creation of a Bi-rich surface and the onset of the formation of Bi droplets will be delayed. All samples shown in Figure 5.3 did not show any presence of Bi droplets. However, this finding contradicts that of Lu *et al*, which proposed that the density of Bi droplets could be reduced by utilizing a low growth rate as it maximizes the chance of excess Bi evaporating [5].

In order to maintain a constant As_4/Ga BEP ratio, the increase of growth rate is also accompanied by an increase of arsenic flux. The supply of a high arsenic flux increases the competition between arsenic and Bi for gallium sites. For Bi BEP of 5.2×10^{-8} mBar, the As_4/Bi BEP ratios are 85 and 212 for the samples grown at 0.23 and 0.5 µm/h, respectively. Therefore, increasing the growth rate beyond the optimum value while maintaining a constant Bi flux will eventually lead to the reduction of Bi concentration as observed in Figure 5.3 (a).

Figure 5.3 (b) shows PL intensity versus growth rate for the samples discussed in Figure 5.3 (a). The PL intensity initially increases with growth rate due to higher Bi composition (discussed earlier in Chapter 3). However, the PL intensity reduces at high growth rates. In order to make a fair comparison, samples with similar PL peak wavelength are compared. For Bi BEP of 5.2×10^{-8} mBar data, the sample grown at 0.16 µm/h has a PL intensity of almost 3 times higher than that of the sample grown at 0.5 µm/h, even though both samples have similar PL peak wavelengths (1067 nm). This is due to the shortage of surface Bi (less surfactant effect) as a result of relatively low Bi flux with respect to the growth rate. The use of high growth rate requires the supply of high Bi flux in order to maintain a sufficient Bi surfactant. The shortage of Bi surfactant will result in a rougher sample surface and degradation of the optical quality. This is similar to the case of surfactant-free GaAs grown at low temperatures [6, 7]. Similarly, growing $GaAs_{1-x}Bi_x$ at slow growth rates requires relatively low Bi flux. This is because the creation of a Bi-rich surface can easily be achieved as higher fractions of Bi atoms are being segregated at slow growth rates. Over-supplying the Bi flux with respect to the growth rate will eventually lead to the formation of Bi droplets.

5.4.2. SIMS and TEM results

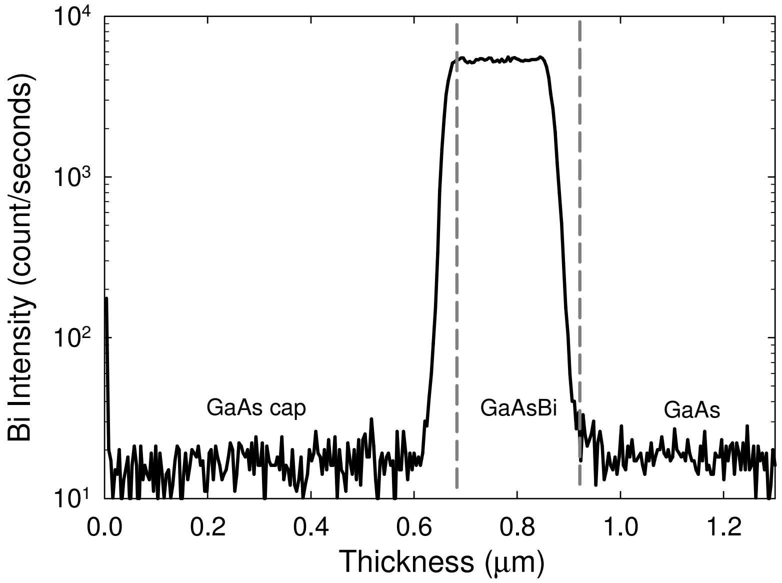

Figure 5.4 The Bi concentration profile obtained by SIMS for a 200 nm thick GaAsBi sample grown at 0.18 μm/h.

In order to investigate the effect of growth rate on the structural properties of $GaAs_{1-x}Bi_x$, Secondary Ion Mass Spectrometry (SIMS) and Transmission Electron Microscopy (TEM) analyses were carried out. All SIMS measurements reported in this work were carried out by Dr. D. E. Sykes from Loughborough Surface Analysis Ltd. This sub-section uses additional samples to the one described in Section 5.2. Figure 5.4 shows the Bi concentration profile obtained by SIMS for a 200 nm thick $GaAs_{1-x}Bi_x$ sample grown at 0.18 μm/h (slow growth rate). The SIMS measurement was carried out using caesium ion bombardment with an impact energy of 14.5 keV.

The SIMS profile shows two important features, i) a plateau Bi concentration across the $GaAs_{1-x}Bi_x$ layer and ii) Bi concentration grading at both of the $GaAs_{1-x}Bi_x$/GaAs interfaces. The plateau Bi profile across the active region is expected.

However, Bi concentration reaches a plateau at thickness ~ 67 nm from the intended bottom interface and reaches a minimum after ~ 54 nm from the intended top interface. The interface non-abruptness can be attributed to the gradual build-up or decay of the Bi floating layer. The transient build-up of the Bi floating layer at the onset of $GaAs_{1-x}Bi_x$ growth results in a reduced number of Bi adatoms available for incorporation. Hence, a region of graded and Bi-deficient $GaAs_{1-x}Bi_x$ layer will be formed at the interface. When the GaAs capping layer is grown, the Bi floating layer will be depopulated and result in another $GaAs_{1-x}Bi_x$ graded layer at the top interface. Similar interface broadening has been observed in InGaAs/GaAs and GaAsSb/GaAs material systems due to the formation of indium and antimony floating layers, respectively [8-10]

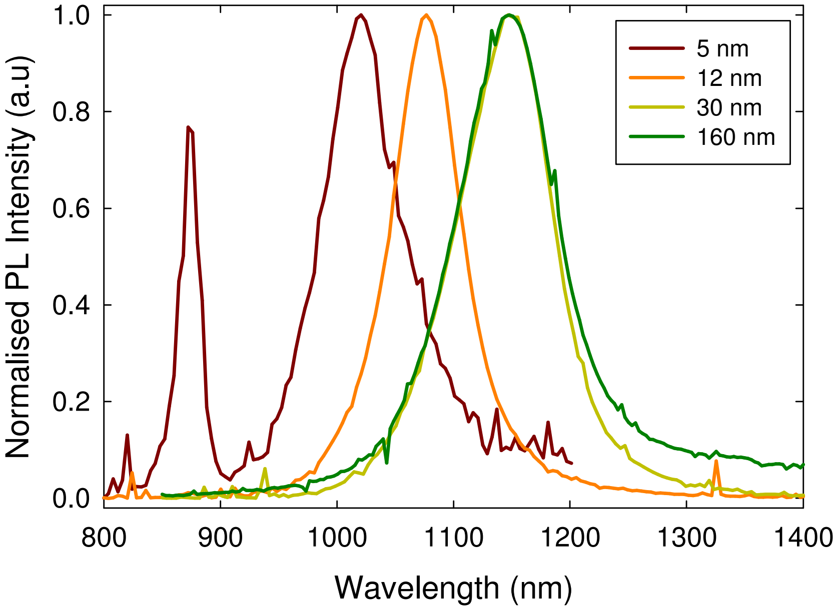

Figure 5.5 PL spectra of GaAsBi samples with various thicknesses grown at a rate of 0.18 µm/h.

The SIMS profile in Figure 5.4 shows that Bi concentration reaches a plateau at thickness ~ 67 nm from the intended interface. However, this value does not represent the real nominal thickness as it also includes the broadening effects induce by SIMS measurements. In order to estimate the nominal layer thickness (thickness required to achieve the nominal Bi concentration), a set of $GaAs_{1-x}Bi_x$ wafers with varying thicknesses were studied. The samples were grown under identical growth conditions at a rate of 0.18 μm/h. The PL data for samples with thicknesses of 5, 12, 30 and 160 nm are shown in Figure 5.5. The PL peak wavelength initially shows a trend of red-shift with increasing thickness. The samples with thicknesses of 5, 12 and 30 nm have PL peak wavelengths of 1017, 1073 and 1143 nm, respectively. However, the PL peak wavelength is similar for the 30 and 160 nm thick samples.

The emission wavelength for the 5 nm thick sample is expected to be blue-shifted with respect to bulk $GaAs_{1-x}Bi_x$ due to quantum well effects. The amount of blue-shift is predicted to be 30 nm for a 5 nm thick $GaAs_{1-x}Bi_x$ ($x = 0.037$) quantum well and becomes negligible for well thickness of more than 10 nm [11]. However, the blue-shift between the 5 and 12 nm thick $GaAs_{1-x}Bi_x$ is 53 nm, which is larger than the predicted blue-shift induced by the quantum effects. This suggests that the Bi concentration varies between the samples. The increase of Bi concentration with thickness (5 to 30 nm) verifies the presence of a $GaAs_{1-x}Bi_x$ grading layer at the interface. For 30 and 160 nm thick samples, the PL wavelength is similar because the $GaAs_{1-x}Bi_x$ layer for both samples is thick enough to reach the nominal Bi concentration or the plateau region. This result suggests that the nominal layer thickness for this growth condition is between 12 and 30 nm from the interface.

For an accurate assessment on the quality of GaAsBi/GaAs interfaces, a TEM image (measured by T. Walther) for a sample grown at 0.18 μm/h is shown in Figure 5.6. The sample has a 20 nm GaAsBi layer and a 50 nm GaAs cap. The cross-section TEM image verifies the presence of a Bi concentration grading at both of the GaAsBi/GaAs interfaces. The Bi concentration reaches its nominal value after ~ 8 nm from the intended bottom interface and reaches a minimum after ~ 9 nm from the intended top interface. The nominal thickness obtained by TEM is much smaller than the range estimated by PL in Figure 5.5 (12 – 30 nm). At the moment it is not clear what causes the difference in the estimated nominal thickness. One possible explanation is over-estimation of the bismide layer thickness (for samples in Figure 5.5) due to growth rate miscalibration. This problem is not an issue for TEM analysis as the layer thickness was determined by analyzing the sample's cross section. In the case of $GaAs_{0.8}Sb_{0.2}$, the nominal layer thickness was reported to be ~ 8 nm [10]. This value is similar to the estimated nominal thickness obtained by TEM.

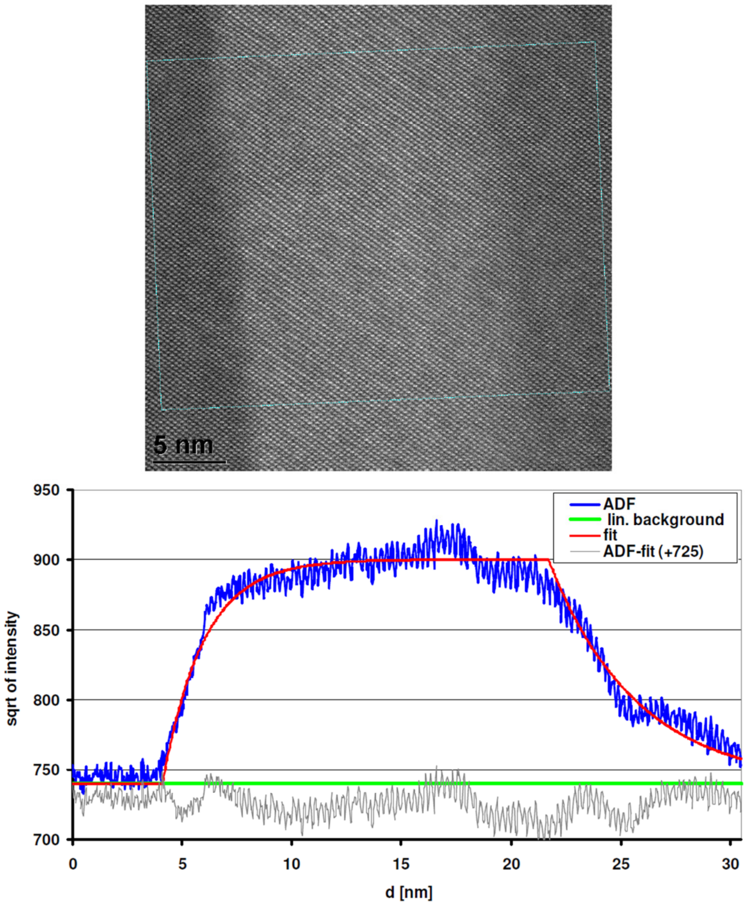

Figure 5.6 The TEM annular dark field (ADF) image for sample *LE2* grown at a rate of 0.18 μm/h. The growth direction is towards the right.

Next, the structural quality of $GaAs_{1-x}Bi_x$ samples grown at high growth rate is investigated. Figure 5.7 shows the TEM images acquired in (002) dark field for samples grown at 1 μm/h with $GaAs_{1-x}Bi_x$ thicknesses of 25 and 80 nm. The TEM images were taken by D. F. Reyes from University of Cadiz, Spain (research collaborator). The $GaAs_{1-x}Bi_x$ layer can be clearly identified as the image brightness varies with Bi concentration. Both samples show similar Bi distributions for the first 20 nm. The area close to the bottom interface shows a higher Bi concentration. However, the Bi content progressively decays beyond 5nm. The decay is unexpected as the growth conditions remain the same. For the 80 nm thick sample, the Bi concentration is almost constant for the last 60 nm at approximately half of the maximum Bi content. These results are in contrast with the distribution of Bi in the samples grown at slow growth rate shown in Figure 5.6.

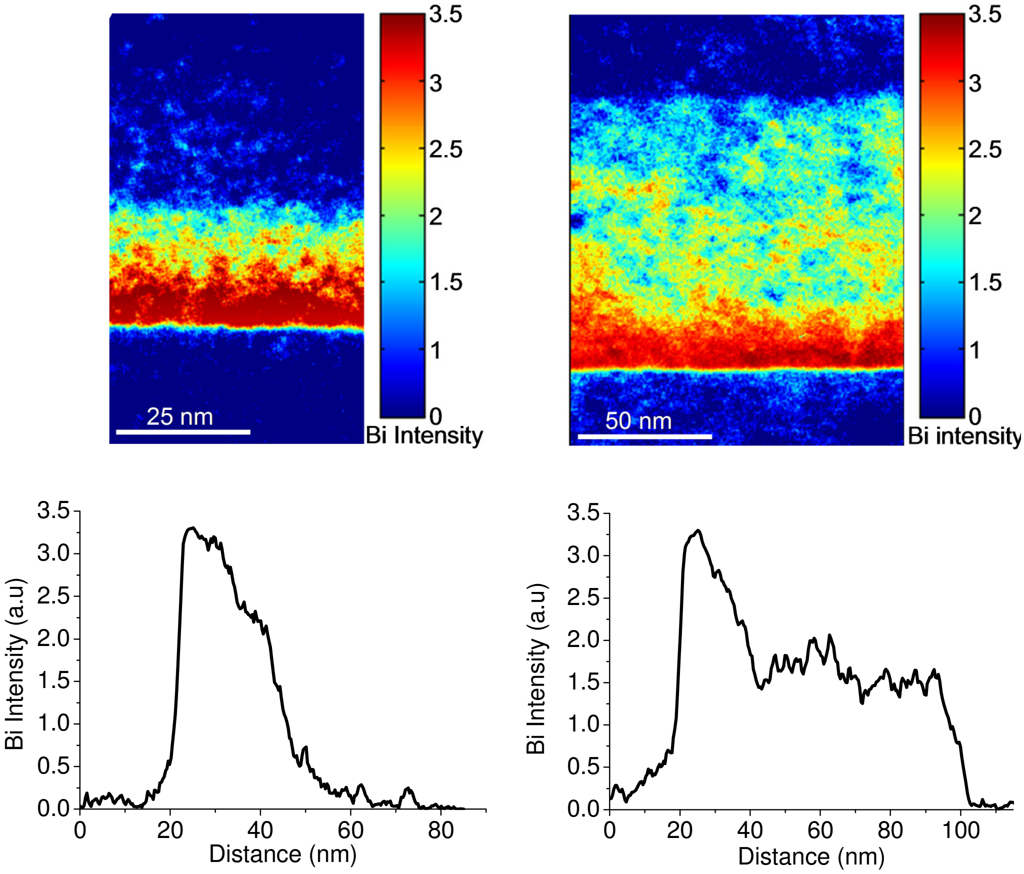

(a) (b)

Figure 5.7 The TEM (002) dark field image colour map (sensitive to composition) of GaAsBi layer with thickness of (a) 25 nm and (b) 80 nm. The samples were grown at 1 μm/h.

The reason which causes the decay of Bi concentration for thickness > 5 nm is unclear. However, one possible explanation is the reduction to the amount of gallium available for Bi bonding. When the $GaAs_{1-x}Bi_x$ growth starts, the layer is initially grown on a surface with a very low coverage of surface Bi. The high growth rate effectively burys Bi adatoms into the lattice while the unincorporated Bi forms a floating layer. The population of the floating layer will eventually change the surface to become Bi-rich. The decay of Bi composition may occur when this surface transition happens. This is because the presence of a high density of Bi floating layer on the surface may reduce the access between Bi and gallium. The reduction of the amount of gallium available for Bi bonding results in the reduction of Bi concentration. Conversely, for $GaAs_{1-x}Bi_x$ grown at slow growth rates, the formation of Bi concentration overshoot is avoided as Bi is being incorporated at much lower rate during the build-up of the floating layer. Hence, the effect of the surface transition is not so pronounced. Figure 5.8 illustrates the effect of the surface transition during $GaAs_{1-x}Bi_x$ growth on Bi concentration for samples grown at high growth rates. The second possible explanation is that the incorporation of a high fraction of Bi in the first few nm increases the overall system strain. This in turn reduces the solubility of the incoming Bi atoms and results in the reduction of Bi concentration.

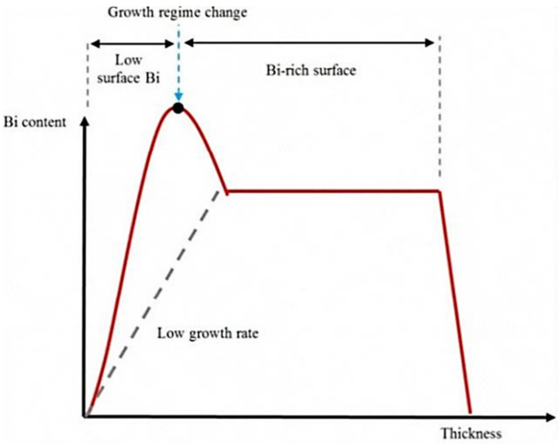

Figure 5.8 Illustration of the effect of the surface transition on Bi incorporation for samples grown at high growth rates.

5.5. As_4/Bi BEP ratio

Sample name	Bi BEP ($\times10^{-7}$ mBar)	As_4 BEP ($\times10^{-5}$ mBar)	As_4/Bi BEP ratio
STC1B	1.1	1.43	130
STC1C	1.5	1.43	95
STC1E	1.9	1.43	75

Table 5.1 Summary of samples with growth parameters.

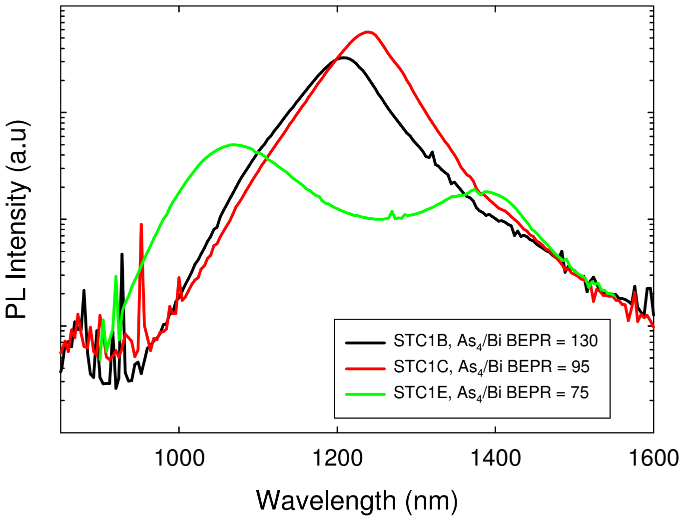

Figure 5.9 PL spectra of GaAsBi samples grown with different As_4/Bi BEP ratios.

Three $GaAs_{1-x}Bi_x$ samples grown with different As_4/Bi BEP ratios are compared. The samples were grown at a rate of 0.6 μm/h and the growth conditions are summarised in Table 5.1. Figure 5.9 shows the room temperature PL data of $GaAs_{1-x}Bi_x$ samples grown with As_4/Bi BEP ratios of 130, 95 and 75. Initially, decreasing the As_4/Bi BEP ratio from 130 to 95 causes the PL peak wavelength to red-shift from 1208 to 1240 nm. The shape of the PL spectra remains relatively unchanged with FWHM of ~ 70 meV. However, the PL spectra changes drastically for the As_4/Bi BEP ratio of 75, showing the presence of two main peaks at 1070 and 1380 nm. The PL intensity also reduces by at least an order of magnitude compared to sample *STC1C*. The origin of the double PL peaks is unclear. However, possibilities include the onset of the formation of Bi droplets or emission from the capping layer due to the large incorporation of Bi impurities. This result suggests that decreasing the As_4/Bi BEP ratio or increasing the Bi flux to enhance Bi incorporation is limited by the formation of double PL peaks.

SIMS analysis was used to evaluate the structural quality of the best sample, *STC1C*. The Bi concentration profile for sample *STC1C* is shown in Figure 5.10. The SIMS measurement was carried out using oxygen ion bombardment with an impact energy of 3 keV. The relatively low impact energy was used in order to reduce SIMS broadening effects.

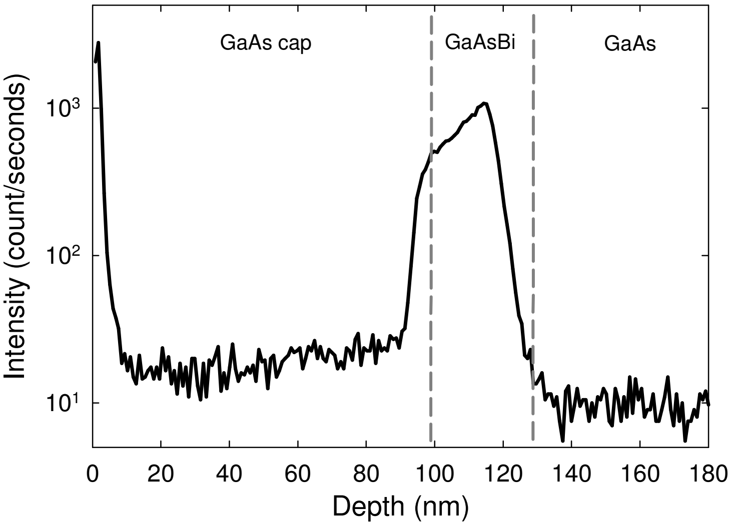

Figure 5.10 Bi concentration profiles obtained by SIMS for sample *STC1C* grown with an As_4/Bi BEP ratio of 95.

The SIMS profile shows that both the $GaAs_{1-x}Bi_x$/GaAs interfaces are not abrupt due to the gradual build-up and decay of the Bi floating layer. The Bi concentration reaches a maximum 13 nm from the intended bottom interface and reaches a minimum 8 nm after the intended top interface. The Bi concentration across the $GaAs_{1-x}Bi_x$ layer also shows a progressive decay after reaching a maximum, similar to that observed in Figure 5.7. For the GaAs capping layer, Bi concentration is low but remains slightly higher than the noise floor. This suggests that a dilute amount of Bi impurities are incorporated into the capping layer. A sharp spike near to the sample's surface is an artefact from SIMS and can be neglected.

5.6. GaAsBi quantum wells

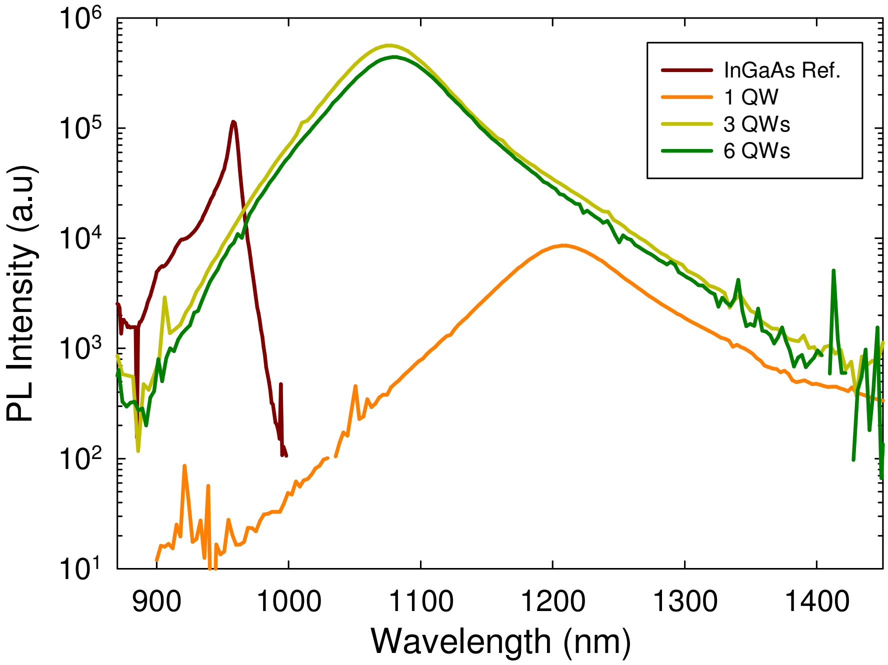

Figure 5.11 PL spectra of GaAsBi QWs grown with different periods. The reference sample is an InGaAs 3-QWs.

In this section, the properties of $GaAs_{1-x}Bi_x$ quantum well (QW) samples are evaluated. The thicknesses of the $GaAs_{1-x}Bi_x$ wells and the GaAs barriers are 7 and 20 nm, respectively. The active region is sandwiched between 500 nm of GaAs buffer and 120 nm of GaAs capping layer. The $GaAs_{1-x}Bi_x$ layer was grown at 370 ^{o}C at a rate of 0.6 µm/h.

Figure 5.11 shows the room temperature PL data of $GaAs_{1-x}Bi_x$ QWs with periods of one, three and six. Interestingly, the PL intensity of the $GaAs_{1-x}Bi_x$ multiple QWs is ~ 4.5 times higher compared to the PL intensity of an $In_{0.15}Ga_{0.85}As$ reference sample (grown at 540 ^{o}C using a standard V90 MBE). The reference sample is a 3-period QW with a well thickness of 10 nm. The three and six-period QW samples have a similar PL wavelength of 1075 nm while the single QW sample has a significantly longer wavelength of 1205 nm. For typical III-V alloys (i.e InGaAs), varying the QW periods should not affect the emission wavelength.

Since the quantum well samples were grown at relatively high growth rate, a pronounced effect due to surface transition is expected. The PL data in Figure 5.11 suggest that the Bi concentration in the first QW is significantly higher compared to other QWs. A weak shoulder observed at long wavelength for the multiple QW samples may be attributed to emission from the first QW while the peak at 1075 nm originates from the $(n + 1)$ QWs (where n is an integer). The significantly lower Bi concentration in $(n + 1)$ QWs suggests that they were grown on Bi-rich surfaces while the first QW with high Bi content was grown on a lowly populated surface Bi. This result is consistent with the Bi concentration decay observed by TEM and SIMS in Figure 5.6 and Figure 5.9, respectively. It also suggests that the population of the Bi floating layer is not significantly affected after the GaAs barrier growths.

5.7. Summary

Two growth parameters were investigated which are growth rate and As_4/Bi BEP ratio. It was found that growth rate significantly affects Bi incorporation and the accumulation of surface Bi. High growth rates efficiently bury Bi adatoms and consequently incorporate a higher fraction of Bi in GaAs. Hence, the accumulation of surface Bi is reduced compared to low growth rates. High growth rates also require relatively high Bi fluxes in order to avoid the shortage of Bi surfactant which will lead to the degradation of the optical quality.

The presence of Bi concentration overshoots near to the GaAs/$GaAs_{1-x}Bi_x$ interface was observed by TEM and SIMS for samples grown at relatively high growth rates (> 0.6 µm/h). Bi concentration started to decay after 5 nm of $GaAs_{1-x}Bi_x$ growth, probably due to the reduction to the amount of gallium available for Bi bonding when the surface becomes Bi-rich. However, this effect was not observed for samples grown at low growth rates due to the slow incorporation of Bi during the population of the floating layer.

In addition, decreasing the As_4/Bi BEP ratio has been shown to increase Bi concentration. However, this is limited by the formation of double PL peaks which is also accompanied by PL intensity degradation.

5.8. References

[1] A.J. Ptak, R. France, D.A. Beaton, K. Alberi, J. Simon, A. Mascarenhas, and C.S. Jiang, "Kinetically limited growth of GaAsBi by molecular-beam epitaxy", *Journal of Crystal Growth,* vol. **338**, pp. 107-110, 2012.

[2] P. Laukkanen, M.P.J. Punkkinen, H.P. Komsa, M. Ahola-Tuomi, K. Kokko, M. Kuzmin, J. Adell, J. Sadowski, R.E. Perälä, M. Ropo, T.T. Rantala, I.J. Väyrynen, M. Pessa, L. Vitos, J. Kollár, S. Mirbt, and B. Johansson, "Anomalous Bismuth-Stabilized (2×1) Reconstructions on GaAs(100) and InP(100) Surfaces", *Physical Review Letters,* vol. **100**, pp. 086101, 2008.

[3] F. Bastiman, A.G. Cullis, J.P.R. David, and S.J. Sweeney, "Bi incorporation in GaAs(100)-2×1 and 4×3 reconstructions investigated by RHEED and STM", *Journal of Crystal Growth,* vol. **341**, pp. 19-23, 2012.

[4] M. Masnadi-Shirazi, D.A. Beaton, R.B. Lewis, X. Lu, and T. Tiedje, "Surface reconstructions during growth of $GaAs_{1-x}Bi_x$ alloys by molecular beam epitaxy", *Journal of Crystal Growth,* vol. **338**, pp. 80-84, 2012.

[5] X. Lu, D.A. Beaton, R.B. Lewis, T. Tiedje, and M.B. Whitwick, "Effect of molecular beam epitaxy growth conditions on the Bi content of $GaAs_{1-x}Bi_x$", *Applied Physics Letters,* vol. **92**, pp. 192110, 2008.

[6] S. Tixier, M. Adamcyk, E.C. Young, J.H. Schmid, and T. Tiedje, "Surfactant enhanced growth of GaNAs and InGaNAs using bismuth", *Journal of Crystal Growth,* vol. **251**, pp. 449-454, 2003.

[7] E.C. Young, S. Tixier, and T. Tiedje, "Bismuth surfactant growth of the dilute nitride GaN_xAs_{1-x}", *Journal of Crystal Growth,* vol. **279**, pp. 316-320, 2005.

[8] J. Nagle, J.P. Landesman, M. Larive, C. Mottet, and P. Bois, "Indium surface segregation in strained GaInAs quantum wells grown on GaAs by MBE", *Journal of Crystal Growth,* vol. **127**, pp. 550-554, 1993.

[9] O.J. Pitts, S.P. Watkins, C.X. Wang, V. Fink, and K.L. Kavanagh, "Antimony segregation in GaAs-based multiple quantum well structures", *Journal of Crystal Growth,* vol. **254**, pp. 28-34, 2003.

[10] R. Kaspi and K.R. Evans, "Sb-surface segregation and the control of compositional abruptness at the GaAsSbGaAs interface", *Journal of Crystal Growth,* vol. **175–176, Part 2**, pp. 838-843, 1997.

[11] S. Jin and S.J. Sweeney, "GaAsBi/GaAs Quantum Wells Modelling", *Unpublished manuscript,* vol.,2010.

Chapter 6

Conclusion

6.1 Conclusion

A detailed and systematic study of the optical and structural properties of $GaAs_{1-x}Bi_x$ alloys on GaAs has been carried out. The temperature dependent PL shows that excitons are localized at low temperatures. The band gap was found to vary more weakly with temperature than in GaAs. Furthermore, the band gap of $GaAs_{1-x}Bi_x$ can be described by a modified VBAC model which considers the increase of valence band maxima as well as the reduction of conduction band minima with Bi concentration.

The optical quality of $GaAs_{1-x}Bi_x$ is highly dependent on the Bi concentration. The incorporation of Bi in GaAs reduces the density of gallium and/or arsenic-related defects as well as introducing Bi-related defects. For dilute amounts of Bi ($x < 0.025$), the crystal quality improves due to Bi surfactant effects. However, a further increase of Bi causes degradation to the material quality due to a significant amount of Bi-related defects.

In order to improve the optical quality of $GaAs_{1-x}Bi_x$, a rapid thermal annealing study has been carried out. At room temperature, the annealed $GaAs_{1-x}Bi_x$ showed a modest improvement (~ 3 times) in PL while the PL peak wavelength remained relatively unchanged. It was found that the PL improvement may be dominated by the reduction of non-Bi related defects. The optimum annealing temperature is also Bi composition dependent. For samples with $x < 0.048$, the optimum annealing temperature is 700 ^{o}C but it reduces to 600 ^{o}C for higher compositions.

The effects of growth parameters to the properties of $GaAs_{1-x}Bi_x$ have been evaluated. It was found that growth rate significantly affects Bi incorporation and the accumulation of surface Bi. Higher Bi concentrations and lower populations of surface Bi can be achieved at high growth rates due to the efficient burying of Bi adatoms into the lattice. However, for samples grown at relatively high growth rates (> 0.6 µm/h), Bi concentration overshoot near to the $GaAs/GaAs_{1-x}Bi_x$ interface was observed. This effect was not observed for samples grown at low growth rates due to slow incorporation of Bi during the population of the Bi floating layer. Decreasing the As_4/Bi BEP ratio has been shown to increase Bi concentration but is limited by the formation of Bi double PL peaks.

6.2 Suggestions for future work

1. The growth of a superlattice requires an abrupt interface between the layers. However, this work found that $GaAs_{1-x}Bi_x/GaAs$ interfaces are not abrupt due to Bi compositional grading. Therefore, a study to improve the $GaAs_{1-x}Bi_x/GaAs$ interface abruptness is suggested. Kaspi *et al* proposed that the interface abruptness between GaAs/GaAsSb can be improved by soaking the GaAs surface with antimony prior to GaAsSb growth [1]. The antimony population also must be optimized so that it is equivalent to the amount expected on the GaAsSb surface during growth at steady state [1]. For a GaAsSb/GaAs interface, compositional abruptness can be enhanced by ‘flashing off’ the antimony floating layer with arsenic flux before the GaAs growth [1]. However, Wu *et al* found that soaking the GaAs surface with antimony prior to GaAsSbN growth lead to lower PL intensity and larger FWHM compared to simultaneous shutter opening [2].

2. The high temperature performance of $GaAs_{1-x}Bi_x$ QW based devices might be poor due to lack of electron confinement. This is because Bi composition mainly affects the valence band offset. Therefore, the use of AlGaAs cladding layers is important to improve the electron confinement. However, the top

AlGaAs cladding might have to be grown at ~ 300 to 400 °C, similar to the growth temperature of the $GaAs_{1-x}Bi_x$ layer. The growth of AlGaAs at low temperatures (optimum growth temperature ~ 600 °C) might increase defect densities and carrier trapping at the cladding layer. The effect of a Bi surfactant on low temperature growth of AlGaAs is also unknown. Once high quality $GaAs_{1-x}Bi_x$ QWs with AlGaAs cladding can be achieved, a full laser structure can be grown. To date, only an optically pumped $GaAs_{1-x}Bi_x$ laser has been reported in the literature [3].

3. Recently, Norman *et al* have carried out a TEM study and observed the presence of $CuPt_B$-(111) ordering in $GaAs_{1-x}Bi_x$ for x up to 0.1 [4]. The atomic ordering was attributed to the (2 × 1) surface reconstruction during $GaAs_{1-x}Bi_x$ growth. Atomic ordering also has been observed in other mixed anion III-V semiconductors such as InAsSb and GaAsSb [5, 6]. The presence of atomic ordering may affect the optical properties of semiconductor alloys such as PL FWHM broadening and band gap blue-shift [7]. Therefore, a systematic study to investigate the effect of atomic ordering on the optical and electrical properties of $GaAs_{1-x}Bi_x$ would be useful.

6.3 References

[1] R. Kaspi and K.R. Evans, "Sb-surface segregation and the control of compositional abruptness at the GaAsSbGaAs interface", *Journal of Crystal Growth,* vol. **175–176, Part 2**, pp. 838-843, 1997.

[2] L. Wu, S. Iyer, K. Nunna, J. Li, S. Bharatan, W. Collis, and K. Matney, "MBE growth and properties of GaAsSbN/GaAs single quantum wells", *Journal of Crystal Growth,* vol. **279**, pp. 293-302, 2005.

[3] Y. Tominaga, K. Oe, and M. Yoshimoto, "Low Temperature Dependence of Oscillation Wavelength in GaAsBi Laser by Photo-Pumping", *Applied Physics Express,* vol. **3**, pp. 062201, 2010.

[4] A.G. Norman, R. France, and A.J. Ptak, "Atomic ordering and phase separation in MBE $GaAs_{(1-x)}Bi_x$", *Journal of Vacuum Science and Technology B,* vol. **29**, pp. 03C121-5, 2011.

[5] T.-Y. Seong, G.R. Booker, A.G. Norman, and I.T. Ferguson, "Atomic ordering in molecular beam epitaxial $InAs_{(y)}Sb_{(1-y)}$ natural strained layer superlattices and homogeneous layers", *Applied Physics Letters,* vol. **64**, pp. 3593-3595, 1994.

[6] B.P. Gorman, A.G. Norman, R. Lukic-Zrnic, C.L. Littler, H.R. Moutinho, T.D. Golding, and A.G. Birdwell, "Atomic ordering-induced band gap reductions in GaAsSb epilayers grown by molecular beam epitaxy", *Journal of Applied Physics,* vol. **97**, pp. 063701-7, 2005.

[7] T. Suzuki, *Sponteneous Ordering in Semiconductor Alloys*, editted by. A. Mascarenhas. 2002, New York Kluwer, Dordrecht/Plenum.

Appendix A: The Valence Band Anti-Crossing Model

The valence band of $GaAs_{1-x}Bi_x$ is described by,

$$E_{\pm}(\mathrm{GaAsBi}) = \frac{E_v(GaAs) + E_{Bi} \pm \sqrt{(E_v(GaAs) - E_{Bi})^2 + 4xC_{Bi}^2}}{2} \qquad (\mathrm{A.1})$$

Assuming that the conduction band is constant, the band gap of $GaAs_{1-x}Bi_x$ is

$$E_g(GaAsBi) = E_c(GaAs) - E_+(GaAsBi)\,, \qquad (\mathrm{A.2})$$

where E_c is the conduction band minimum of GaAs. Since,

$$E_{Bi} = E_v(GaAs) - \Delta E_{VBM-Bi} \qquad (\mathrm{A.3})$$

and

$$E_g(GaAs) = E_c(GaAs) - E_v(GaAs)\,, \qquad (\mathrm{A.4})$$

where $\Delta E_{VBM\text{-}Bi}$ is the energy difference between the VBM of GaAs and the Bi level. Using Equation (A.1) to (A.4), the band gap of $GaAs_{1-x}Bi_x$ can be simplified to

$$\begin{aligned}
E_g(GaAsBi) &= E_c(GaAs) - \frac{E_v(GaAs) + E_{Bi} + \sqrt{(E_v(GaAs) - E_{Bi})^2 + 4xC_{Bi}^2}}{2} \\
&= E_c(GaAs) - \frac{2E_v(GaAs) - \Delta E_{VBM-Bi} + \sqrt{(\Delta E_{VBM-Bi})^2 + 4xC_{Bi}^2}}{2} \\
&= E_g(GaAs) - \frac{1}{2}(\sqrt{(\Delta E_{VBM-Bi})^2 + 4xC_{Bi}^2} - \Delta E_{VBM-Bi}) \\
&= E_g(GaAs) - \frac{\Delta E_{VBM-Bi}}{2}(\sqrt{\frac{(\Delta E_{VBM-Bi})^2 + 4xC_{Bi}^2}{(\Delta E_{VBM-Bi})^2}} - 1) \\
&= E_g(GaAs) - \frac{\Delta E_{VBM-Bi}}{2}(\sqrt{1 + \frac{4xC_{Bi}^2}{(\Delta E_{VBM-Bi})^2}} - 1)
\end{aligned}$$

$$E_g(GaAsBi) = E_g(GaAs) - \Delta E_{VBAC}, \tag{A.5}$$

Here, ΔE_{VBAC} refers to the band gap reduction due to bismuth incorporation, which is given by,

$$\Delta E_{VBAC} = \frac{\Delta E_{VBM-Bi}}{2}\left(\sqrt{1 + \frac{4xC_{Bi}^2}{(\Delta E_{VBM-Bi})^2}} - 1\right) \tag{A.6}$$

Appendix B: Sample details

NR = Not recorded

Sample name	Section(s)	Bi content (*estimated by PL)	GaAsBi growth						GaAsBi structure
			Growth temp. (^{o}C)	Growth rate (µm/h)	As$_4$ sublimator temp. (^{o}C), BEP (x10^{-6} mBar)	As cracker	Ga cell temp. (^{o}C), BEP (×10^{-7} mBar)	Bi cell temp. (^{o}C), BEP (×10^{-7} mBar)	
GC	3.2.2	0.014	400	0.16	320, NR	✖	880, NR	500, NR	50 nm
G4	3.2.2	0.021	400	0.16	320, NR	✖	880, NR	525, NR	160 nm
BA	3.2	0.03	400	0.16	320, NR	✖	885, NR	520, NR	160 nm
X	3.3	0.005	420	0.16	318, NR	✖	930, NR	510, NR	100 nm
Y	3.3	0.009	420	0.16	318, NR	✖	930, NR	520, NR	100 nm
Z	3.3	0.025	420	0.16	318, NR	✖	930, NR	530, NR	100 nm
GB	3.3	0.027	400	0.16	320, NR	✖	880, NR	520, NR	50 nm
GP	3.3	0.036	400	0.16	320, NR	✖	880, NR	545, NR	50 nm
GR	3.3	0.045	400	0.16	320, NR	✖	880, NR	550, NR	50 nm
LR	3.3, 4.3	0.022	400	0.16	322, NR	✖	880, NR	500, NR	25 nm
LS	3.3, 4.3	0.033	400	0.16	322, NR	✖	880, NR	510, NR	25 nm
LV	3.3, 4.3	0.048	400	0.16	322, NR	✖	880, NR	520, NR	25 nm

Sample name	Section(s)	Bi content (*estimated by PL)	GaAsBi growth						GaAsBi structure
			Growth temp. (°C)	Growth rate (µm/h)	As$_4$ sublimator temp. (°C), BEP (x10^{-6} mBar)	As cracker	Ga cell temp. (°C), BEP (×10^{-7} mBar)	Bi cell temp. (°C), BEP (×10^{-7} mBar)	
LT	3.3, 4.3	0.06	400	0.16	322, NR	✗	880, NR	530, NR	25 nm
STB0DT	4.3	0.04	420	1.0	380, 17	✓	1022, 8.2	550, 1.3	10 nm
STB02G	4.3	0.065	380	0.18	315, 4.5	✗	924, 2.4	530, NR	50 nm
STB0GW	4.4, 5.4.1	0.042	370	0.36	380, 6.8	✓	980, 3.0	520, NR	25 nm
STC01B	4.4	0.058	400	0.6	380, 14	✓	1030, NR	543, 1.1	25 nm
STB02C	4.5	0.037	400	0.18	324, NR	✗	896, NR	550, NR	44 nm
STB02H	4.5	0.05	400	0.18	315, NR	✗	924, NR	530, NR	50 nm
STB0GU	5.4.1	0.02*	370	0.09	380, 1.6	✓	900, 0.72	520, 0.53	25 nm
STB0GV	5.4.1	0.036*	370	0.16	380, 2.9	✓	935, 1.4	520, 0.52	25 nm
STB0GS	5.4.1	0.051*	370	0.23	380, 4.6	✓	950, 2.0	520, 0.53	25 nm
STB0GT	5.4.1	0.036*	370	0.50	380, 11.5	✓	997, 5.0	520, 0.52	25 nm
STC13	5.4.1	0.027*	370	0.09	380, 1.8	✓	902, 0.74	540, 1.1	25 nm
STC19	5.4.1	0.048*	370	0.36	380, 7.8	✓	989, 3.4	543, 1.1	25 nm
STC15	5.4.1	0.071*	370	0.50	380, 11.5	✓	1004, 5.0	540, 1.0	25 nm
STC1B	5.4.1, 5.5	0.059*	370	0.61	380, 14.3	✓	1030, 6.2	543, 1.1	25 nm
STC1C	5.4.1, 5.5	0.064*	370	0.61	380, 14.3	✓	1031, 6.2	550, 1.5	25 nm

Sample name	Section(s)	Bi content (*estimated by PL)	GaAsBi growth						GaAsBi structure
			Growth temp. (^{o}C)	Growth rate (µm/h)	As$_4$ sublimator temp. (^{o}C), BEP (x10^{-6} mBar)	As cracker	Ga cell temp. (^{o}C), BEP (×10^{-7} mBar)	Bi cell temp. (^{o}C), BEP (×10^{-7} mBar)	
STB064	5.4.2	0.051	370	0.18	324, 6.6	✗	923, 2.2	530, 0.5	200 nm
H6	5.4.2	0.027*	400	0.18	320, NR	✗	885, NR	550, NR	5 nm
H8	5.4.2	0.037*	400	0.18	320, NR	✗	885, NR	550, NR	12 nm
H9	5.4.2	0.049*	400	0.18	320, NR	✗	885, NR	550, NR	30 nm
H5	5.4.2	0.049*	400	0.18	320, NR	✗	885, NR	550, NR	160 nm
LE2	5.4.2	0.056	400	0.18	322, NR	✗	880, NR	540, NR	20 nm
STB0DP	5.4.2	0.035	370	1.0	380, 17	✓	1022, 8.3	550, 1.4	25 nm
STB0DI	5.4.2	0.033	370	1.0	380, 17	✓	1022, 8.5	550, 1.4	80 nm
STC1E	5.5	0.036*, 0.083*	370	0.6	380, 14.3	✓	1031, 6.2	562, 1.9	25 nm
New flux monitor installed									
STC2B	5.6	0.059*	370	0.6	395, 14.7	✓	1010, 1.1	540, 2.7	7 nm SQW
STC29	5.6	0.037*	370	0.6	395, 14.7	✓	1010, 1.1	540, 2.6	7 nm 3QW
STC2F	5.6	0.038*	370	0.6	395, 14.7	✓	1010, 1.1	540, 2.8	7 nm 6QW